Dissertation

INTRACELLULAR CALCIUM SIGNALING IN THE REGULATION OF TRANSCRIPTION FACTORS, MITOCHONDRIAL CALCIUM HOMEOSTASIS, BIOENERGETICS, AND APOPTOSIS

submitted by

Furkan Enes Oflaz

for the Academic Degree of

Doctor of Philosophy
(PhD)

at the
Medical University of Graz

Gottfried Schatz Research Center for Cell Signaling, Metabolism & Aging
Molecular Biology & Biochemistry

under the Supervision of
Univ.-Prof. Mag.pharm. Dr.rer.nat. Wolfgang Graier

2023

Statutory Declaration

I hereby declare that this thesis is my own original work and that I have fully acknowledged by name all of those individuals and organizations that have contributed to the research for this thesis. Due acknowledgment has been made in the text to all other material used. Throughout this thesis and in all related publications I followed the “Guidelines of the Medical University of Graz on Good Scientific Practice”.

Graz, October 11th, 2023

Furkan Enes Oflaz

Disclosures

Part of this thesis has been published in:

Oflaz F.E, Koshenov Z, Hirtl M, Rost R, Bachkönig O, Gottschalk B, Madreiter-Sokolowski C, Malli R, Graier WF. Near-UV Light Induced ROS Production Initiates Spatial Ca^{2+} Oscillation to Fire NFATc3 Translocation. Int. J. Mol. Sci. 2021; DOI: 10.3390/ijms22158189

Oflaz F.E, Koshenov Z, Hirtl M, Rost R, Malli R, Graier WF. Sigma-1 Receptor Modulation by Ligands Coordinates Cancer Cell Energy Metabolism. Biomolecules. 2022; DOI: 10.3390/biom12060762

Oflaz F.E, Koshenov Z, Hirtl M, Bachkönig O, Graier WF Gottschalk B,. Synergy of Uncoupling Proteins (1 and 2) with Mitochondrial Ca^{2+} Uptake Machinery Potentiate Mitochondrial Uncoupling. Cell Calcium. 2023-a; DOI: 10.1016/j.ceca.2023.102736

Part of this thesis is under review:

Oflaz F.E, Bondarenko A, Trenker M, Waldeck-Weiermair M, Gottschalk B, Bernhart E, Koshenov Z, Radulović S, Rost R, Hirtl M, Pilif J, Leitinger G, Brachvogel B, Summerauer S, Shoshan-Barmatz V, Malli R, Graier WF. Annexin-A5 is fundamental for VDAC1-dependent mitochondrial Ca2+ homeostasis and determines the susceptibility to apoptosis. Research Square 2023-b; https://doi.org/10.21203/rs.3.rs-3338004/v1

During my PhD studies, I also contributed to the following publications:

Pilic J, Oflaz F.E, Gottschalk B, Graier WF, Malli R. Visualizing interactions of VDAC1 in live cells using a tetracysteine tag. BioRxiv. 2023; doi.org/10.1101/2023.09.08.556841

Pilic J, Gottschalk B, Bourgeois B, Koshenov Z, Oflaz F.E, Erdogan C, Shoshan-Barmatz C, Madl T, Graier WF, Malli R. Hexokinase 1 forms rings that constrict mitochondria during energy stress. BioRxiv. 2023; DOI: 10.1101/2023.03.20.533440

Gottschalk B, Koshenov Z, Waldeck-Weiermair M, Radulović S, Oflaz F.E, Hirtl M, Bachkönig O, Leitinger G, Malli R, Graier WF. MICU1 controls spatial membrane potential gradients and guides Ca^{2+} fluxes within mitochondrial substructures. Commun. Biol. 2022; DOI: 10.1038/s42003-022-03606-3

Koshenov Z, Oflaz F.E, Hirtl M, Gottschalk B, Rost R, Malli R, Graier WF. Citrin mediated metabolic rewiring in response to altered basal subcellular Ca2+ homeostasis. Commun. Biol. 2022; DOI: 10.1038/s42003-022-03019-2

Koshenov Z, Oflaz F.E., Hirtl M, Pilic J, Bachkönig O, Gottschalk B, Madreiter-Sokolowski C, Rost R, Malli R, Graier WF. Sigma-1 Receptor Promotes Mitochondrial Bioenergetics by Orchestrating ER Ca^{2+} Leak during Early ER Stress. Metabolites. 2021; DOI: 10.3390/metabo11070422

Koshenov Z, Oflaz F.E, Hirtl M, Bachkönig O, Rost R, Osibow K, Gottschalk B, Madreiter-Sokolowski C, Waldeck-Weiermair M, Malli R, Graier WF. The contribution of uncoupling protein 2 to mitochondrial Ca^{2+} homeostasis in health and disease -A short revisit. Mitochondrion. 2020; DOI: 10.1016/j.mito.2020.10.003

The following co-authors contributed to my first-authors publications:

Zhanat Koshenov, Alexander I. Bondarenko, Johannes Pilic, Martin Hirtl, Olaf A. Bachkoenig, Benjamin Gottschalk, Rene Rost, Corina T. Madreiter-Sokolowski, Eva Bernhart, Michael Trenker, Markus Waldeck-Weiermair, Roland Malli, Wolfgang F. Graier: Gottfried Schatz Research Center, Division of Molecular Biology and Biochemistry, Medical University of Graz, Neue Stiftingtalstraße 6/6, 8010 Graz, Austria

Zhanat Koshenov: Present address: Department of Biochemistry, Weill Cornell Medicine, New York, USA

Snježana Radulović, Gerd Leitinger, Susanne Summerauer: Gottfried Schatz Research Center: Cell Biology, Histology and Embryology, Medical University of Graz, Graz, Austria

MichaelTrenker: Present address: MM Frohnleiten GmbH, Frohnleiten, Austria

Markus Waldeck-Weiermair: Present address: Division of Cardiovascular Medicine, Department of Medicine, Brigham and Women's Hospital, Harvard Medical School, 75 Francis Street, Boston, MA, 02115, USA.

Bent Brachvogel: Department of Pediatrics and Adolescent Medicine, Experimental Neonatology, Faculty of Medicine and University Hospital Cologne, University of Cologne, Cologne, Germany.

Varda Shoshan-Barmatz: Department of Life Sciences, and the National Institute for Biotechnology in the Negev, Ben-Gurion University of the Negev, 84105, Beer Sheva, Israel.

I confirm that all co-authors have agreed to use their data in my thesis (signed confirmations are available). I have permission from the publisher to reproduce figures published in Oflaz et al. 2021, Oflaz & Koshenov et al. 2022, Oflaz et al. 2023-a and Oflaz et al. 2023-b. All four papers are distributed under the terms of the Creative Commons CC BY license, which permits unrestricted use, distribution, and reproduction in any medium, provided the original work is properly cited.

Acknowledgments

As a PhD student, I received funding from the Austrian Science Fund (FWF) through the Doctoral College Metabolic and Cardiovascular Disease (DK-MCD W1226-B18), under the supervision of Wolfgang F. Graier.

I want to express my deep gratitude to my supervisor, Wolfgang Graier, for his constant support, motivation, and belief in me. From the very beginning of my Ph.D journey until its completion, he has played a pivotal role in enhancing my scientific perspective. His enthusiasm for science has consistently impressed me and greatly motivated me to develop my research and engage in continuous discussions with him. I admire his approach to questions, always thinking outside of the box. I am confident that the completion of my Ph.D journey marks the commencement of a new phase in scientific exploration and I hope to continue collaborating and working with him in the future.

I would like to extend my special thanks to my thesis committee members, Roland Malli and Rainer Schindl. Their invaluable comments and insightful suggestions have greatly contributed to the my research projects.

I would like to convey my gratitude to Varda-Shoshan Barmatz for her warm and gracious hospitality during my six-month research stay at Ben Gurion University of the Negev.

My sincere thanks go to my colleagues at the Medical University of Graz, particularly from the Graier & Malli group. It has been a pleasure to share this academic journey with all of you. I thank Rene for being a great companion and for always being willing to lend a helping hand. I want to thank Benjamin for his accessibility during discussions and for providing valuable insights. I want to express my special thanks to Zhanat for being a great friend and for our engaging discussions in the lab, in Manhattan, and even at the Cliffs of Moher. Moreover, I would like to thank Eva, Alexander, Snježana, and Gerd for their great contributions to my research.

I wish to extend my heartfelt appreciation to my wife for her support and encouragement. I truly appreciate her enduring patience during this journey, especially on the days when the experiments lasted almost until midnight. I want to convey my gratitude for her inspiration and help, which has been the driving force behind my journey from day one until the completion of my PhD. This success is as much her as it is mine.

Finally, I am deeply grateful to my family for their unwavering support and love.

Table of Contents

List of Abbreviations 10
Abstract 12
Zusammenfassung 14
1 Introduction 16
1.1 Intracellular Ca^{2+} homeostasis 16
1.2 Impact of intracellular Ca^{2+} cycling on transcription factors 17
1.3 Mitochondrial Ca^{2+} signaling 19
1.4 Role of UCPs on mitochondrial Ca^{2+} uptake and uncoupling 22
1.4 Deciphering the role of Ca^{2+} in mitochondrial bioenergetics 25
1.5 Contribution of Sigma-1 Receptor on mitochondrial bioenergetics in cancer cells 26
1.6 Role of VDAC1 in mitochondrial-mediated apoptosis 27
1.7 Annexin-A5: structure, membrane binding, and contribution to Ca^{2+} homeostasis 29
1.8 Association of Annexin-A5 with Mitochondria 31
1.9 A general overview 32
2 Material Methods 35
2.1 Cell Culture and Transfection 35
2.2 Generation of AnxA5-KO cells 36
2.3 AnxA5 silencing was achieved through Short Hairpin RNA (shRNA) technology 36
2.3 Quantitative PCR 37
2.4 Buffers and Solutions 37
2.5 Live-Cell Imaging Experiments 37
2.6 Detection of Sub-Mitochondrial Ca^{2+} levels 38
2.7 Detection of Cytosolic Ca^{2+} levels 39
2.8 Detection of ER Ca^{2+} levels 39
2.9 Detection of mitochondrial ATP levels 39
2.10 Cytosolic pyruvate to lactate ratio measurements 40
2.11 Measuring ROS in mitochondria and the cytosol 40
2.12 Experiments involving the translocation of GFP-NFATc3 and Ca^{2+} dynamics under UV light stimulation. 41
2.13 Quantification of Cytosolic Ca^{2+} Oscillation 42
2.14 Measurements of Mitochondrial Membrane Potential 42
2.15 ER-Mitochondria Co-Localization and 3D-Morphological Analysis of Mitochondria 43
2.16 Morphological analysis of mitochondria imaged with SIM 44
2.17 Cristae Membrane Kinetics Quantification 44
2.18 Evaluation of MCU shuttling to IBM 44
2.19 Electron microscopy 45

2.20 Analysis of Cristae Membrane, Density, and Cristae Density Distribution 46
2.21 Analysis of the Immunogold Staining 47
2.22 Proximity Ligation Assay 47
2.23 Western Blot 48
2.24 Co-Immunoprecipitation 49
2.25 Chemical cross-linking 50
2.26 Cisplatin and VBIT-4 Treatment 51
2.27 VDAC1 cluster size experiments and analysis 51
2.28 Flow Cytometry 51
2.29 Mitochondria Isolation 52
2.30 Patch clamp of intact mitochondria 53
2.31 Statistical Analysis and Reproducibility 54
3 Results 55
3.1 Impact of Near-UV light-induced Ca^{2+} oscillations on nuclear migration of NFATc3. 55
3.1.1 IP_3 generating agonist induces bi-phasic nuclear migration of NFATc3. 55
3.1.2 Near-UV light induces cytosolic Ca^{2+} oscillations via L-Type Ca^{2+} channel which activates nuclear migration of NFATc3. 58
3.1.3 Near-UV light generates ROS production in the cytosol and mitochondria which fires the Ca^{2+} oscillations and the nuclear migration of NFATc3. 61
3.1.4 Subplasmalemmal mitochondria buffers Near-UV light-induced Ca^{2+} oscillations and diminish nuclear translocation of NFATc3 64
3.2 Modulation of the Sigma-1 Receptor activity controls the cancer cell energy metabolism. 68
3.2.1 Sigma-1 Receptor expression differs in lung carcinoma and breast cancer cells. 68
3.2.2 Pharmacological modulation of Sigma-1 Receptor activity regulates mitochondrial bioenergetics: Activation enhances it, while inhibition has no impact. 69
3.2.3 Pharmacological activation of Sigma-1 Receptor boosts mitochondrial membrane potential and reduces aerobic glycolysis, while its inhibition enhances glycolysis. 72
3.2.4 Activation of Sigma-1 Receptor with agonist enhances mitochondrial Ca^{2+} access capacity. 74
3.3 Role of AnxA5 on mitochondrial Ca^{2+} homeostasis and apoptosis 79
3.3.1 AnxA5 regulates the mitochondrial matrix Ca^{2+} homeostasis 79
3.3.2 Depletion of AnxA5 does not influence Ψ_{mito} and expression level of Ca^{2+} uniporter machinery 84
3.3.3 AnxA5 depletion has no impact on MAMs but alters the structure of mitochondria 85
3.3.4 AnxA5 localizes both at the OMM and within mitochondria 88
3.3.5 AnxA5 controls the IMS Ca^{2+} signaling upon IP_3-induced ER Ca^{2+} release 89
3.3.6 AnxA5 actively influences the IMM dynamics through its modulation of IMS Ca^{2+} homeostasis. 93

3.3.7 AnxA5 resides close to VDAC1 and accumulates in the OMM in response to ER Ca^{2+} release. 97
3.3.8 AnxA5 modulates the open probability of an OMM channel 100
3.3.9 Annexin 5-VDAC1 interaction serves as a protective mechanism, safeguarding against VDAC1 dimerization during cisplatin-induced cell death 102
4 Discussion 108
4.1 General Outlook 108
4.1.1 Near UV-induced ROS production activates L-type Ca^{2+} oscillation to fire nuclear migration of NFATc3 109
4.1.2 Sigma1 Receptor activations enhance mitochondrial bioenergetics in cancer cells 114
4.1.3 AnxA5 is essential for VDAC1-dependent mitochondrial Ca^{2+} signaling and plays a critical role in regulating apoptotic cell death 116
4.2 Future Perspectives 121
5 References 123

List of Abbreviations

AIF	Apoptosis-inducing factor
AnxA5	Annexin A5
AnxA6	Annexin A6
AnxA7	Annexin A7
ATP	Adenosine triphosphate
CFP	Cyan fluorescent protein
Cyto-c	Cytochrome c
EMRE	Essential MCU regulator
ER	Endoplasmic reticulum
ERAD	ER-associated degradation
ETC	Electron transport chain
FRET	Förster resonance energy transfer
GPCRs	Glucose-regulated protein 75
GRP75	G protein-coupled receptors
GSK3	Glycogen Synthase Kinase 3
HK-1	Hexokinase 1
IBM	Inner boundary membrane
IMM	Inner mitochondrial membrane
IMS	Intermembrane space
IP_3R	Inositol 1,4,5-trisphosphate receptors
IP_3	Inositol trisphosphate
IDH	Isocitrate dehydrogenase
kDa	Kilodalton
LDH	Lactate dehydrogenase
KDH	α-Ketoglutarate dehydrogenase
MAM	Mitochondria associated ER membrane
MCU	Mitochondrial Ca^{2+} uniporter
MCUb	Mitochondrial Ca^{2+} uniporter, dominant negative form
MCUC	Mitochondrial Ca^{2+} uniporter complex
MCUR1	Mitochondrial Ca^{2+} Uniporter Regulator 1
MICU 1-3	Mitochondrial Ca^{2+} uptake 1-3

NCLX	Na^+/Ca^{2+} exchanger
NFAT	Nuclear Factor of Activated T cell
NLS	Nuclear localization signal
OMM	Outer mitochondrial membrane
OXPHOS	Oxidative phosphorylation
PDH	Pyruvate dehydrogenase
PA	Phosphatidic acid
PDC	Pyruvate dehydrogenase complex
PE	Phosphatidylethanolamine
PIP2	Phosphatidylinositol 4,5-bisphosphate
PI	Phosphatidylinositol
PLA	Proximity ligation assay
PLC-β	Phospholipase C β-type
PL	Phospholipid
PM	Plasma membrane
PMCA	Plasma membrane Ca^{2+}-ATPase
PRMT1	Protein arginine N-methyltransferase 1
PS	Phosphatidylserine
ROS	Reactive oxygen species
S1R	Sigma-1 receptor
SERCA	Sarco/endoplasmic reticulum Ca^{2+}-ATPase
SOCE	Store operated Ca^{2+} entry
STIM1	Stromal interaction molecule 1
UCP1-3	Uncoupling protein 1-3
UV	Ultraviolet
VDAC	Voltage-dependent anion channels
YFP	Yellow fluorescent protein

Abstract

Calcium ions (Ca^{2+}) serve as versatile second messengers that play a pivotal role in cellular functions. Cells finely tune the temporal Ca^{2+} concentration in specific organelle contact sites or subcellular domains to regulate gene expression, mitochondrial bioenergetics, and apoptosis. Among various Ca^{2+}-activated proteins, calcineurin regulates the nuclear translocation of the nuclear factor of the activated T-cells (NFAT) family, which controls the expression of several genes involved in cell growth and proliferation. The relationship between spatial Ca^{2+} kinetics and NFAT migration dynamics was previously elucidated through simultaneous tracking of fluorescent protein-tagged NFATs and, the Ca^{2+} using Fura2-AM. However, possible side effects may occur when using the Ultraviolet (UV) wavelength range which is commonly used for Fura2-AM measurements. In my first publication, I studied the nuclear translocation of NFATc3 and the Ca^{2+} dynamics upon ER Ca^{2+} release in pancreatic β-cells. These measurements revealed that the near-UV light (405nm) used to track Ca^{2+} ions, induces ROS production, which, in turn, activates L-type Ca^{2+} channels. The activation of L-type Ca^{2+} channels by reactive oxygen species (ROS) requires a certain threshold, which generates repetitive cytosolic Ca^{2+} oscillation, thereby inducing the nuclear migration of NFATc3. By targeting mitochondria to the plasma membrane to buffer subplasmelemal Ca^{2+}, I showed that ROS-induced cytosolic Ca^{2+} oscillations, not ROS themselves, trigger NFATc3 nuclear import. In my second publication, I investigated the contribution of the Sigma-1 receptor (S1R) to cancer cell energy metabolism. S1R, localized at ER-mitochondria contact sites, modulates the inositol 1,4,5-trisphosphate receptors (IP_3Rs) activity, thereby regulating Ca^{2+} signaling between the ER and mitochondria. SR1 is upregulated in various cancers, and the development of S1R ligands with potential antitumor properties is of great interest. While altering S1R pharmacologically affects tumor cell proliferation, the impact of S1R ligands on cancer cell energy metabolism remains unclear. I examined the impact of S1R on mitochondrial bioenergetics in its basal, activated, and inhibited states. The pharmacological activation of S1R enhances oxidative phosphorylation in S1R-expressing cancer cells, reducing their reliance on aerobic glycolysis by promoting increased mitochondrial Ca^{2+} levels. Moreover, S1R does not significantly contribute to mitochondrial bioenergetics under basal conditions. Overall, S1R plays a pivotal role in cancer energy metabolism, and the utilization of S1R ligands can be considered a promising approach to manipulate this process. In my third publication, I studied the involvement of AnnexinA5 (AnxA5) in mitochondrial Ca^{2+} homeostasis. AnxA5, a Ca^{2+}-dependent phospholipid binding protein, has been proposed to regulate intracellular Ca^{2+} levels, but the role of AnxA5 in mitochondrial Ca^{2+} signaling was previously unknown. This research revealed that AnxA5 plays a key role in controlling the

intermembrane space (IMS) Ca^{2+} signaling upon ER Ca^{2+} release. By positioning itself close to voltage-dependent anion channel 1 (VDAC1), AnxA5 modulates the Ca^{2+} permeability of VDAC1. Furthermore, these findings demonstrate that AnxA5's localization near VDAC1 controls excessive VDAC1 oligomerization, thereby regulating cell death in response to cisplatin treatment. These results suggest that the strategic localization of AnxA5 within the VDAC1 microenvironment governs proper IMS Ca^{2+} signaling while also safeguarding against apoptotic cell death. Collectively, this dissertation elucidates the mechanism by which near-UV light affects the nuclear migration of NFATc3, investigates S1R's influence on mitochondrial energy metabolism in cancer cells, and explores the role of AnxA5 in regulating the Ca^{2+} permeability of VDAC1 and oligomerization of VDAC1.

Zusammenfassung

Kalziumionen (Ca^{2+}) dienen als vielseitige Botenstoffe, die eine zentrale Rolle für die Zellfunktionen spielen. Zellen stimmen die zeitliche Ca^{2+}-Konzentration an spezifischen Organellen-Kontaktstellen oder subzellulären Domänen fein ab, um die Genexpression, die mitochondrielle Bioenergetik und die Apoptose zu regulieren. Unter den verschiedenen Ca^{2+}-aktivierten Proteinen reguliert Calcineurin die nukleare Translokation der nuclear factor of activated T-cells (NFAT)-Familie, die die Expression mehrerer Gene steuert, die an Zellwachstum und -proliferation beteiligt sind. Die Beziehung zwischen der räumlichen Ca^{2+}-Kinetik und der NFAT-Migrationsdynamik wurde zuvor durch die gleichzeitige Verfolgung von mit fluoreszierenden Proteinen markierten NFATs und Ca^{2+} mit Fura2-AM aufgeklärt. Allerdings können bei der Verwendung des ultravioletten (UV) Wellenlängenbereichs, der üblicherweise für Fura2-AM-Messungen verwendet wird, Nebenwirkungen auftreten. In meiner ersten Veröffentlichung untersuchte ich die Kerntranslokation von NFATc3 und die Ca^{2+}-Dynamik bei der Freisetzung von ER-Ca^{2+} in β-Zellen der Bauchspeicheldrüse. Bei diesen Messungen konnte gezeigt werden, dass das Nah-UV-Licht (405 nm), das zur Verfolgung von Ca^{2+}-Ionen verwendet wird, die ROS-Produktion anregt, die wiederum den L-Typ Ca2+-Kanal aktiviert. Die Aktivierung des L-Typ- Ca^{2+}-Kanals erfordert einen bestimmten ROS-Schwellenwert, der eine wiederholte zytosolische Ca^{2+}-Oszillation erzeugt und dadurch die Kernwanderung von NFATc3 auslöst. Durch das Fixieren von Mitochondrien an die Plasmamembran, wurde das subplasmales Ca^{2+} gepuffern, und es konnte gezeigt werden, dass ROS-induzierte zytosolische Ca^{2+}-Oszillationen und nicht ROS selbst den NFATc3-Kernimport auslösen. In meiner zweiten Veröffentlichung untersuchten ich den Beitrag des Sigma-1-Rezeptors (S1R) zum Energiestoffwechsel von Krebszellen. Der S1R, der an den Kontaktstellen zwischen ER und Mitochondrien lokalisiert ist, moduliert die Aktivität der Inositol-1,4,5-Trisphosphat-Rezeptoren (IP3Rs) und reguliert dadurch die Ca^{2+}-Signalübertragung zwischen ER und Mitochondrien. SR1 ist bei verschiedenen Krebsarten hochreguliert, und die Entwicklung von S1R-Liganden mit potenziellen Antitumoreigenschaften ist von großem Interesse. Während die pharmakologische Veränderung von S1R die Proliferation von Tumorzellen beeinflusst, ist der Einfluss von S1R-Liganden auf den Energiestoffwechsel von Krebszellen noch unklar. Ich untersuchte die Auswirkungen von S1R auf die mitochondrielle Bioenergetik in ihrem basalen, aktivierten und inhibierten Zustand. Die pharmakologische Aktivierung von S1R steigert die oxidative Phosphorylierung in S1R-exprimierenden Krebszellen und verringert deren Abhängigkeit von der aeroben Glykolyse, indem sie erhöhte mitochondrielle Ca^{2+}-Spiegel fördert. Darüber hinaus trägt der S1R unter basalen Bedingungen nicht wesentlich zur mitochondriellen Bioenergetik bei. Insgesamt spielt

der S1R eine zentrale Rolle im Energiestoffwechsel von Krebs, und die Verwendung von S1R-Liganden kann als vielversprechender Ansatz zur Beeinflussung dieses Prozesses angesehen werden. In meiner dritten Veröffentlichung untersuchten wir die Beteiligung von AnnexinA5 (AnxA5) an der mitochondriellen Ca^{2+}-Homöostase. AnxA5, ein Ca^{2+}-abhängiges phospholipidbindendes Protein, wurde beschrieben den intrazellulären Ca^{2+}-Spiegel regulieren, aber die Rolle von AnxA5 in der mitochondriellen Ca^{2+}-Signalgebung war bisher unbekannt. Meine Forschungen ergaben, dass AnxA5 eine Schlüsselrolle bei der Kontrolle der Ca^{2+}-Signalgebung im Intermembranraum (IMS) bei der Freisetzung von ER- Ca^{2+} spielt. Indem es sich in der Nähe von voltage-dependent anion channel 1 (VDAC1) positioniert, moduliert AnxA5 die Ca^{2+}-Permeabilität von VDAC1. Darüber hinaus zeigen unsere Ergebnisse, dass die Lokalisierung von AnxA5 in der Nähe von VDAC1 die übermäßige Oligomerisierung von VDAC1 kontrolliert und dadurch den Zelltod als Reaktion auf die Behandlung mit Cisplatin reguliert. Diese Ergebnisse deuten darauf hin, dass die strategische Lokalisierung von AnxA5 in der VDAC1-Mikroumgebung die ordnungsgemäße IMS- Ca^{2+}-Signalgebung steuert und gleichzeitig den apoptotischen Zelltod verhindert.

Diese Dissertation klärt den Mechanismus auf durch den Nah-UV-Licht die Kernwanderung von NFATc3 beeinflusst, untersucht den Einfluss von S1R auf den mitochondriellen Energiestoffwechsel in Krebszellen und erforscht die Rolle von AnxA5 bei der Regulierung der Ca^{2+}-Permeabilität von VDAC1 und der Oligomerisierung von VDAC1.

1 Introduction

1.1 Intracellular Ca^{2+} homeostasis

Calcium ions (Ca^{2+}) are multifaceted second messengers that orchestrate cellular functioning. Their pivotal role is indispensable for preserving cellular homeostasis. Ca^{2+} signaling governs an array of cellular processes, including cell proliferation, signal transduction, mitochondrial bioenergetics, and apoptosis (1). Thus the delicate balance of intracellular Ca^{2+} levels is crucial for cellular well-being (1).

In non-excitable cells, the basal cytosolic and mitochondrial Ca^{2+} concentrations are tightly regulated to approximately 100 nM, while in the extracellular space, the Ca^{2+} concentration is about 1.8 to 2 mM (2). In the event of a need for Ca^{2+} to regulate cellular functions and mitochondrial bioenergetics, cells can utilize the Ca^{2+} reservoir known as the endoplasmic reticulum (ER), which contains Ca^{2+} ions at levels ranging from 500 µM to 700 µM (3). Similar to ER, lysosomal Ca^{2+} concentration is also between 400 to 600 µM (4).

Cells activate specialized channels to regulate intracellular Ca^{2+} concentrations. The ER, serving as the main Ca^{2+} store within the cells, facilitates this process through Inositol 1,4,5-trisphosphate receptors (IP_3Rs) (5). Upon activation of G protein-coupled receptors (GPCRs), GPCRs stimulate the Gq proteins to activate beta-type phospholipase C (PLC-β), which, in turn, hydrolyzes phosphatidylinositol 4,5-bisphosphate (PIP2) into inositol 1,4,5-trisphosphate (IP_3) (6). Subsequently, the IP_3 then binds to IP_3Rs in the ER membrane, inducing channel opening, and Ca^{2+} ions diffuse down this electrochemical gradient from the ER lumen to the cytosol (5). During this process, ER Ca^{2+} content significantly decreases, which is sensed by the N-terminal region of the ER-residing protein Stromal Interaction Molecules (STIM), triggering a conformational change (7). Through this function, STIM aggregates and migrates to the cell membrane to interact with pore-forming Orai channels (7). This interaction activates the Orai channels, leading to a Ca^{2+} influx from the extracellular space into the cytosol, consequently enhancing intracellular Ca^{2+} concentrations. This process is called Store-operated calcium entry (SOCE) (8). During this processes, intracellular Ca^{2+} concentration significantly increases, and Ca^{2+} is involved in several processes, including the activation of several transcription factors, the regulation of mitochondrial matrix-residing Ca^{2+}-sensitive NADH dehydrogenases, and the regulation of IMS-residing Ca^{2+}-sensitive metabolite shuttles (9–11).

High cytoplasmic Ca^{2+} concentrations can disrupt normal cellular processes and trigger various downstream signaling pathways including apoptosis (12). To counteract this, cells employ several efficient channels for clearing elevated cytosolic Ca^{2+} levels. One of the key players in this regulatory process is the Sarco/Endoplasmic Reticulum Calcium ATPase (SERCA), a member of the P-type ATPase family residing in the ER (13). SERCA plays a critical role in maintaining intracellular Ca^{2+} homeostasis by actively transporting Ca^{2+} ions from the cytosol back into the ER lumen, by utilizing ATP hydrolysis (13). This unique function enables SERCA to uphold low cytosolic Ca^{2+} levels and replenish the ER's calcium stores (14). In addition to SERCA, the Plasma Membrane Calcium ATPase (PMCA), another member of the P-type ATPase family located on the cell membrane, also contributes to the regulation of intracellular Ca^{2+} levels (15). PMCA hydrolyzes ATP molecules to pump cytosolic Ca^{2+} ions into the extracellular space, further aiding in the fine-tuning of intracellular Ca^{2+} levels. Furthermore, mitochondria play a crucial role in buffering substantial amounts of Ca^{2+} to ensure precise control of Ca^{2+} signaling (10). This buffering process predominantly occurs at specialized regions known as Mitochondrial-Associated ER Membranes (MAMs), where the ER and mitochondria are closely associated (16). At MAMs, Ca^{2+} concentrations can reach remarkably high levels, often exceeding 16 µM (16). Mitochondria serve as a pivotal buffer in this process, working diligently to maintain cellular Ca^{2+} homeostasis and ensuring that Ca^{2+} signaling is finely tuned and tightly regulated (10).

1.2 Impact of intracellular Ca^{2+} cycling on transcription factors

The regulation of transcription factors by Ca^{2+} is a fundamental mechanism in cellular signaling and gene expression control (17). When intracellular Ca^{2+} levels increase, it triggers a cascade of signaling events. One key mediator in this process is calmodulin, a Ca^{2+}-binding protein capable of activating various transcription factors (17). Calcineurin as a Ca^{2+}-activated phosphatase, plays a crucial role by dephosphorylating specific transcription factors, thereby modulating their activity (17). For example, the nuclear factor of activated T cells (NFAT) serves as a well-known target of this regulation. Under basal Ca^{2+} levels, NFAT family proteins remain in the phosphorylated form at the cytosol, by concealing their nuclear localization signals (NLS) (18). However, when cytosolic Ca^{2+} levels rise, Ca^{2+} binds to calmodulin and undergoes a conformational change (17). Next, Ca^{2+}-bound calmodulin activates calcineurin, which, in turn, dephosphorylates NFAT proteins, exposing their nuclear localization signal (NLS) and facilitating their translocation into the nucleus (18). In the nucleus, NFATs regulate multiple genes by binding to specific DNA sequences in their promoters thereby controlling the

expression level of proteins in a Ca^{2+}-dependent manner (19). After the regulation of genes, NFATs are re-phosphorylated by the nucleus-residing Glycogen Synthase Kinase 3 (GSK3), which masks their NLS, thus inducing the translocation of NFATs back into the cytosol (20).

NFAT proteins form a diverse family, encompassing five distinct members: NFATc1, NFATc2, NFATc3, NFATc4, and NFAT5 (21). Notably, these proteins exhibit varying patterns of nuclear translocation dynamics. NFATc3 demonstrates rapid nuclear localization dynamics, while NFATc2 exhibits slower but sustained nuclear. These distinctions underscore that different NFATs rely on distinct Ca^{2+} signaling profiles for their activation. In an elegant study, researchers unveiled the mechanisms governing the activation of NFATc2 and NFATc3 (22). NFATc2 activation was found to be associated with Ca^{2+} microdomains close to the ORai1 channel, while NFATc3 required the presence of both Ca^{2+} microdomains and an increase in nuclear Ca^{2+} levels. This discovery was unveiled through the manipulation of nuclear Ca^{2+} levels using parvalbumin-GFP, a Ca^{2+}-binding protein employed to buffer nuclear Ca^{2+} levels (22). By employing this technique, Kar et al. effectively showed the different translocation kinetics of NFATc2 and NFATc3, highlighting the pivotal role of nuclear Ca^{2+} levels in their regulatory mechanisms. Moreover, an interesting study explored the potential significance of mitochondrial Ca^{2+} cycling in governing the nuclear translocation of NFAT. To investigate this, they inhibited the extrusion of Ca^{2+} from mitochondria, and their subsequent observations demonstrated a marked decrease in the nuclear translocation of NFAT (23). These experiments underscored the crucial role of mitochondrial Ca^{2+} cycling in the regulation of cytosolic Ca^{2+} signaling, and consequently, in the control of transcription factors.

Simultaneous monitoring of Ca^{2+} ions using the cytosolic Ca^{2+} dye Fura2-AM and FP-tagged NFAT proteins has elucidated the dynamic connection between the nuclear migration of NFAT family members and intracellular Ca^{2+} kinetics. Studying NFAT translocation dynamics involves extended microscopic measurements with sequential excitation wavelengths, including near-UV light. Previous studies have noted potential side effects of near-UV light, commonly used for tracking intracellular Ca^{2+} levels with Fura2-AM. However, the potential artifacts of near-UV light on NFAT nuclear translocation kinetics had not been previously demonstrated. In my initial publication (Oflaz et al. 2021) (10), as I investigated how ER Ca^{2+} release influences the nuclear translocation kinetics of NFATc3 in pancreatic beta cells (INS-1), I observed that near-UV light, employed to track Ca^{2+}, triggers ROS production. Overproduction of ROS, in turn, activate the L-type Ca^{2+} channel, resulting in repetitive cytosolic Ca^{2+} oscillations that initiate NFATc3 migration to the nucleus. Our study reveals that it is the ROS-induced cytosolic Ca^{2+}

oscillations, rather than ROS themselves, that trigger NFATc3 migration in response to near-UV light (10).

1.3 Mitochondrial Ca^{2+} signaling

Mitochondrial Ca^{2+} uptake is tightly linked to the mitochondrial membrane potential (Ψmito), which facilitates efficient mitochondrial Ca^{2+} uptake by providing the driving force for ion influx generated by the respiratory chain (24). Upon intracellular Ca^{2+} elevation, Ca^{2+} ions initially pass through the outer mitochondrial membrane (OMM) via a pore-forming protein on the OMM called the Voltage-Dependent Anion Channel (VDAC) (25). There are three different isoforms of VDAC: VDAC1, VDAC2, and VDAC3 (26). Among the isoforms, VDAC3 exhibits the highest Ca^{2+} permeability, followed by VDAC2 and then VDAC1 (27). VDAC1 is the most abundant protein on the OMM (28) and is permeable for Ca^{2+} ions (25). However, later studies reported that the permeability of VDAC1 to Ca^{2+} ions is influenced by several proteins such as α-synuclein (αSyn) and B-cell lymphoma-extra large (Bcl-xL) (27,29). Interaction between VDAC1 and Bcl-xL has been shown to promote mitochondrial Ca^{2+} uptake (29). Similarly, αSyn interaction with VDAC1 facilitates the VDAC1-mediated Ca^{2+} flux (27). Additional studies have revealed that VDAC1 exclusively conveys apoptotic Ca^{2+} signals to the mitochondria, whereas VDAC2 and VDAC3 do not participate in this particular mechanism (30). VDAC1 significantly participates in mitochondrial Ca^{2+} signaling by localizing to the MAM regions. Studies have demonstrated a physical linkage between VDAC1 and IP_3R through GRP75. This IP_3R-GRP75-VDAC1 bridge facilitates efficient Ca^{2+} transfer to the mitochondria (Fig. 1) (30).

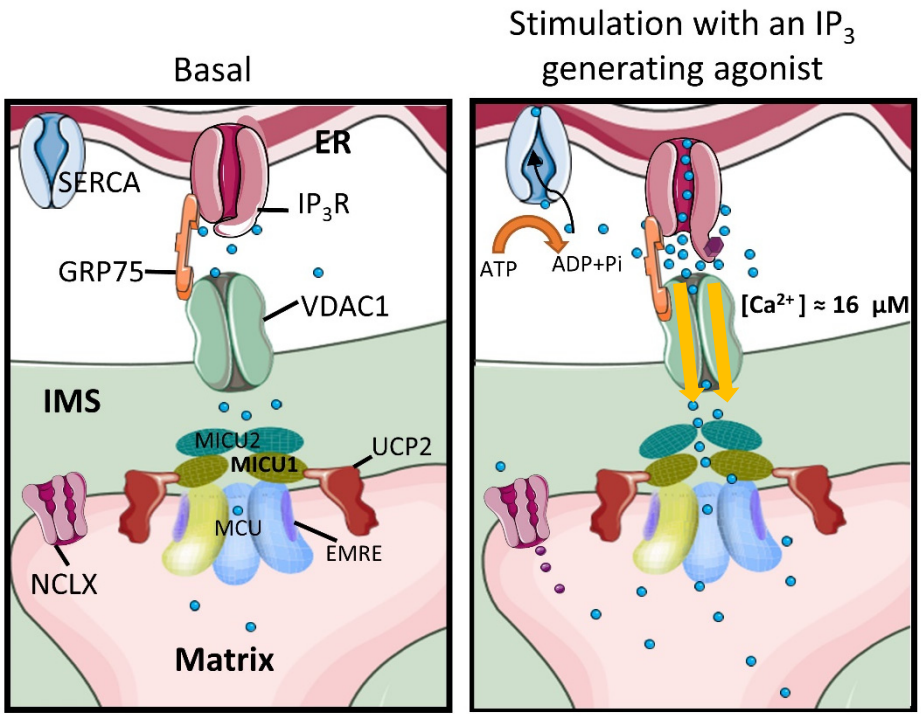

Figure 1. Simplified schematic illustrations of mitochondrial Ca^{2+} signaling at MAMs under basal conditions (left panel) and upon stimulation with an IP_3-generating agonist (right panel). The left panel, depicted as 'Basal,' illustrates the MAM regions, including proteins that play a role in Ca^{2+} signaling. Under basal conditions, IP_3R interacts with VDAC1 via GRP75. In the IMM, the regulation of MCUc is governed by the dimeric complex comprising MICU1/MICU2. This complex is suggested to function as a barrier, preventing excessive influx of mitochondrial Ca^{2+} when cytosolic Ca^{2+} levels are low. Upon stimulating the cells with an IP_3-generating agonist, IP_3 binds to IP_3R, leading to a flux of Ca^{2+} towards the OMM. Ca^{2+} ions pass through the OMM via VDAC1, and in the IMS, it reaches a certain threshold, subsequently de-oligomerizing MICU1 and allowing Ca^{2+} entry into the mitochondria. The efflux of Ca^{2+} ions from the matrix to the cytosol is mediated by the IMM-residing protein NCLX.

After passing through the OMM, Ca^{2+} ions enter the intermembrane space (IMS). The primary route for their passage through the inner mitochondrial membrane (IMM) is facilitated by the mitochondrial Ca^{2+} uniporter complex (MCUc) (31–36) (Fig. 1). The MCUc is a multi-subunit molecular assembly composed of various regulatory subunits, each with distinct functions. The Mitochondrial Ca^{2+} Uniporter (MCU) acts as the pivotal pore-forming subunit, creating a channel for Ca^{2+} ions to traverse into the mitochondrial matrix (Fig. 1) (31). The MCU Dominant-Negative β-Subunit (MCUb) operates as a negative regulator of the MCU (32). MCU Regulator 1 (MCUR1) serves as a scaffold factor by binding to both MCU and Essential MCU

Regulator (EMRE) (33), thereby facilitating critical interactions within the complex. EMRE contributes to the stability and assembly of the MCU complex with Mitochondrial Calcium Uptake (MICU) proteins (34). These MICU proteins, including MICU1, MICU2, and MICU3, collectively regulate MCU's Ca^{2+} permeability, acting as the gatekeepers for MCU (35). MICU1 and MICU2 are expressed in most mammalian tissues and together set the Ca^{2+} threshold for uniporter activity (35) while MICU3 has specific expression only in skeletal muscles and the central nervous system (CNS) (37). In its basal state, MICU1 forms hexamers; however, upon binding to Ca^{2+} through its EF-hand domains, it undergoes a disassembly process, transitioning into dimers with an EC_{50} of 4 μM Ca^{2+} and subsequently allowing Ca^{2+} entry to mitochondria (38).

In addition to its role in contributing to mitochondrial Ca^{2+} homeostasis, MICU1 has been demonstrated to regulate mitochondrial ultrastructure. A recent study identified MICU1 as an IMS Ca^{2+} sensor, mediating mitochondrial membrane dynamics independently of matrix Ca^{2+} levels (34). MICU1-depleted cells exhibited fragmented mitochondria with destructered cristae (39). Our group has shown that MICU1 is localized in the inner boundary membrane (IBM) and at the cristae junction, with the latter localization contributing to dynamic cristae membrane movements (40,41). Upon ER Ca^{2+} release MICU1 regulates cristae junction openings to facilitate the transfer of cristae-localized MCU to the IBM, enabling effective bi-phasic mitochondrial Ca^{2+} uptake. Additionally, by strategically localizing in the cristae junction, MICU1 controls spatial membrane potential which will be further explained in the following section (42).

When mitochondrial Ca^{2+} levels increase, mitochondria extrude Ca^{2+} ions from the mitochondrial matrix into the cytosol through the mitochondrial $Na^+/(Li^+)/Ca^{2+}$ exchanger (NCLX) which is localized in the IMM (43). This specialized extrusion system is powered by the electrochemical gradient for Na^+ entry into the mitochondria (43,44). The stoichiometry of Na^+:Ca^{2+} exchange remains a subject of debate, as various studies propose different ratios, with some suggesting a 2:1 stoichiometry (45) and others proposing a 3:1 ratio (46). This discrepancy implies that either 2 or 3 Na^+ ions enter the matrix for every 1 Ca^{2+} ion that exits it (Fig. 1). Research demonstrated that NCLX is essential for mitochondrial Ca^{2+} homeostasis, and its deletion in adult mouse hearts results in sudden death and heart failure, highlighting the critical role of the mitochondrial Ca^{2+} efflux machinery in cellular function (47).

1.4 Role of UCPs on mitochondrial Ca^{2+} uptake and uncoupling

The Electron Transport Chain (ETC) is an important complex for mitochondrial function, responsible for pumping protons across the IMM into the IMS to establish an electrochemical gradient (48). This gradient serves as a source of potential energy that drives the generation of (Adenosine Triphosphate) ATP by ATP synthase (49). However, not all protons in this gradient are used for ATP generation instead some protons leak back into the matrix without contributing to the ATP synthesis (50). This controlled dissipation of the proton gradient by Uncoupling Proteins 1, 2, and 3 (UCP1), (UCP2), and (UCP3) is important for maintaining mitochondrial function and preventing hyperpolarization of the IMM, which can lead to the production of excessive amounts of ROS (51). In addition to their significant role in mitochondrial uncoupling, UCPs have also been shown to play a pivotal role in regulating mitochondrial Ca^{2+} homeostasis (52,53).

The role of UCPs in mitochondrial Ca^{2+} uptake and uncoupling has been debated for a long time. Our lab was the first to demonstrate the involvement of UCP2 and UCP3 in mitochondrial Ca^{2+} uptake (53). Subsequent studies revealed the source-selective impact of UCP2 on mitochondrial Ca^{2+} uptake. Depletion of UCP2 reduces mitochondrial Ca^{2+} uptake upon ER Ca^{2+} release but does not affect SOCE (54). Conversely, overexpression of UCP2 enhances mitochondrial Ca^{2+} sequestration upon ER Ca^{2+} release and SOCE. Follow-up studies elucidated the mechanism of UCP2 involvement, where, in cancer and aging cells, MICU1 undergoes methylation by protein arginine methyltransferases 1 (PRMT1), resulting in reduced sensitivity to Ca^{2+} ions (36). Our group has demonstrated that UCP2 and UCP3 facilitate mitochondrial Ca^{2+} uptake by binding to methylated MICU1, thereby restoring its Ca^{2+} threshold in both cancer and aging cells. Thus, UCP2 and UCP3 serve as a sensitizer for mitochondrial Ca^{2+} sequestration under the conditions of high PRMT1 methylation (36). The subsequent investigations resolved how the interaction between UCP2 and MICU1 mediates mitochondrial uncoupling by employing super-resolution microscopy (42).

UCP2 is hypothesized to facilitate uncoupling through its fatty acid flippase activity, which suggests that a protonated fatty acid moves across the inner mitochondrial membrane to release its proton to the matrix (55). While this mechanism has been demonstrated in artificially created liposomes, direct uncoupling of the mitochondrial proton gradient by UCP2 has yet to be conclusively established. To understand UCP2-mediated mitochondrial uncoupling, it's crucial to consider the interaction of UCP2 and methylated MICU1 and the sub-mitochondrial localization of both (39). It has been demonstrated that UCP2 is uniformly distributed across the IMM, while MICU1 is primarily localized at the IBM and the cristae junctions (Fig. 2). This

specific localization of MICU1 at the cristae junctions effectively isolates the cristae, trapping the protons within the cristae lumen leading to unequal dissemination of potential across the IMM (Fig. 2) (42). The spatial opening of cristae junctions during ER Ca^{2+} release results in the diversion of the proton motive force from its exclusive role in ATP generation. Instead, it dissipates into the IMS and subsequently traverses through VDACs on the OMM into the cytosol (Fig. 2) (42). This mechanism is intensely under the control of UCP2. The absence of UCP2 in cancer and aging cells results in a shift in EC_{50} of MICU1 de-oligomerization from 4 µM to 14.0 µM of Ca^{2+}, which impairs cristae junction permeability during ER Ca^{2+} signaling and thus abolishes the dissemination of mitochondrial membrane potential in these cells (36,42,56).

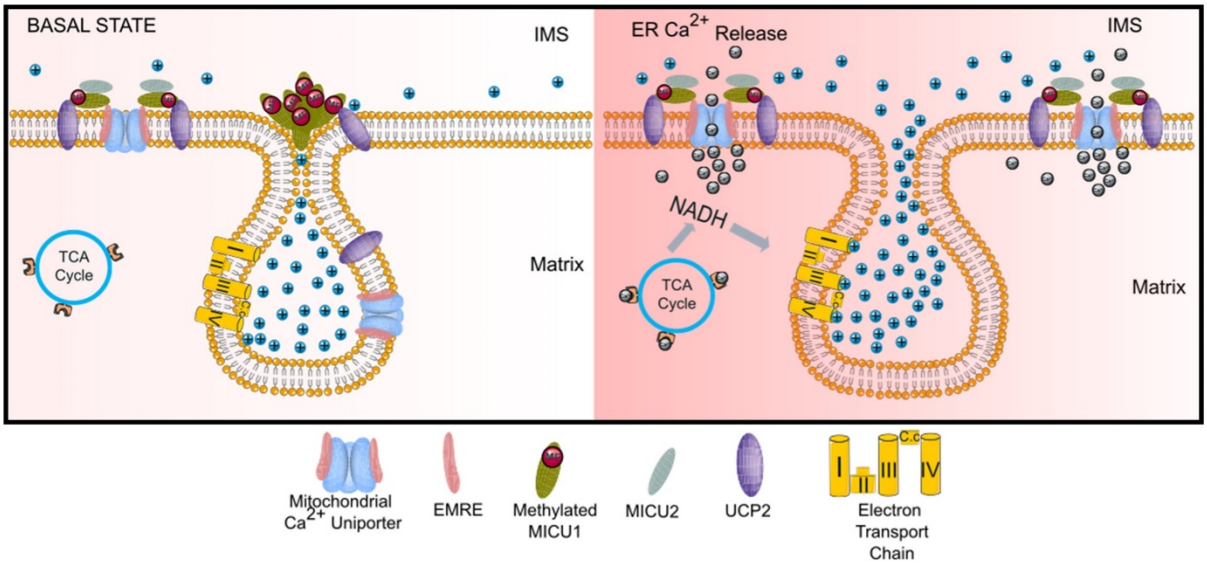

Figure 2. The strategic role of UCP2 in mitochondrial uncoupling. Under basal conditions, methylated MICU1 (it has a reduced Ca^{2+} sensitivity) is localized at the cristae junction to retain protons within the cristae lumen (left panel). UCP2 interacts with methylated MICU1 and pseudo-normalizes its Ca^{2+} sensitivity. Upon ER Ca^{2+} release, MICU1 undergoes de-oligomerization, resulting in the spatial opening of cristae junctions and the subsequent dissipation of protons from the cristae into the IMS (right panel). Figure is taken from my own publication (Oflaz et al. 2023) (56).

Unlike UCP2, UCP1-mediated uncoupling is well-established to rely on the availability of long-chain fatty acids. In this process, protonated long-chain fatty acids bind to the substrate binding site of UCP1, located on the IMM side facing the cristae lumen (57). Consequently, when a conformational change occurs, the substrate binding site becomes exposed to the matrix side of the IMM, leading to the release of protons (Fig. 3) (57). A recent study has unveiled a novel role of UCP1 in mitochondrial uncoupling in brown adipose tissues. In this study, authors showed that UCP1 enhances mitochondrial Ca^{2+} uptake following adrenergic stimulation via

forming a complex with the MCU through its interaction with the EMRE (Fig. 3) (58). This interaction is heightened in response to cold or adrenergic stimulation, resulting in increased mitochondrial Ca^{2+} uptake (Fig. 3). Intriguingly, MICU1 serves as a negative regulator in this interaction by competing for binding to EMRE. These findings offer a novel perspective on mitochondrial uncoupling. During adrenergic stimulation, the formation of the UCP1-EMRE-MCU complex enhances mitochondrial Ca^{2+} uptake, subsequently boosting the activity of Ca^{2+}-sensitive dehydrogenases in the tricarboxylic acid (TCA) cycle (Fig. 3) (58). Consequently, this process leads to increased NADH production and the release of a significant amount of proton into the IMS (58). In the presence of fatty acids, these protons are then uncoupled via UCP1 within the cristae (Fig. 3).

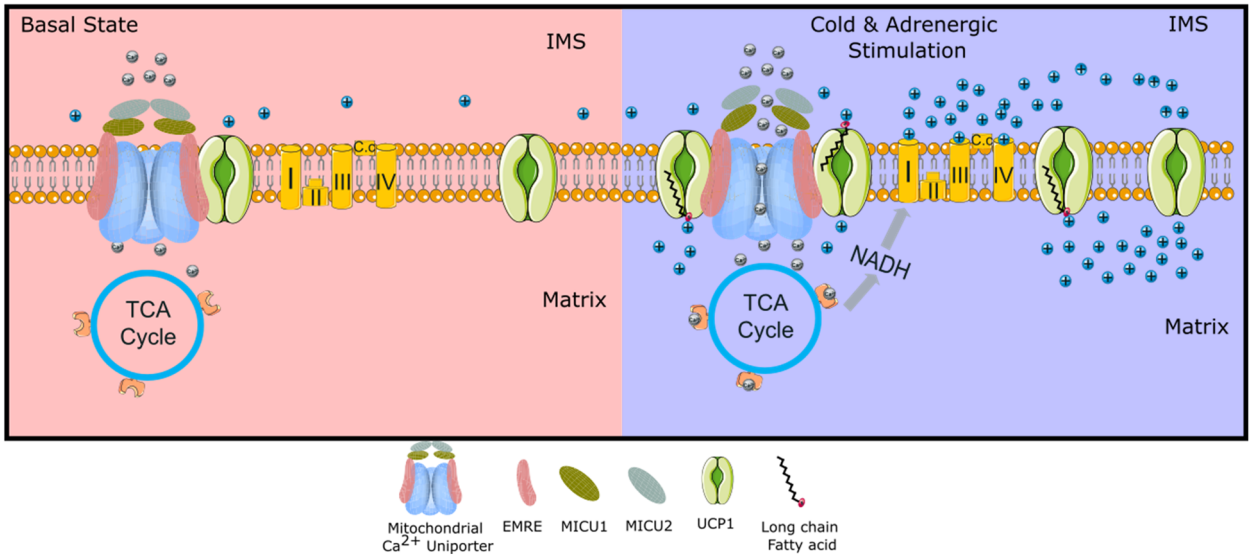

Figure 3. The interaction of UCP1 with MCU contributes to mitochondrial uncoupling. Under basal conditions, UCP1 interacts with EMRE (left panel). Cold exposure or adrenergic stimulation increases UCP1 expression and its interaction with EMRE, enhancing mitochondrial Ca^{2+} uptake (right panel). This boosts TCA cycle activity, NADH production, and proton accumulation in the IMS, promoting highly effective proton conductance through the UCP1 (right panel). Figure is taken from my own publication (Oflaz et al. 2023) (56).

In my most recent first-authored review paper (Oflaz et al. 2023) (56), we conducted an in-depth discussion of the distinct molecular mechanisms that underlie mitochondrial uncoupling mediated by UCP1 and UCP2 (56). In summary, both UCP1 and UCP2 proteins interact with the MCU and contribute to mitochondrial Ca^{2+} homeostasis and uncoupling through different mechanisms. Specifically, UCP2 interacts with methylated MICU1 to adjust its Ca^{2+} sensitivity, promoting the opening of cristae junctions and the release of protons into the cytosol (56). On

the other hand, UCP1 interacts with the EMRE to enhance mitochondrial Ca^{2+} uptake, thereby boosting the activity of the TCA cycle and increasing mitochondrial uncoupling (56).

1.4 Deciphering the role of Ca^{2+} in mitochondrial bioenergetics

The intricate interplay between Ca^{2+} and mitochondrial bioenergetics is the focus of extensive research due to its profound implications for health and disease. ATP production is a fundamental requirement for the survival and functionality of all cells, including cancer cells (59). However, a notable distinction exists in the ATP production pathways between healthy and cancerous cells. Healthy cells predominantly rely on oxidative phosphorylation (OXPHOS) for ATP generation, whereas cancer cells often prefer aerobic glycolysis (60). This increased dependence on aerobic glycolysis, despite being less efficient in terms of ATP production per glucose molecule, offers numerous benefits to cancer cells. These advantages include the rapid generation of energy and the production of metabolic intermediates that facilitate the increased growth and proliferation of biomass (61). It is important to note that cancer cells display varying degrees of metabolic heterogeneity, and the level of glycolysis versus OXPHOS can vary among different cancer types and even within the same tumor (62). This variability suggests that cancer cells do not exclusively depend on aerobic glycolysis but also generate a certain amount of ATP. In this context, our group has developed a protocol to discern the reliance of different cancer cells on aerobic glycolysis versus OXPHOS, revealing distinct metabolic profiles and activities at the single-cell level (59). For example, when comparing different cancer cell types, we observe variations in their metabolic preferences. HeLa cells, originating from cervical cancer, and A549 cells, derived from lung cancer, predominantly favor aerobic glycolysis as their primary ATP generation pathway. In contrast, MCF7 breast cancer cells exhibit a relatively higher reliance on OXPHOS compared to HeLa and A549 cells, emphasizing the diversity in metabolic strategies among these cancer cell lines (59).

Cells utilize glucose to generate ATP through two primary pathways: glycolysis and OXPHOS. Once glucose enters the cell through glucose transporters (63), it undergoes a series of enzymatic reactions in the cytosol, resulting in the production of two molecules of pyruvate, along with the generation of 2 ATP and 2 NADH molecules (64). The fate of pyruvate is contingent on the cell's metabolic demands. In OXPHOS, pyruvate is transported into the mitochondria through the VDAC1 in the OMM and the mitochondrial pyruvate carrier in the IMM (65). Within the mitochondrial matrix, pyruvate is enzymatically converted into acetyl-CoA by the pyruvate dehydrogenase complex (PDC). Notably, the activity of PDC is indirectly

regulated by Ca^{2+}, where Ca^{2+} activates pyruvate dehydrogenase phosphatase (PDP), leading to the dephosphorylation and activation of pyruvate dehydrogenase (PDH) (66). Generated Acetyl-CoA subsequently enters the TCA cycle. In the TCA cycle, the activities of α-ketoglutarate dehydrogenase (KDH) and isocitrate dehydrogenase (IDH) are also regulated by Ca^{2+} ions (67). Therefore, an increased concentration of Ca^{2+} within the mitochondrial matrix enhances the activity of Ca^{2+}-dependent members of the TCA cycle, leading to the enhanced generation of the electron donors NADH and FADH2 and subsequently more ATP production (68). In addition to the Ca^{2+}-sensitive dehydrogenases in the mitochondrial matrix that regulate ATP production, our laboratory has revealed the influence of basal Ca^{2+} levels within the IMS on mitochondrial bioenergetics. This effect is mediated through the Ca^{2+}-binding component of the malate-aspartate shuttle, known as citrin (11).

In the ETC, NADH and FADH2 serve as critical electron carriers, transporting high-energy electrons to the chain's protein complexes. The ETC is located in the IMM, residing within the cristae (69). ETC consists of several key protein complexes, including Complex I (NADH dehydrogenase), Complex II (Succinate dehydrogenase), Complex III (Cytochrome bc1 complex), and Complex IV (Cytochrome c oxidase) (67). Complexes I and II receive electrons from NADH and FADH2, respectively, initiating a sequential electron transfer process that leads to the pumping of protons across IMM. This process establishes a proton gradient, which is concentrated within the cristae lumen. In the next step, protons are harnessed by ATP synthase to generate ATP (69).

1.5 Contribution of Sigma-1 Receptor on mitochondrial bioenergetics in cancer cells

The Sigma-1 Receptor (S1R) stands as a pivotal membrane protein, localized on the ER membrane and enriched in the MAMs (40). Its presence can be detected in a wide range of tissues, encompassing the Central Nervous System, liver, lungs, and various cancer cells (70). This highlights its intricate participation in a multitude of cellular functions, including the modulation of ion channel activity, apoptosis, and the regulation of Ca^{2+} signaling (71). The groundbreaking discovery of S1R's contribution to Ca^{2+} signaling arose from the pioneering work of Tsung-Ping Su's laboratory. They unveiled the localization of S1R within the MAMs, forming a complex with the ER-resident chaperone, Binding immunoglobulin protein (BiP), under basal conditions (72). However, when confronted with ER stress or stimulated by its agonists, S1R dissociates from BiP and engages with a diverse array of proteins, including

IP_3R. The association with IP_3R, allows S1R to play a critical role in facilitating prolonged and efficient Ca^{2+} transfer to the mitochondria (72). In this regard, we have demonstrated that during ER stress, S1R plays a crucial role in enhancing mitochondrial bioenergetics, achieved by prolonging and intensifying the ER-to-mitochondria Ca^{2+} transfer (73).

S1R, distinguished by its dynamic positioning within the ER and its interactions with a wide range of proteins, stands out as a compelling candidate for the regulation of cancer cell metabolism. Notably, S1R exhibits increased expression in various cancer types, including lung, breast, prostate, and colon cancers (70,74). Among different cancer cells, S1R shows prominent expression in the lung (A549), followed by breast (MCF7), and colon cancer cell lines (9). To understand the S1R's role in cancer metabolism, numerous studies have explored the effects of S1R activation or inhibition through ligands (70,74). For instance, the activation of S1R with its agonist has reduced the proliferation of MDA-MB-231 breast cancer cells, notable for their robust S1R expression (70,74). In contrast, this effect was not observed in other breast cancer cell types, specifically MCF-7 and MCF-10A, owing to their lower S1R expression levels (70). While the pharmacological manipulation of the S1R has been shown to affect tumor cell proliferation, the impact of S1R ligands on cancer cell energy metabolism remains elusive. Therefore, I have investigated the impact of S1R on cancer cell energy metabolism in A549 and MCF7 cells under basal, activated, and inactivated conditions (Oflaz & Koshenov et al. 2022) (9). Our study revealed that pharmacological activation of S1R enhances mitochondrial bioenergetics and decreases their reliance on aerobic glycolysis by enhancing basal Ca^{2+} delivery to the mitochondrial matrix, particularly in highly S1R-expressing A549 cells (9). However, activation of S1R did not have an impact on the low-level S1R-expressing MCF7 cells. Collectively, our results emphasize the crucial role of S1R in cancer energy metabolism and indicate the potential for manipulating the cancer energy metabolism using S1R ligands (9).

1.6 Role of VDAC1 in mitochondrial-mediated apoptosis

The intrinsic pathway of apoptosis can be initiated by a diverse array of intracellular triggers, including mitochondrial Ca^{2+} overload, VDAC1 oligomerization, and oxidative stress. Upon apoptosis induction, key proapoptotic proteins resident in the IMS, such as Cytochrome C (Cyto-c), Apoptosis-Inducing Factor (AIF), and Smac/DIABLO, are released into the cytosol (75). Within the cytosol, Cyto-c engages with Apoptotic Protease Activating Factor-1 (Apaf-1), orchestrating the formation of the apoptosome, which, in turn, activates caspase-9 (75). As a catalytic keystone, caspase-9 initiates a cascade of downstream caspases, including caspase-

3 and caspase-7, ultimately leading the cell toward programmed cell death (75). Various models have been suggested for the mechanisms underpinning the release of IMS-residing proteins into the cytosol: 1: opening of the permeability transition pore upon mitochondrial Ca^{2+} overload (76), 2: the formation of a substantial channel on the OMM through BAX/BAK proteins (77), and 3: formation of a large channel via the homo-oligomerization of VDAC1 (78).

VDAC1 plays a pivotal role in mitochondrial-mediated apoptosis by enabling the release of proapoptotic proteins into the cytosol. It is essential to consider that the VDAC1 pore size is a mere 3.0 nm when contemplating the release of these proteins. (79). This dimension appears to be insufficient for the passage of large proteins like Cyto-c with a molecular weight of 12 kDa. However, upon exposure to apoptotic stimuli, VDAC1 undergoes homooligomerization, forming large protein-conducting channels capable of accommodating and facilitating the release of IMS-residing proapoptotic proteins (80). Numerous apoptotic triggers, including cisplatin, etoposide, selenite, H_2O_2, arsenic trioxide, staurosporine, and curcumin, have been demonstrated to induce the oligomerization of VDAC1 across various cell lines (12,80,81). Furthermore, it has been proposed that the negatively charged lipid microenvironment surrounding VDAC1 plays an additional role in promoting VDAC1 oligomerization during the apoptotic process (82). This suggests that the interplay between VDAC1 and its lipid surroundings contributes significantly to the intricate regulatory mechanisms of apoptosis (82).

VDAC1's oligomeric state plays a pivotal role in orchestrating mitochondria-mediated apoptosis (80). Notably, several VDAC1-interacting molecules and proteins have been identified as inhibitors of apoptosis, preventing excessive VDAC1 oligomerization during apoptotic stimulation. A recently developed VDAC1 oligomerization inhibitor, VBIT-4, has been shown to prevent VDAC1 oligomerization and apoptosis induced by various apoptotic triggers across multiple cell lines (80). Moreover, the interaction between Hexokinase-1 (HK-1) and VDAC1 has been shown to inhibit the release of Cyto-c and protect against apoptotic cell death (83). This protective function of HK-1 is attributed to its capacity to inhibit VDAC1 oligomerization (83). In line with these findings, in my latest study (Oflaz et al., 2023, under revision) (84), I have shown that Annexin A5 (AnxA5), a phospholipid-binding protein, plays a regulatory role in mitochondria-mediated apoptosis. It achieves this by positioning itself near VDAC1 and functions as a protective barrier, effectively restricting excessive VDAC1 oligomerization. As a result, this regulatory mechanism governs apoptotic cell death in response to cisplatin treatment (84). With these findings, we showed a multifunctional nature of AnxA5 on mitochondrial Ca^{2+} signaling and apoptosis.

1.7 Annexin-A5: structure, membrane binding, and contribution to Ca^{2+} homeostasis

Annexins comprise a family of 12 proteins involved in intracellular Ca^{2+} signaling. Annexins share a common structural framework, characterized by two primary domains: the short NH2-terminal 'head,' which exhibits variable characteristics, and the long COOH-terminal protein core, which remains evolutionarily conserved (85). The COOH-terminal protein core plays a crucial role by housing Ca^{2+} binding sites and facilitating membrane interactions. Conversely, the variability in the N-terminus among different annexins imparts specificity to their intracellular signaling functions (85).

AnxA5 is a soluble protein mainly localized in the cytosol. AnxA5 was the first member of the family whose crystal structure was characterized back in the early 1990s (86). AnxA5 consists of four repeating alpha-helical domains (Fig. 4). According to its structure, the convex side harbors Ca^{2+} binding sites, known as type II and type III sites which bind 10–12 Ca^{2+} ions (86), and in the presence of Ca^{2+} ions, this region binds to the membranes. In contrast, the concave side, where the *N*-terminus is located, faces away from the membrane, rendering it accessible for interactions with other proteins (Fig. 4) (86). Advancements in scientific techniques have provided deeper insights into the behavior of AnxA5 upon interacting with cellular membranes. Through the application of atomic force microscopy, researchers have uncovered that in the presence of high Ca^{2+} levels, AnxA5 molecules exhibit a capacity for self-assembly, forming intricate two-dimensional crystalline arrays on the membranes (87).

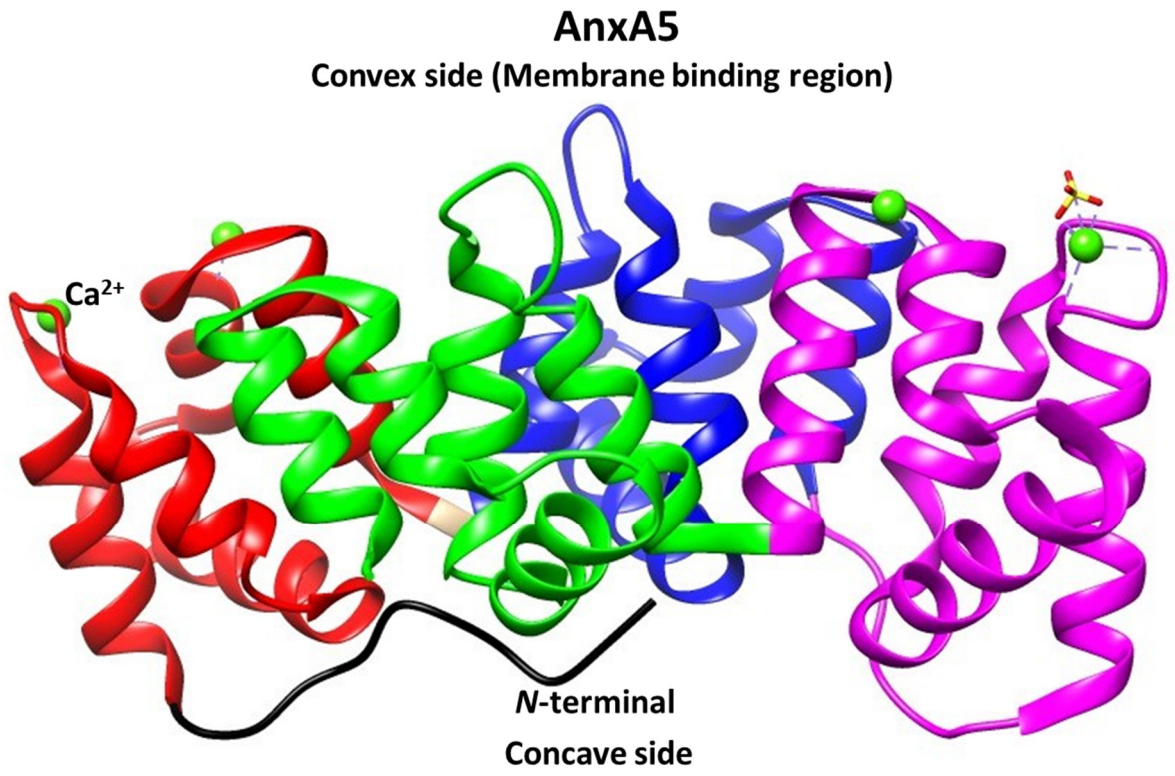

Figure 4: The crystal structure of AnxA5. The structure of AnxA5 comprises four repeating alpha-helical domains, each represented by a distinct color: red for Domain 1, blue for Domain 2, magenta for Domain 3, and green for Domain 4. The convex side of this structure houses the Ca^{2+} binding domains, while the concave side is formed by the N-terminus. Adapted from PDB (P08758) (86).

Within the annexin protein family, Ca^{2+}-dependent reversible PL binding is a common feature, yet each member exhibits distinct sensitivity to Ca^{2+} ions and displays preferences for different PL headgroups. AnxA5 serves as a notable example, as it has been shown to interact with various PLs, including cardiolipin, phosphatidylserine (PS), phosphatidylethanolamine (PE), phosphatidylinositol (PI), and phosphatidic acid (PA), with no observable binding in the absence of Ca^{2+} (86). Intriguingly, when AnxA5 engages with liposomes composed of PS and PE in the presence of Ca^{2+}, it forms strong associations with the membranes, with a dissociation constant (Kd) of 55 µM, underscoring its pivotal role in membrane repair (88). This function is particularly significant in response to elevated intracellular Ca^{2+} levels, where AnxA5 translocates and binds to ruptured cell membranes, contributing to the restoration of cell membrane integrity (87). Additionally, AnxA5's ability to self-assemble into two-dimensional arrays on membranes plays a crucial role in membrane repair (89). This self-assembly process not only stabilizes the membrane but also restructures it into a more ordered, gel-like phase, further enhancing its effectiveness in facilitating membrane repair (88)(89).

AnxA5's ability to bind to intracellular membranes and indirectly modulate the activity of Ca^{2+} channels and transporters is a subject of ongoing research and scientific inquiry. While there is evidence to suggest that AnxA5 may function by inserting itself into membranes and potentially acting as a Ca^{2+} channel, the precise mechanisms remain a topic of investigation. Studies have shown that AnxA5 can indeed be inserted into membranes under specific conditions, particularly at acidic pH levels (pH = 4.5), as observed in artificial membrane models (90). Moreover, experiments involving liposomes composed of PS have demonstrated AnxA5's capability to mediate Ca^{2+} influx (91). In a cellular context, AnxA5 has been implicated in facilitating Ca^{2+} influx across the plasma membrane, upon stimulation with high levels of H_2O_2 in the chicken DT40 cells (92). This phenomenon has been attributed to the insertion of AnxA5 into the cell membrane triggered by peroxide stimulation. However, despite these intriguing findings, the precise role of AnxA5 in cellular Ca^{2+} homeostasis remains incompletely understood. Further research is actively underway to uncover the specific mechanisms by which AnxA5 exerts its regulatory effects on Ca^{2+} transport, shedding light on its multifaceted functions in cellular physiology and signaling pathways.

1.8 Association of Annexin-A5 with Mitochondria

In addition to binding to the cellular membranes, several studies have indicated that AnxA5 can be associated with mitochondria. In the early 1990s association of cytosolic AnxA5 with mitochondria, has been demonstrated (93). Interestingly, in the same study, it was revealed that AnxA5 binds to a 27 kDa mitochondrial polypeptide (93). This observation led to the conclusion that AnxA5 may constitute a component of a larger protein complex located in the mitochondrial membranes (93). In a separate study, researchers examined the binding of AnxA5 to isolated mitochondria from rat liver. Their investigation revealed that AnxA5 binds not only to the OMM but also to the IMM. To gain insights into this binding, they conducted a comparative analysis of AnxA5 binding to these mitochondrial membranes and phospholipid vesicles. The results showed that AnxA5 binds to cardiolipin-rich vesicles with greater affinity which led them to propose that cardiolipin-rich microdomains within mitochondrial membranes serve as the likely binding sites for AnxA5 (94). Furthermore, it was observed that the binding of AnxA5 to isolated mitochondria requires physiological Ca^{2+} concentrations within the range of 0.1 µM to 10 µM (94). Based on these findings, the researchers suggested that AnxA5's interaction with mitochondrial membranes plays a regulatory role in modulating membrane-associated proteins (94). A subsequent study conducted by the same research group not only reaffirmed the binding of AnxA5 to mitochondrial cardiolipins but also demonstrated that the

binding of AnxA5 to cardiolipin-rich microdomains within mitochondrial membranes immobilizes these regions (95). Furthermore, AnxA5's interaction with mitochondrial membranes has been further elucidated in the context of apoptosis. Upon exposure to apoptotic stimuli, AnxA5 has been observed to undergo translocation to mitochondrial membranes. Despite extensive efforts to understand the function of AnxA5 on mitochondria, its specific role in these organelles remained elusive. In my latest paper (Oflaz et al. 2023, under review) (84), we revealed that AnxA5 localizes in the vicinity of VDAC1 to regulate the Ca^{2+}-permeable state of VDAC1. By doing so AnxA5 actively participates in IMS Ca^{2+} signaling.

1.9 A general overview

During my Ph.D. study, I focused on intracellular Ca^{2+} signaling and its impact on transcription factors, mitochondrial health, and mitochondrial Ca^{2+} homeostasis. I employed different techniques including fluorescent and super-resolution microscopy to dynamically monitor ion and metabolite flux within the single cells, using various genetically encoded organelle-targeted biosensors (Table 1). My research results are organized into three distinct perspectives on intracellular Ca^{2+} signaling.

Firstly, I investigated how various sources of intracellular Ca^{2+} signaling, specifically comparing ER Ca^{2+} release through IP_3R and the activation of the L-type Ca^{2+} channel on the cell membrane, impact the nuclear translocation of NFATc3 in pancreatic β-cell line, INS-1. During my investigation, I realized that near-UV light, typically used for Fura2-AM measurements to monitor Ca^{2+} signaling, generates a significant amount of ROS. The generation of ROS initiates the activation of L-type Ca^{2+} channels, resulting in sustained Ca^{2+} oscillations within the cytosol. These Ca^{2+} oscillations, in turn, activate the nuclear translocation of NFATc3 (Oflaz et al., 2021) (10).

Secondly, we explored the role of S1R in cancer cell energy metabolism. Our investigation revealed that S1R exhibits high expression in lung cancer cells, specifically A549, while its expression is notably lower in the breast cancer cell line MCF7. Furthermore, our findings demonstrated that the activation of S1R with its ligand significantly enhances mitochondrial bioenergetics in A549 cells but does not produce the same effect in MCF7 cells. We also uncovered the underlying mechanism behind this enhancement, showing that S1R activation increases mitochondrial Ca^{2+} uptake upon agonist-induced ER Ca^{2+} release, thereby facilitating directed Ca^{2+} flux from the ER to the mitochondria which in turn enhances the OXPHOS (Oflaz & Koshenov et al., 2022) (9).

Finally, my latest paper has uncovered a new function of AnxA5 in the context of mitochondrial Ca^{2+} signaling in perivascular, HeLa, and EA.hy926 cells. We found that AnxA5 is pivotal in regulating intramitochondrial Ca^{2+} signaling, upon ER Ca^{2+} release. It translocates to the OMM, where it influences VDAC1's Ca^{2+} permeability, maintaining optimal IMS Ca^{2+} levels. The localization of AnxA5 in the VDAC1 microenvironment shields against cell death in response to cisplatin treatment, by regulating VDAC1's oligomeric state. These findings enhance our understanding of AnxA5's multifaceted role in mitochondrial Ca^{2+} signaling and apoptosis. (Oflaz et al., 2023) (84).

Table 1. List of genetically encoded constructs used during this study

Name of the sensor	**What it detects**	**Characteristics**	**References**
mt.AT1.03	ATP	FRET-based ratiometric biosensors targeted to mitochondria.	(9)
Lapronic	Pyruvate/Lactate	Cytosolic FRET-based ratiometric biosensor.	(96)
GFP-NFATc3	Ca^{2+}-mediated nuclear translocation of NFATc3	GFP-tagged NFATc3.	Gift from Mark L. Dell'Acqua
AKAP-RFP-CAAX	Subplasmalemal localization of mitochondria	Anchor mitochondria to the cell membrane.	Gift from Gyorgy Hajnoczky
D3cpv and 4mtD3cpv	Ca^{2+}	Cytosolic and mitochondrial FRET-based ratiometric biosensors.	(96)
D1ER	Ca^{2+}	ER targeted FRET-based ratiometric biosensor.	(97)
IMS-GEM-GECO, ROMO-GEM-GECO	Ca^{2+}	Ratiometric biosensors targeted to IMS and Cristae.	(84,98)
GCaMP7c	Ca^{2+}	Intensiometric cytosolic Ca^{2+} sensor with high dynamic range.	(84)

mitoHyper7 and cytoHyper7	H_2O_2	Mitochondrial and cytosolic ratiometric biosensor.	(10)

2 Material Methods

This section has been partially adapted from the following articles (Oflaz et al. 2021) (10), (Oflaz & Koshenov et al. 2022) (9), and (Oflaz et al. 2023, under review) (84).

2.1 Cell Culture and Transfection

HeLa S3 cells (ATCC CCL-2.2), EA.hy926 cells (provided by Dr. C.J.S. Edgell, University of North Carolina, Chapel Hill, NC, USA), and perivascular cells (PCs) were generously supplied by Prof. Dr. Bent Brachvogel from the Center for Biochemistry, Faculty of Medicine, University of Cologne, Germany (84). A-549 and MCF-7 cells were procured from the cell culture facility of the Medical University of Graz and were cultured in DMEM (D5523, Sigma-Aldrich, Vienna, Austria) with 10% FCS (Gibco, Thermo Fisher Scientific), penicillin (100 U/ml), streptomycin (100 µg/ml), and amphotericin B (1.25 µg/ml) (Gibco) in a humidified incubator (37 °C, 5% CO2, 95% air) (9). Regular checks for mycoplasma contamination confirmed the absence of contamination (84).

The INS-1 832/13 (INS-1) cell line was graciously provided by Prof. Dr. Claes B. Wollheim and Dr. Françoise Assimacopoulos-Jeannet from the University Medical Center in Geneva, Switzerland (10). These INS-1 cells were cultivated in RPMI 1640 medium supplemented with 11 mM glucose (PubChem CID: 5793), 10 mM HEPES (PubChem CID: 23831), 10% fetal calf serum (FCS), 1 mM sodium pyruvate (PubChem CID: 23662274), 50 µM β-mercaptoethanol (PubChem CID: 1567), 1% (v/v) Pen Strep® (ThermoFischer, Vienna, Austria; 10,000 U/L), and 1.25 µg/mL Amphotericin B (ThermoFischer, Vienna, Austria; 250 µg/mL) (10).

For microscopy experiments, cells were cultured on either 30 mm glass coverslips or 1.5 H high-precision glass coverslips (Marienfeld-Superior). Transfection was performed when HeLa cells reached 40% confluence, PCs at 60% confluence, and EA.hy926 cells at 70-80% confluence. Cells were transfected with 1 µg of the respective plasmid (all plasmids used in this study are listed in table 1) using PolyJetTM transfection reagent (SignaGen Laboratories, Rockville, MD, USA) in 1 ml of full culture medium (84). Five hours after transfection, the medium was replaced with 2 ml of full culture medium (10). In the knockdown experiments, HeLa cells (50-60% confluence) were transfected using 3 µl of TransFast transfection reagent (Promega, Madison, WI, USA) in 1 ml of medium without serum and antibiotics for a duration of 14-16 hours (10). Following this, the transfection medium was substituted with 2 ml of complete culture medium (9). The experiments were conducted 40-48 hours following transfection. Prior to each experiment, cells were equilibrated to room temperature while

maintaining them in a storage buffer (84). For VDAC1 knockdown, the siRNA sequence used was ACACUAGGCACCGAGAUUA (siVDAC1, sense strands, 5′-3′), and a scrambled control siRNA with the sequence UUCUCCGAACGUGUCACGU (siControl, sense strands, 5′-3′) from Microsynth (Balgach, Switzerland) was employed (84). The efficacy of siVDAC1-induced knockdown was confirmed through Western blot analysis (84).

2.2 Generation of AnxA5-KO cells

To create AnxA5-KO HeLa cells, we obtained pcDNA3.3-Cas9-2A-eGFP and pGS-U6-gAnxA5 from Genscript (Thermo Fischer Scientific) (84). The gRNA sequence for AnxA5 is 5′-GATGCAGAAACTCTTCGGA -3′ (84). Subsequently, the plasmids were co-transfected into HeLa cells at a 1:1 ratio (84). After 48 hours of transfection, cells exhibiting GFP fluorescence were individually isolated into 96-well plates and subsequently cultured (84). Ultimately, approximately 50 clones underwent PCR analysis (84). To confirm the presence of mutations in both alleles of 5 selected clones, we created bacterial subclones from the amplified PCR fragments and performed sequencing using the Sanger method (Microsynth, Balgach, Switzerland) (84). To create AnxA5-KO in EA.hy926 cells, we performed co-transfection using a 1:1 ratio of pcDNA3.3-Cas9-2A-eGFP and pGS-U6-gAnxA5 (84). The following day, GFP-positive cells were sorted, and then 200-800 cells were individually seeded into 10 cm dishes. Subsequently, 24 clones were selected and cultured further (84). These clones underwent analysis through PCR and Western blot.

WT and AnxA5-KO PCs were obtained from mice using methods described elsewhere (99).

2.3 AnxA5 silencing was achieved through Short Hairpin RNA (shRNA) technology

HeLa cells were cultured in 6-well plates under standard conditions and grown to a confluency of 30%. Next, cells were transfected with 10 µL of shRNA plasmid DNA, where Control shRNA Plasmid-A (sc-108060) was used for control cells, and AnxA5 shRNA Plasmid (sc-29686-SH) was utilized for AnxA5 knockdown cells (84). All plasmids were procured from Santa Cruz Biotechnology. Following a 48-hour period post-transfection, the transfection medium was substituted with fresh medium containing 1.0 µg/ml of puromycin (84). After 48 hours, approximately 90% of the cells had undergone cell death, and the selective medium was refreshed every two days (84). Colonies were individually collected using a pipette filled with trypsin and further cultured under selective conditions in separate plates (84).

2.3 Quantitative PCR

To obtain total RNA, we employed the RNeasy® Mini Kit (Qiagen, Hilden, Germany), and subsequently performed reverse transcription using the Applied Biosystems High-Capacity cDNA Reverse Transcription kit (Thermo Fisher Scientific Baltics UAB, Vilnus, Lithuania) (10). Quantitative PCR (qPCR) was conducted by employing the Promega GOTaq® qPCR Master Mix (Madison, WI, USA) (10). The efficacy of rMCU knockdown was assessed using specific primers for rMCU (Forward: GCGTTGCCATCTATTCCCCA; Reverse: TGGCTCAGGAGGTCTCTCTTT) and subsequently normalized to rGAPDH (Forward: TCTACATGTTCCAGTATGACTC; Reverse: GCATCACCCCATTTGATG) (10).

2.4 Buffers and Solutions

Before conducting microscopic measurements, cells were equilibrated to room temperature in a storage buffer containing the following components: 2 mM Ca2+, 138 mM NaCl, 1 mM MgCl2, 5 mM KCl, 10 mM HEPES, 2.6 mM NaHCO3, 0.44 mM KH2PO4, amino acid, and vitamins mix, 10 mM glucose, 2 mM L-glutamine, 1% penicillin/streptomycin, 1.25 µg/mL amphotericin B, and pH adjusted to 7.4 (84). Live-cell imaging experiments were conducted using three different buffers: Hepes-buffered Ca2+-containing experimental buffer (2CaNa): Comprising 2 mM CaCl2, 138 mM NaCl, 1 mM MgCl2, 5 mM KCl, 10 mM Hepes, and 10 mM D-glucose at pH 7.4. A nominal Ca2+-free solution (0CaNa): Containing 0.1 mM EGTA in place of CaCl2. 2Ca30K buffer: Comprising 2 mM CaCl2, 113 mM NaCl, 1 mM MgCl2, 30 mM KCl, 10 mM Hepes, 10 mM D-glucose, and pH adjusted to 7.4 (84)(9). Cells were exposed to stimulation with either 100 µM ATP, histamine, or BHQ (15 µM) in either the 2CaNa or 0CaNa buffer (84). In experiments where glucose deprivation was applied, we used a glucose-free buffer consisting of the following components: 2 mM CaCl2, 138 mM NaCl, 1 mM MgCl2, 5 mM KCl, and 10 mM Hepes at a pH of 7.4 (9). SKF10047 and BD1047 were obtained from Tocris (Tocris, Abingdon, UK) and were dissolved in water to prepare 10 mM stock solutions (9).

2.5 Live-Cell Imaging Experiments

The experiments were carried out utilizing an Olympus IX73 inverted microscope, which was equipped with a UApoN340 40× oil immersion objective (Olympus, Tokyo, Japan), and a CCD Retiga R1 camera (Q-imaging, Surrey, BC, Canada) (84). The illumination was supplied using LedHUB® from Omnicron (Germany), which featured 340, 385, 455, 470, and 550 nm LEDs, combined with a CFP/YFP/RFP (CFP/YFP/mCherry-3X, Semrock, New York, NY, USA) filter

set (84). Data acquisition was carried out using VisiView 4.2.01 (Visitron, Puchheim, Germany). For live-cell imaging experiments, cells were positioned within a flow chamber (84). During measurements, a gravity-driven perfusion system, PS-9D (NGFI, Graz, Austria), was employed to deliver a continuous flow to the cells (84). The valve, equipped with nine positions, was linked to reservoirs, and the relevant reservoir was automatically activated using perfusion control software (84). Cell selection was randomized based on the expression of genetically encoded biosensors (84).

In the case of NFATc3 translocation experiments, we used a Zeiss array confocal laser scanning microscope (Axio Observer.Z1 by Zeiss, Gottingen, Germany) equipped with a 100x objective lens (Plan-Fluor x100/1.45 Oil, Zeiss, Germany) (10). This microscope setup included a motorized filter wheel (CSUX1FW, Yokogawa Electric Corporation, Tokyo, Japan) on the emission side, an AOTF-based laser merging module for the 405, 445, 473, 488, 514, and 561 nm laser lines (Visitron Systems), and a Nipkow-based confocal scanning unit (CSU-X1, Yokogawa Electric Corporation) (10). Data acquisition and control of the fluorescence microscope were managed using Visiview 4.2.01 (Visitron, Puchheim, Germany) (10).

2.6 Detection of Sub-Mitochondrial Ca^{2+} levels

To measure mitochondrial matrix Ca^{2+} levels, we employed a genetically encoded, FRET-based sensor, 4mtD3cpv23, specifically targeted to the mitochondrial matrix (96)(84). We conducted measurements of mitochondrial IMS Ca^{2+} levels using a genetically encoded, ratiometric green-emitting IMS-targeted Ca^{2+} sensor known as IMS-GEM-GECO1 (98)(84). The measurement of mitochondrial cristae was carried out using a genetically encoded, ratiometric cristae-targeted Ca2+ sensor called ROMO-GEM-GECO1 (98)(84). FRET measurements in real-time between MICU1-CFP and MICU1-YFP were conducted using the MICU1 FRET sensor (38). The 4mtD3cpv sensor was subjected to illumination with a 455 nm LED every 2 to 3 seconds, employing a 300-millisecond exposure time (84). Emission signals were collected at wavelengths of 480 nm and 530 nm, employing a CFP/YFP/mCherry-3X filter set and a 505dcxr beam-splitter (84). The IMS-GEM-GECO1 and ROMO-GEM-GECO1 sensors underwent illumination with a 425 nm LED every 2 to 3 seconds, employing a 200-millisecond exposure time (84). Emission signals were gathered at 480 nm and 530 nm using a CFP/YFP filter set and a 505dcxr beam-splitter. All recorded data were subjected to background subtraction and corrected for photobleaching using an extrapolation method based on an exponential decay fit of the initial basal phase (84).

2.7 Detection of Cytosolic Ca^{2+} levels

Cytosolic Ca^{2+} levels were monitored using the genetically encoded cytosol-targeted intensiometric calcium sensor jGCaMP7s (100). Alternatively, ratiometric measurements of cytosolic Ca^{2+} were conducted using the dye Fura-2 acetoxy-methyl-ester (Fura-2 AM) (TEFLabs, Austin, TX) (84). To measure cytosolic calcium levels with Fura-2 AM, cells were incubated with 3.3 μM of the dye (at 60% confluency for HeLa and 80% confluency for PCs and EA.hy926 cells) in the storage buffer for a period of 30 minutes (84). Following the incubation, cells underwent two washes with a storage buffer, and subsequent measurements were carried out in either 2CaNa or 0CaNa buffer. All recorded data were subjected to background subtraction (84).

The jGCaMP7c sensor was exposed to 470 nm LED illumination every 2 seconds, with a 200-millisecond exposure time and emission was obtained at 510 (84). In the case of Fura-2 AM measurements, cells were subjected to sequential illumination with 340 nm and 385 nm LEDs every 2-3 seconds, employing a 300-millisecond exposure time, and emission signals were collected at 510 nm (84). Background subtraction was applied to all recorded data (84).

2.8 Detection of ER Ca^{2+} levels

The measurement of ER Ca^{2+} levels was conducted using the genetically encoded, FRET-based, ER-targeted ratiometric Ca^{2+} sensor known as D1ER (97). The sensor was exposed to illumination with a 455 nm LED every 3 seconds, with a 300-millisecond exposure time (84). Emission signals were gathered at 480 nm and 530 nm using a CFP/YFP/mCherry-3X filter set and a 505dcxr beam-splitter (84). To enhance the accuracy of the data, background subtraction and correction for photobleaching was performed by extrapolating an exponential decay fit of the initial basal phase in all recordings (84).

2.9 Detection of mitochondrial ATP levels

We assessed mitochondrial ATP levels using the genetically encoded FRET-based mitochondrial matrix-targeted ATP sensor, mt.AT1.03 (9), kindly provided by Hiromi Imamura at Kyoto University, Kyodai Graduate School of Biostudies in Japan. Mt.AT1.03 consists of the ε subunit of the bacterial FoF1-ATP synthase positioned between cyan and yellow fluorescent proteins (FP) (9). When ATP binds to the ε subunit of the bacterial FoF1-ATP synthase, it undergoes a conformational change that alters the distance between the cyan and yellow

fluorescent proteins (9). This change impacts the emission of the FRET pair, resulting in a ratiometric readout of mitochondrial ATP fluctuations (9). We excited this sensor using a 455 nm LED with a 300-millisecond exposure time every 2 seconds and collected emissions at 480 nm and 530 nm using a CFP/YFP/mCherry-3X filter set along with a 505dcxr beam-splitter (9). The background-subtracted emission ratio of 530/480 was then analyzed (9). Following a 10-minute cell adjustment in the loading buffer, cells were exposed to an experimental buffer to measure basal mitochondrial ATP levels for 2 minutes (9). To assess the mitochondrial ATP response during glucose deprivation and oligomycin treatment, we changed the buffer to one lacking glucose for 8 minutes (9). At the conclusion of this 8-minute period, cells were perfused for 4 minutes with a glucose-containing buffer and an additional 6 minutes with 2 µM oligomycin (9). The Oxphos/Glycolysis ratio was determined by calculating the ratio change after oligomycin addition and dividing it by the change in ratio observed during glucose deprivation (9).

2.10 Cytosolic pyruvate to lactate ratio measurements

We quantified the cytosolic pyruvate-to-lactate ratio using a genetically encoded, FRET-based sensor targeted to the cytosol, known as Lapronic (AddGene, #140756) (9). We excited this sensor using a 455 nm LED every 2 seconds with a 300-millisecond exposure time, and emissions were collected at 480 nm and 530 nm employing a CFP/YFP/mCherry-3X filter set along with a 505dcxr beam-splitter (9). We subsequently analyzed the background-subtracted emission ratio of 530/480 (9).

2.11 Measuring ROS in mitochondria and the cytosol

We conducted measurements of ROS in both mitochondria and the cytosol using recently developed genetically encoded H_2O_2 sensors known as mitoHyper7 and cytoHyper, which are targeted to the mitochondrial matrix and cytosol, respectively (10). Both sensors were subjected to excitation by 405 nm and 488 nm laser lines, while emissions were recorded at 510 nm (10). To establish the baseline, cells were exposed to 5 mW of 405 nm and 488 nm laser light every 5 seconds, with a 500-millisecond exposure, over 2 minutes (10). Starting from the end of minute 2, the excitation intensity of the 405 nm and 488 nm lasers was elevated to 20 milliwatts, and measurements were carried out for an additional 22 minutes under these conditions (10). After minute 22, cells were stimulated with 200 µM of H_2O_2 to determine the saturation ratio of the sensors (10). Control cells, where ROS production did not occur, were subjected to excitation with 5 mW of 405 nm and 488 nm laser light every 5 seconds, with a

500-millisecond exposure, over a 22-minute duration (10). The maximum UV light-induced H_2O_2 ratio of 488/405, after background subtraction, was then subtracted from the baseline to ascertain the change in ROS production at the end of 20 minutes with repetitive UV induction at 20 mW (10).

2.12 Experiments involving the translocation of GFP-NFATc3 and Ca^{2+} dynamics under UV light stimulation.

Experiments involving the translocation of GFP-NFATc3 were conducted using the GFP-NFATc3 construct, which was graciously provided by Mark L. Dell'Acqua from the Department of Pharmacology at the University of Colorado School of Medicine in Aurora (10). Unless specified otherwise, all GFP-NFATc3 translocation experiments adhered to the following imaging parameters: GFP-NFATc3 was excited with laser lines at 488 nm (30 mW) every 5 seconds, with each exposure lasting 500 milliseconds, and emissions were captured at 510 nm (10). For experiments involving UV light stimulation and concurrent monitoring of changes in cytoplasmic calcium concentration ($[Ca^{2+}]$cyto), cells were loaded with 3.3 µM Fura-2 in EB for a duration of 30 minutes (10). Subsequently, they were excited with laser lines at 405 nm (20 mW) every 5 seconds, employing a 500-millisecond exposure time, and emissions were recorded at 510 nm using a charged CCD camera (CoolSNAP-HQ, Photometrics, Tucson, AZ, USA) (10). Data acquisition for both $[Ca^{2+}]$cyto and the translocation of GFP-NFATc3 from the cytosol to the nucleus was facilitated through the VisiView acquisition software (Universal Imaging, Visitron Systems) (10). The measurement was based on the background-subtracted GFP-NFATc3 fluorescence ratio between the nucleus and cytosol region (10). The baseline ratio of GFP-NFATc3 at minute 0 represented the resting state, while the maximum translocation ratio within the 0 to 10-minute timeframe was observed at minute 10 (10). Furthermore, minute 25 denoted the peak translocation ratio of GFP-NFATc3 within the 20 to 25-minute timeframe (10).

To investigate biphasic GFP-NFATc3 translocation, cells loaded with Fura-2-AM were stimulated with 100 µM CCh in the presence of 2 mM extracellular Ca^{2+} (10). The concurrent changes in $[Ca^{2+}]$cyto and GFP-NFATc3 translocation were recorded, with quantification of cytosolic calcium oscillation occurring between minutes 10 and 25 (10). To inhibit Ca^{2+} oscillation in the cytosol and GFP-NFATc3 translocation, cells were perfused with a mixture containing 2 µM oligomycin (Sigma-Aldrich, Vienna, Austria) and 10 µM verapamil (Sigma-Aldrich, Vienna, Austria) during the experiment, or they underwent a 30-minute preincubation

with 1 mM NAC (Sigma-Aldrich, Vienna, Austria) (10). The count of cytosolic Ca^{2+} oscillations was determined between minutes 2 and 24 (10).

2.13 Quantification of Cytosolic Ca^{2+} Oscillation

We conducted background correction on the cytosolic Ca^{2+} traces using background ROI intensities (10). Additionally, we computed the standard deviation of the baseline Ca^{2+} signals to assess the signal-to-noise ratio (10). Initially, we identified peaks by detecting a shift from a positive to a negative slope between measurement points (10). As a secondary criterion, changes in intensity between time points corresponding to transitions from positive to negative slopes and vice versa needed to exhibit values at least 5 times higher than the baseline standard deviation values to qualify as valid signals and be designated as Ca^{2+} oscillations (10).

2.14 Measurements of Mitochondrial Membrane Potential

Experiments on mitochondrial membrane potential were conducted following established protocols as described previously (9). In brief, mitochondrial membrane potential experiments utilized the Tetramethylrhodamine methyl ester perchlorate (TMRM) dye obtained from Invitrogen™ (T668; Vienna, Austria) (84). TMRM dye was subjected to excitation using a 550 nm LED every 3 seconds, employing a 200-millisecond exposure time. Emission signals were collected at 600 nm utilizing the CFP/YFP/mCherry-3X filter set (84). Cells were exposed to a storage buffer containing 25 nM of TMRM dye at room temperature for 30 minutes (84). This was done when the cells were at 50-60% confluence (84). Following the incubation period, cells were perfused with 2CaNa for 2 minutes, during which basal values were recorded (84). Subsequently, the cells were subjected to a 4-minute perfusion with 2CaNa buffer that included 1 µM of carbonyl cyanide-p-trifluoromethoxyphenylhydrazone (FCCP) obtained from Abcam, Cambridge, UK (84). This step was conducted to induce full depolarization of the mitochondria. The fluorescence ratio, corrected for background, between mitochondria and the nucleus was employed to calculate the basal mitochondrial membrane potential in both WT and AnxA5-KO cells (84).

2.15 ER-Mitochondria Co-Localization and 3D-Morphological Analysis of Mitochondria

To mark the endoplasmic reticulum, WT, and AnxA5-KO HeLa cells were subjected to transfection with ERAT4.03 NA (NGFI, Graz, Austria) (84). Simultaneously, mitochondria were stained using Mitotracker Red CMXROS (MTR-CMX) from Invitrogen, Thermo Fischer Scientific, Vienna, Austria. Cell imaging was carried out using a confocal spinning disk microscope (Axio Observer.Z1 from Zeiss, Gottingen, Germany) (84). The microscope features a 100x objective (Plan-Fluor x100/1.45 Oil, Zeiss), a motorized filter wheel (CSUX1FW, Yokogawa Electric Corporation, Tokyo, Japan), and an AOTF-based laser merge module offering laser lines at 405, 445, 473, 488, 514, and 561 nm (Visitron Systems) (84). ERAT4.03 NA and MTR-CMX were excited sequentially with 488 and 561 nm, and emission signals were collected at 530 nm and 600 nm, respectively, using a charged CCD camera (CoolSNAP-HQ, Photometrics, Tucson, AZ, USA) (84). Z-stacks with 0.2 µm z-height increments were imaged. The data from the imaging process was captured using VisiView software (Universal Imaging, Visitron Systems) (84). The images underwent blind deconvolution (NIS-Elements, Nikon, Vienna), and the co-localization analysis between ER (ERAT4.03 NA) and mitochondria (MTR-CMX) was conducted at the individual cell level utilizing ImageJ and the coloc2 plugin (84). The calculation of Pearson's coefficient follows established procedures as described in prior studies (73).

To conduct a morphological analysis of mitochondria, we employed a customized ImageJ macro, the details of which can be found in a our previous publication (39). In short, following the process of deconvolution, we implemented the rolling ball method to perform background subtraction, thereby enhancing the overall contrast (84). A global auto Otsu threshold (utilizing a stacked histogram) and a localized Otsu threshold (with a 640 nm radius and a histogram based on a single slice) were employed on the stack, followed by their combination (84). The segmentation and binarization of mitochondria were carried out using the ImageJ plugin known as 3D manager (84). The determination of mitochondrial volume and surface was accomplished using the 3D Geometrical Measure plugin, while the parameters for elongation and flatness were obtained through the application of the 3D Ellipsoid Fitting plugin (84). Quantifying mitochondrial branching involved calculating the ratio of mitochondrial volume to the volume of the 3D ellipse fitted to the corresponding mitochondrion (84).

2.16 Morphological analysis of mitochondria imaged with SIM

We co-transfected cells with MICU1-YFP and MCU-mCherry constructs. Subsequently, single 3D-SIM imaging and time-lapsed capture of MCU-mCherry were performed both before and after the release of ER Ca^{2+} via the application of 100 μM of Histamine (84). Subsequently, these images were employed to conduct a morphological analysis of mitochondria, following well-established protocols (39). In summary, we briefly employed the ImageJ Plugin (specifically the Mosaic Suite and NIH background subtractor) to correct for background in the images (84). Subsequently, binarization was achieved using an automated Yen thresholding method (84). The count of mitochondria, along with their respective areas, minor axes, and major axes, was determined using the ImageJ particle analyzer (84). The aspect ratio was calculated by utilizing the ratio between the major and minor axes of the mitochondria (84).

2.17 Cristae Membrane Kinetics Quantification

The quantification of CM-kinetics within both entire mitochondria and the MAM region was performed following methods detailed elsewhere (41,42). In brief, HeLa cells of both WT and AnxA5-KO types were subjected to transfection with ER-RFP and stained using Mitotracker Green/FM (MTG) (84). Subsequently, live dual-color SIM imaging was conducted to capture the recordings (84). Quantification of CM-membrane kinetics involved the utilization of both local and global automated thresholding techniques on the MTG staining (84). This evaluation was conducted both before and following the release of ER Ca^{2+}, which was triggered by stimulating the cells with 100 μM of histamine (84). The assessment entailed the measurement of alterations in the cristae membrane per frame within the mitochondria (84). To identify CM-kinetics within MAM regions, a mask was generated by partially dilating the overlapped area between ER-RFP and MTG staining (84).

2.18 Evaluation of MCU shuttling to IBM

The assessment of MCU translocation to the inner boundary membrane was conducted in both WT and AnxA5-KO (HeLa) cells using methods previously outlined (39). In summary, cells underwent co-transfection with MICU1-YFP and MCU-mCherry constructs. Subsequently, imaging was conducted both before and 90 seconds following the release of ER Ca^{2+} (84). Two masks were employed to measure the fluorescence intensities of MCU-mCherry in both the cristae membrane and the inner boundary membrane (84). The IBM association index was determined by calculating the intensity ratio between the IBM and the cristae membrane. A

greater value for the IBM association index indicates a more pronounced shift in the distribution of MCU towards IBM (84). The image analysis was performed using the freely available software tool, ImageJ.

2.19 Electron microscopy

To achieve chemical fixation, cells from both the WT and AnxA5-KO (HeLa) groups were initially cultured on Aclar fluoropolymer foils and then treated with a solution comprising 2% paraformaldehyde and 2.5% glutaraldehyde in a buffered environment. Following osmification, the cells underwent a dehydration process using a series of ethanol solutions, ranging from 50% to 100% (84). Subsequently, a transition solvent, propylene oxide, was applied and allowed to incubate for 30 minutes (84). This was followed by successive incubations in a mixture of propylene oxide and TAAB embedding resin (TAAB, Berkshire, UK) at ratios of 1:1 and 1:2. Lastly, the samples were subjected to incubation in pure resin and subsequently polymerized at 60°C for a duration of three days, following previously documented procedures (101).

High-pressure freezing and freeze substitution were carried out in accordance with previously established protocols (102). Briefly, HeLa cells were seeded onto sapphire discs, encompassing both untreated WT cells and cells subjected to a 20-second histamine stimulation (84). The cells on the sapphire discs were subsequently inserted into aluminum carriers and subjected to high-pressure freezing using the Leica HPM 100 high-pressure freezer (84). The initial step of freeze substitution involved immersing the specimen in acetone for a total duration of 44 hours, maintaining a temperature of -90 °C (84). During this period, there was a single replacement of acetone after 24 hours (84). Subsequently, the next step involved immersing the specimen in a solution comprising acetone along with 0.5% glutaraldehyde and 1.5% distilled water (84). This process lasted for 6 hours, during which the temperature was incrementally elevated to -60 °C. Following this, the specimen was left to incubate for 8 hours at -60 °C in the same substitution solution (84). The temperature was then gradually increased to -40 °C over the course of the next 4 hours, followed by a 2-hour incubation at -40 °C (84). The final phase of freeze substitution involved immersing the specimen in pure acetone. During this stage, the temperature was gradually elevated from -40 °C to 0 °C over 3.3 hours, and it was maintained at 0 °C for 30 minutes (84). To remove any remaining acetone, the substituted samples underwent four cycles of rinsing in ice-cold 96% ethanol (84). The infiltration of resin was conducted on ice, with a sequential mixture of 96% ethanol to LR White resin, first at a ratio of 2:1, and then at a ratio of 1:2. Each of these steps

had a duration of 30 minutes (84). The specimens were placed in pure LR White resin at 4 °C overnight, followed by a three-day polymerization process under UV light at the same temperature of 4 °C (84).

For the immunogold labeling procedure, thin sections were prepared from the freeze-substituted cells embedded in LR White resin and were then positioned on nickel grids coated with pioloform (84). Following a 30-minute blocking step with 5% normal goat serum, the sections were subjected to a two-hour incubation period at room temperature using a 1:100 dilution of the Anti-Annexin V antibody (Abcam ab14196) (84). Subsequently, a one-hour incubation with 10 nm gold-conjugated goat anti-rabbit IgG (BB International EM) was carried out (84). The sections underwent thorough washing between each incubation phase (84). In a negative control experiment, where the primary antibody was intentionally omitted, no staining was observed. Electron micrographs were captured using a Thermo Fisher FEI Tecnai G2 20 microscope equipped with an Ametek Gatan US1000 camera. Whole cells were observed at a magnification of 5000x (84).

2.20 Analysis of Cristae Membrane, Density, and Cristae Density Distribution

The evaluation of cristae membrane density was conducted following previously established methods (42). Briefly, mitochondria were manually chosen through free-hand selection. Following the previous step, cristae were delineated within the chosen mitochondria using a free-hand segmentation approach (84). Measurements were taken for the area and perimeter of both mitochondria and cristae (84). The relationship between the cristae's perimeter and the mitochondria's area provides an indicator of the cristae density within individual mitochondria. The relationship between the perimeter of cristae and the perimeter of mitochondria signifies the ratio of cristae to mitochondria membrane content (84). Cristae density distribution was analyzed as described in our previous publication (42). Briefly, mitochondrial segments were transformed into binary masks and subsequently employed as masks on binarized cristae membranes. This allowed for the computation of the proportion of cristae perimeter contained within the mitochondrial area (84). The mitochondrial mask was systematically diminished in 2-pixel increments, equivalent to 5.88 nanometers each, while concurrently assessing the associated coverage of cristae (84). These measurements yielded cristae density values within circular segments, commencing from the outer mitochondrial membrane and extending towards the center of the mitochondria. To accommodate variations in mitochondrial size and

shape, which led to varying numbers of ring segments, the cristae densities were normalized by utilizing linear interpolation to standardize them to 100 segments (84).

2.21 Analysis of the Immunogold Staining

Electron micrographs, which had been subjected to immunolabeling for AnxA5, were manually divided into segments to create masks delineating the regions corresponding to cytosol, nucleus, and mitochondria (84). Additionally, the cell underwent scrutiny to identify gold particles, and the x/y-localizations of these particles were recorded for subsequent analysis (84). Gold granules were identified based on their dimensions, spherical shape, and the electron-lucent halo that appeared under focus conditions (84). A specially designed macro was employed to ascertain the precise localization of gold particles within the cellular compartments, namely, the cytosol, nucleus, and mitochondria (84). Furthermore, the proximity of each gold particle located in the cytosol or mitochondria to the outer mitochondrial membrane was quantified by measuring the shortest distance (84).

2.22 Proximity Ligation Assay

Proximity ligation assay (PLA) was performed as described in the previous publication (103). In brief, cells from both the WT and AnxA5-KO groups were cultured in 12-well plates (84). Subsequently, the cells were transfected with either negative control siRNA (neg. siRNA) or siVDAC1 (84). Approximately 48 hours following the transfection, the cells were subjected to a wash with 1% PBS and then fixed with a 10% formaldehyde solution for 10 minutes at room temperature (84). The reaction was subsequently halted using a 1 M glycine solution (pH 2.2) and the cells were further incubated in 100 mM glycine for 15 minutes (84). Following this, the cells underwent a PBS wash and were subsequently permeabilized for a duration of 15 minutes using 0.1% Triton-X100 (84). They were then washed twice with PBS. To facilitate blocking, 50 µL of a blocking solution (Duolink In Situ PLA Probe, Sigma-Aldrich) was introduced into each well, and the plate was subjected to a 30-minute incubation at 37 °C within a humidified incubator (84). Following the incubation period, the blocking solution was aspirated from each well (84). Subsequently, primary antibodies specific for Annexin 5 (Abcam, ab14196, 1:200) and VDAC1 (Abcam, 186321, 1:400) were diluted in PBS, introduced into each well, and allowed to incubate overnight at 4 °C (84). The following day, the cells underwent two consecutive washes with Tris Buffered Saline containing 0.01% Tween (TBS-T). Subsequently, diluted proximity ligation assay probes (Duolink In Situ PLA Probe, Sigma Aldrich) at a ratio of 1:5 were introduced into each well and subjected to an incubation period

of one hour at 37 °C within a humidified incubator (84). Following the incubation, the cells were subjected to two washes with TBS-T (84). For the ligation step, an in situ detection reagent (Texas Red kit, Bio-Synthesis (Zotal)) was introduced into the wells and allowed to incubate for 30 minutes at 37 °C, after which the cells were washed two more times with TBS-T (84). Following this, an amplification solution included in the KIT was introduced to each specimen (84). Subsequently, the plate underwent incubation within a humidity chamber for a duration of 100 minutes at a temperature of 37°C (84). Following this incubation period, coverslips were subjected to a washing process and were then affixed to slides using a mounting medium containing DAPI (Immuno bioscience, AR-6500-01) (84). Confocal microscopy (Olympus 1X81) was used to capture images of the slides approximately 2 hours post-mounting. To quantify individual PLA signals, an image analysis macro developed in Image-J Fiji was employed (84). A specific threshold was established to identify positive PLA dots among the signals detected (84). Signals surpassing this predetermined threshold were categorized as positive PLA dots. Cell counts were determined based on the DAPI-containing cells (84). The PLA dot-to-cell ratio served as the measurement. Ultimately, these ratios were standardized with respect to WT cells (84).

2.23 Western Blot

To assess the expression levels of proteins responsible for mitochondrial Ca^{2+} uptake, HeLa cells and AnxA5-KO cells were plated in 6-well dishes (84). Subsequently, the cells were collected using RIPA buffer (comprising 25 mM Tris-HCl at pH 7.6, 150 mM NaCl, 5 mM EDTA, 1% Triton X-100, 1% sodium deoxycholate, and 0.1% SDS), which was supplemented with a protease inhibitor cocktail (Sigma, Vienna, Austria, Catalog #P8340) (84). The protein concentration in the extracted samples was quantified using the Pierce™ BCA Protein Assay Kit from ThermoFisher Scientific (Waltham, MA, USA) and measured on a CLARIOstar Plus instrument (BMG Labtech, Ortenberg, Germany) (84). The samples were separated through SDS-PAGE (Sodium Dodecyl Sulfate-Polyacrylamide Gel Electrophoresis) and subsequently transferred onto a membrane (84). Following this, the membranes were subjected to overnight incubation at 4°C with primary antibodies, including Annexin 5 (Santa Cruz, sc-74438, 1:1000), VDAC1 (Abcam, 186321, 1:5000), MICU1 (Cell Signaling Technology, D4P8Q, 1:1000), UCP2 (Cell Signaling Technology, D105V, 1:1000), MCU (Cell Signaling Technology, D2Z3B, 1:1000), β-Actin (Sigma, A5316, 1:1000), and Histone H3 (Cell Signaling Technology, 1B1B2, 1:1000) (84). On the subsequent day, the membranes underwent incubation with the relevant HRP-conjugated secondary antibodies for a duration of 1 hour at room temperature (84). After

rinsing, the membranes were subjected to incubation with the SuperSignalTM West Pico PLUS Chemiluminescent Substrate (ThermoFisher Scientific) (84). Subsequently, the signal was captured utilizing the ChemiDoc MP Imaging System (Biorad) (84). To determine signal intensities, Image-J Fiji66 was employed, and normalization was performed with respect to the intensities of the relevant β-actin or Histone H3 signals, serving as loading controls (84).

In the cell fractionation assay, the concentrations of cytosolic, crude mitochondria, and pure mitochondria fractions were assessed using the Lowry method (84). Immunoblotting utilized the following primary antibodies: Annexin 5 (Abcam, ab14196, 1:1000), VDAC1 (Abcam, 186321, 1:5000), Cytochrome C (Biosciences, BD556432, 1:1000), Hexokinase-1 (Santa Cruz, sc6517, 1:1000), Lactate dehydrogenase (Santa Cruz, sc27230, 1:1000), and Tubulin (BioLegend, 801202, 1:5000) (84). Corresponding HRP-conjugated secondary antibodies were employed as well (84).

To validate the knockdown of VDAC1, HeLa cells were initially plated in 6-well dishes (84). Subsequently, the cells were transfected with specific siRNAs, either negative control siRNA or siVDAC1 (84). Harvesting of cells was carried out 48 hours post-transfection. Immunoblotting was performed using antibodies targeting VDAC1 and β-actin, along with the relevant HRP-conjugated secondary antibodies (84).

The following antibodies are used in (Oflaz & Koshenov et al. 2022): SIGMAR1 (D4J2E) Rabbit mAb #61994 (Cell Signaling); β-Actin (D6A8) Rabbit mAb #8457 (Cell Signaling); goat anti-rabbit IgG-HRP: sc-2054 (Santa Cruz Biotechnology, Dallas, TX, USA); Color Prestained Protein Standard, Broad Range (10–250 kDa) (P7719S, New England BioLabs, Waltham, MA, USA) (9).

2.24 Co-Immunoprecipitation

Co-immunoprecipitation was used in accordance with the previously outlined methodology(39). Briefly, AnxA5 knockout Hela cells were transfected with either an empty plasmid (pcDNA3.1 (-)) or an AnxA5-Flag plasmid 48 hours prior to the experiment.. Subsequently, cell lysis was carried out using 0.7 mL of lysis buffer containing the following components: 100 mM NaCl, 20 mM Tris, 1 mM EGTA, 5 mM n-Dodecyl β-D-maltoside, pH 7.5-HCl, along with protease inhibitors, which included 10 µM phenylmethylsulfonyl fluoride, and 1 µg/ml each of aprotinin, leupeptin, and pepstatin (84). Following a brief freeze-thaw cycle, the lysates underwent centrifugation at 12,000g for 10 minutes. Subsequently, 60 µl of the supernatants were extracted for protein quantification employing a BCA assay (Thermo-Fisher) and for analysis

as total cell lysates (input) (84). The remaining lysates, comprising approximately 1.5 mg of total protein, were subjected to incubation with 30 µl of anti-Flag M2 affinity gel (Sigma-Aldrich) for 30 minutes on a rotary shaker, following the manufacturer's recommended bead preparation procedure (84). Subsequently, the beads were gathered through centrifugation at 8,000g for 30 seconds and subjected to three successive washes with TBS (84). Every step was conducted at 4°C (84). To elute the FLAG-fusion proteins, a solution consisting of 50 µl of 2x Lämmli sample buffer along with 5% β-mercaptoethanol, and subsequently, the protein samples were subjected to a 10-minute boiling step before being subjected to SDS-PAGE (84). For cross-linking fixation, cells underwent a series of steps: first, they were washed with PBS, followed by incubation with 10% formaldehyde for 10 minutes at room temperature with agitation. The reaction was halted using 1 M glycine (pH 8), after which the cells were once again washed with PBS (84). Subsequently, 100 mM glycine was introduced and incubated for 15 minutes at room temperature with agitation (84). The cells were then readied for Co-IP following the previously described procedure (84).

Regarding the immunoblotting procedure, whole cell lysates, consisting of 40 µg for VDAC1 and 20 µg for Annexin V in terms of total protein, as well as Co-IP samples, were all subjected to SDS-PAGE (84). Following this, PVDF membranes underwent overnight incubation at 4°C with primary antibodies, specifically anti-VDAC1 (Abcam, 186321, diluted at 1:1000) and Annexin 5 (Abcam, ab14196, diluted at 1:1000) (84). To prevent any potential interference stemming from denatured heavy and light chain IgG, the immunoblot reagent Veriblot (Abcam, diluted at 1:1000, ab131366) conjugated with HRP was employed for the detection of co-immunoprecipitated proteins (84). Immunoreactive bands were observed by applying Immobilon Western HRP Substrate (Thermo Fisher) and utilizing the chemiluminescence detection system known as ChemiDoc (Bio-Rad) (84).

2.25 Chemical cross-linking

Cross-linking experiments were done as described in previous publications(104). In summary, cells at a concentration of 1.5 mg/ml were collected and exposed to 300 µM of the cross-linking reagent, ethylene glycol bis(succinimidyl succinate) (Thermo Fisher, 21565), in PBS with a pH of 8.3, for 20 minutes at 30°C (84). The samples, containing 30 µg of protein each, were subjected to SDS-PAGE and subsequently underwent immunoblotting with a mouse anti-VDAC1 antibody (Abcam, 186321, diluted at 1:5000) (84). The quantitative assessment of the VDAC1 dimer level was determined using Image-J Fiji(105) (84).

2.26 Cisplatin and VBIT-4 Treatment

WT and AnxA5-KO HeLa cells were exposed to either 5 or 10 µM of cisplatin (Sigma, P4394), or subjected to co-treatment with 10 µM cisplatin in combination with 20 µM VBIT-4 (VBIT-4 was graciously provided by Prof. Dr. Varda Shoshan-Barmatz from Ben-Gurion University of the Negev, Beer-Sheva, Israel) (84). In the case of co-treatment, cells were initially pre-incubated with VBIT-4 for 2 hours before being subsequently exposed to cisplatin and VBIT-4 (84).

2.27 VDAC1 cluster size experiments and analysis

Cells that expressed VDAC1 with a tetracysteine tag (VDAC1-TC) were labeled with 1 µM FlAsH-EDT2 (Cayman Chemical, Michigan, USA) in EHL for 15 minutes at 37°C (84). Following the initial staining, the cells were washed with 100 µM BAL (2,3-dimercaptopropanol or British anti-Lewisite) in EHL for 15 minutes at 37°C, after which they were maintained in EHL until the confocal imaging was performed (84).

High-resolution imaging was carried out using an array confocal laser scanning microscope (Axiovert 200 M, Zeiss) equipped with a 100×/1.45 NA oil immersion objective (Plan-Fluor, Zeiss) and a Nipkow-based confocal scanner unit (CSU-X1, Yokogawa Electric Corporation, Tokyo, Japan) (84). Diode lasers from Visitron Systems were utilized as the excitation light source. Specifically, VDAC1-TC was excited at 488 nm, while mitoDsRed was excited at 561 nm. Emissions were captured using a CoolSNAP HQ2 CCD Camera (Photometrics, Tucson, Arizona, USA) and the following emission filters (Chroma Technology Corporation, VT, USA) were employed: ET535/30 m for VDAC1-TC and ET630/75 m for mitoDsRed (84).

The assessment of VDAC1 cluster size was performed using the Fiji software (84). To improve cluster visibility, a Gaussian blur preprocessing method was applied. Subsequently, the Watershed technique was employed to separate clusters that were closely positioned, and this was followed by the utilization of the MaxEntropy thresholding method to accurately identify the clusters (84).

2.28 Flow Cytometry

Following either 24 or 48 hours of treatment with cisplatin, VBIT4, or their combination, cells and cell supernatant were collected and subjected to staining using the FITC Annexin V Apoptosis Detection Kit 1 (BD Biosciences) as per the manufacturer's guidelines (84). Flow

cytometry analyses were conducted using a CytoFLEX S flow cytometer from Beckman Coulter Life Sciences, and the resulting data were processed and analyzed with the CytExpert Software also from Beckman Coulter (84).

2.29 Mitochondria Isolation

In preparation for patch clamp experiments, crude mitochondria were isolated through a series of differential centrifugation steps, as outlined in prior protocols (106). In summary, one to two days prior to the isolation process, both WT and AnxA5-KO cells were seeded onto a 20 cm dish. On the day of isolation, when the cells reached 90-100% confluence, they were trypsinized, collected, and then rinsed with PBS. The cell pellet was resuspended in 1 ml of IMBc(+PI) buffer and subjected to homogenization using a glass-Teflon potter with 80 strokes (84). The suspension was transferred into a 1.5 ml Eppendorf tube and centrifuged at 600 g for 10 minutes at 4°C (84). This centrifugation step was repeated twice to ensure complete removal of cellular debris (84). The supernatant was carefully transferred into a new pre-chilled Eppendorf tube and subjected to another round of centrifugation at 9000 g for 15 minutes at 4°C (84). Following this centrifugation step, the supernatant was discarded, and the pellet, which contains the mitochondria, was resuspended in 200 µM of IMBc(+PI). The resuspended mitochondria were then subjected to centrifugation at 9000 g for 15 minutes at 4°C, and the resulting pellet was stored on ice for subsequent experiments. All the steps were performed on ice (84).

Highly purified mitochondrial fractions were obtained through Percoll (Sigma, P1644) density gradient centrifugation, following established procedures as previously outlined (107). In summary, HeLa cells were cultivated in a T175 flask approximately two days prior to the experiment (84). On the day of isolation, when the cells had reached 90-100% confluence, they were trypsinized, collected, and subsequently rinsed with PBS (84). Subsequently, the cell pellet was suspended in IBcells–1 buffer (detailed buffer compositions can be found in (107)) and subjected to homogenization using a Teflon potter (84). The resulting homogenate was then centrifuged at 600 g for 5 minutes at 4°C (84). S The supernatant, which contains mitochondria, was harvested and subjected to an additional centrifugation step at 7000 g for 10 minutes. The resulting supernatant was employed for the isolation of the cytosolic fraction (by subjecting it to further centrifugation at 10.0000 g to obtain an organelle-free cytosolic fraction), while the pellet containing mitochondria was resuspended in MRB buffer. Subsequently, Percoll medium was poured into the ultracentrifuge tube (utilizing a thin-wall ultra-clear tube, 344060 Beckman Coulter) (84). The mitochondrial suspension was layered on

top of the Percoll medium, and MRB buffer was added to the mitochondrial fraction (84). The whole assembly was then subjected to centrifugation at 95000 g for 35 minutes using an SW40 rotor from Beckman (84). Highly purified mitochondrial fractions were carefully gathered using a Pasteur pipette, followed by centrifugation at 6300 g (84). These purified mitochondrial fractions were then resuspended in MRB buffer and subjected to additional centrifugation at 6300 g to obtain the pure mitochondrial pellets (84). It's important to note that all these procedures were conducted on ice, and the centrifugations were carried out at a temperature of 4°C (84).

To perform Proteinase K treatment, the isolated pure mitochondrial fraction was exposed to 100 µg/ml of proteinase K for a duration of 30 minutes at 37°C (84). To terminate the activity of proteinase K, the mitochondrial fraction was then treated with 2 mM of Phenylmethylsulfonyl fluoride (Sigma, P7626) for 10 minutes at room temperature (84).

2.30 Patch clamp of intact mitochondria

Single-channel measurements were carried out in the mitochondria-attached configur allowing for the recording of ionic current as it traversed the outer mitochondrial membrane (84). Patch pipettes were fabricated by drawing glass capillaries with a Narishige puller (Narishige Co., Ltd., Tokyo, Japan), followed by fire-polishing, resulting in a resistance range of 12-15 MΩ. These pipettes were filled with a solution comprising the following concentrations (in mM): 100 K gluconate, 40 KCl, 3 EGTA, 10 HEPES (84). The free Ca^{2+} concentration was set to 10 µM by adding the necessary quantity of CaCl2 determined using the CaBuff program, and the pH was brought to 7.2 with KOH (84). Mitochondria were exposed to a solution with identical composition. In certain experiments, a Ca^{2+}-free pipette solution was employed, consisting of the following components (in mM): 100 K gluconate, 40 KCl, 0.3 EGTA, 10 HEPES, with pH adjusted to 7.2 using KOH (84). Single-channel currents were recorded at specific test potentials as indicated in the corresponding figures (84). Voltage steps lasting 2 seconds each were applied from the holding potential of 0 mV to reach the test potentials every 5 seconds (84). The test potentials are referenced in relation to the inner membrane surface (84). Currents were captured utilizing a patch-clamp amplifier, specifically the Axopatch 200B from Molecular Devices located in Sunnyvale, CA, USA (84). Data acquisition was conducted using the Clampex software within the pClamp suite (V9.0, Molecular Devices, Sunnyvale, CA, USA) (84). The acquired signals underwent a low-pass filtering at 1 kHz and were digitized at a sampling rate of 10 kHz, facilitated by a Digidata 1322A A/D converter from Molecular Devices

in Sunnyvale, CA, USA. Subsequently, data analysis was conducted employing the Clampfit 10.3 software within the pClamp suite from Molecular Devices, Sunnyvale, CA, USA (84).

2.31 Statistical Analysis and Reproducibility

The number of individual experiments was denoted as "n=single-cell/independent experiment" within each figure legend, accompanied by details of the employed statistical test and corresponding p-value. Statistical analyses, including Student's t-test and analysis of variance (ANOVA) with Tukey post hoc test, were carried out using GraphPad Prism software version 9.3.1 (GraphPad Software, San Diego, CA, USA) or Microsoft Excel (Microsoft Office 2013). To depict data distribution and the mean value, bar graphs with individual data points (represented as single dots) were employed, with statistical significance defined as differences with $p < 0.05$.

3 Results

3.1 Impact of Near-UV light-induced Ca^{2+} oscillations on nuclear migration of NFATc3.

This section, based on my first-author publication (Oflaz et al. 2021) (10), delves into the impact of near-UV light (405 nm) induced Ca^{2+} oscillation on the nuclear translocation of NFATc3. Briefly, it explores how near-UV light induces intracellular ROS production, resulting in Ca^{2+} oscillation through L-type Ca^{2+} channels. These repetitive Ca^{2+} oscillations, in turn, trigger the translocation of the well-known transcription factor NFATc3. Our study demonstrates that while ROS-induced Ca^{2+} oscillation leads to NFATc3 migration to the nucleus, ROS themselves do not play this role. Furthermore, our research underscores the sensitivity of pancreatic β-cells to the near-UV light (10).

3.1.1 IP_3 generating agonist induces bi-phasic nuclear migration of NFATc3.

To investigate the impact of IP_3-induced ER Ca^{2+} release on NFATc3 translocation and Ca^{2+} signaling, we employed a comprehensive experimental approach. We transfected cells with NFATc3-GFP and utilized Fura2-AM loading to monitor intracellular Ca^{2+} levels simultaneously. Upon a 3-min stimulation with the IP_3-generating agonist carbachol (CCh), we observed a rapid increase in cytosolic Ca^{2+} levels and subsequent translocation of NFATc3 to the nucleus commenced as part of the initial phase (Fig. 5a, e, f). During this primary phase, maximum translocation of NFATc3 to the nucleus was achieved within 10 minutes, followed by a gradual decline (Fig. 5a, e). Subsequently, after the 10-minute, repetitive Ca^{2+} oscillations emerged, ushering in the secondary phase of NFATc3 translocation to the nucleus (Fig. 5a, e, g). To discern the contribution of Ca^{2+} entry via L-type Ca^{2+} channels to the second phase, we employed the well-established L-type Ca^{2+} channel inhibitor, Verapamil. Applying this inhibitor, we noticed that while the initial ER Ca^{2+} release induced by CCh and the accompanying NFATc3 translocation remained unaffected, the occurrence of Ca^{2+} oscillations and the NFATc3 translocation in the second phase diminished (Fig. 5b, e, g). This implies that the L-type Ca^{2+} channel played a pivotal role in both the cytosolic Ca^{2+} oscillations and the ensuing NFATc3 nuclear translocation in the secondary phase. Subsequently, we delved into the role of mitochondrial ATP in generating Ca^{2+} oscillations during the second phase. By administering an ATP synthase inhibitor, oligomycin, we found that the ER Ca^{2+} release and NFATc3 translocation were not influenced, similar to the effects observed with Verapamil (Fig. 51c, e, g). However, the repetitive Ca^{2+} oscillation and the accumulation of NFATc3 in the nucleus

were significantly reduced during the secondary phase (Fig. 5c, e, g). This evidence suggests that the initial phase of NFATc3 translocation is unassociated with mitochondrial ATP production, whereas the Ca^{2+} oscillations fuelled by Ca^{2+} influx through the L-type Ca^{2+} channel in the secondary phase are dependent on mitochondrial ATP production.

To ascertain whether the repetitive Ca^{2+} oscillation in the secondary phase is a consequence of the CCh stimulation in the initial phase, we performed the same experiments without initial CCh stimulation. Interestingly, when cells were perfused with 2mM Ca^{2+}, we observed the onset of Ca^{2+} oscillation approximately 8 to 10 minutes later, followed by subsequent NFATc3 translocation into the nucleus (Fig. 5 d-g). These findings indicate that the Ca^{2+} oscillation and NFATc3 translocation during the secondary phase are independent of the CCh stimulation.

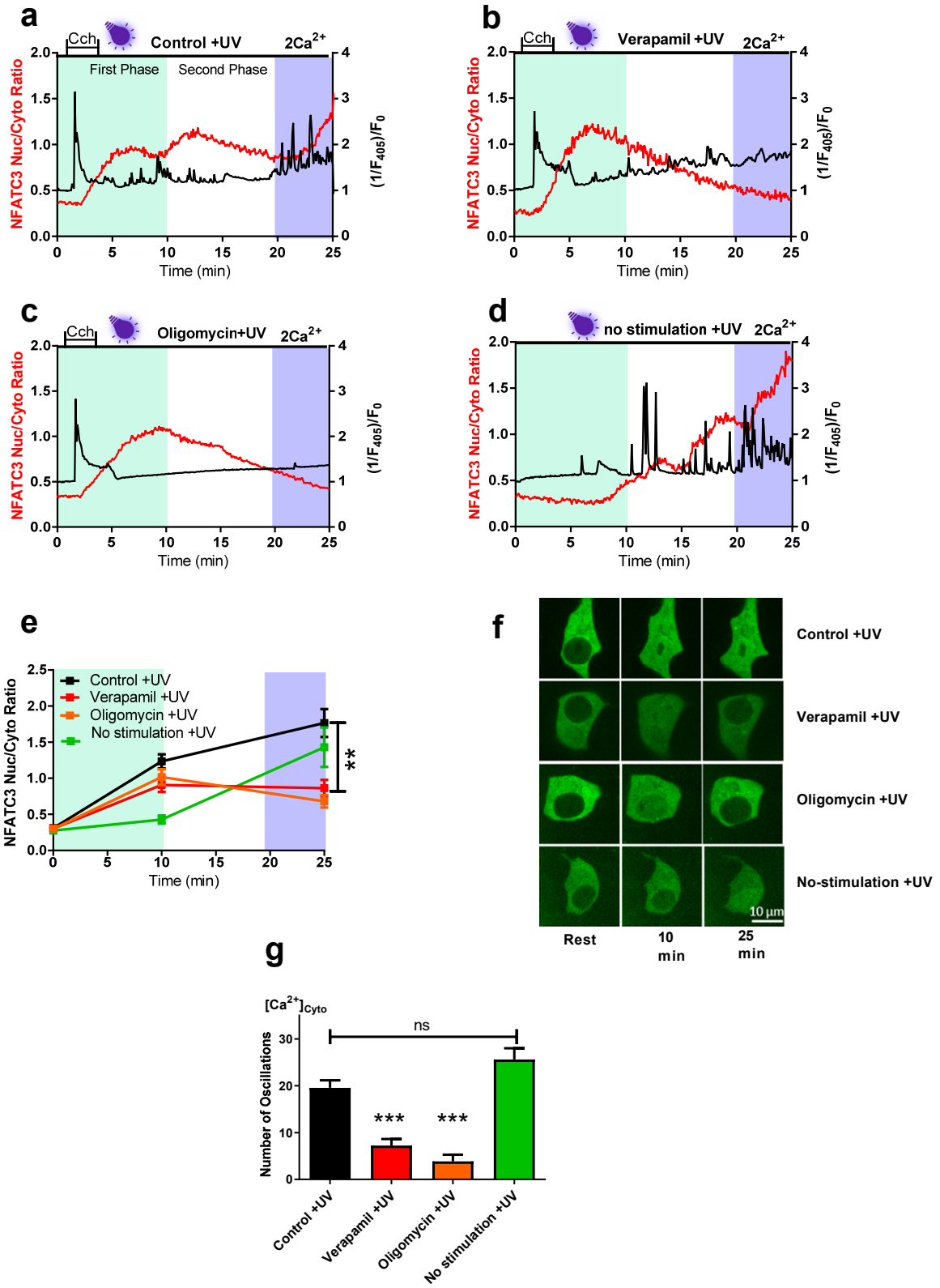

Figure 5. Regulation of Nuclear GFP-NFATc3 Translocation in INS-1 Cells. a The representative trace demonstrates the Ca^{2+} rise triggered by Carbachol stimulation (black) using Fura2-AM excited at

405 nm. At the same time, we observed GFP-NFATc3 translocation (trace) using a 488 nm laser line for cell excitation. These experiments used cells exposed to a 2 mM extracellular Ca^{2+} solution in various conditions: **a** control +UV, **b** 10 µM verapamil +UV, **c** 2 µM oligomycin +UV, and **d** no-stimulation +UV. Light green signifies the first phase of GFP-NFATc3 translocation, while white and light blue indicate the second phase. **e** GFP-NFATc3 translocation was quantified in different conditions: control +UV (black), verapamil +UV (red), oligomycin +UV (orange), and no-stimulation +UV (green), using the nucleus-to-cytosol ratio (MEAN + SEM). At minute 0, the baseline GFP-NFATc3 ratio was set, minute 10 marked the peak translocation ratio within the initial 0-10 minutes, and minute 25 indicated the maximum translocation ratio between minutes 20 and 25. **f** Representative images display NFATc3 translocation at minutes 10 and 25 (Scale bar = 10 µm). **g** The bar graphs illustrate cytosolic Ca^{2+} oscillations from 10 to 25 minutes. Statistical significance was evaluated using one-way ANOVA followed by Tukey's test, and the results are expressed as distinct p-values (** $p < 0.01$, *** $p < 0.001$, n.s.—not significant) the sample sizes are as follows: Control (n = 59), Verapamil (n = 32), Oligomycin (n = 27), and No-Stimulation (n = 22). Figure is taken from my own publication (Oflaz et al. 2021) (10).

3.1.2 Near-UV light induces cytosolic Ca^{2+} oscillations via L-Type Ca^{2+} channel which activates nuclear migration of NFATc3.

In our pursuit to unravel the underpinnings of the Ca^{2+} oscillation during the second phase, we shifted our focus to a protocol devoid of CCh stimulation. To calibrate the maximal Ca^{2+} peak attributed to the L-type Ca^{2+} channel, utilized for normalization, a 30 mM K^{+} stimulation was employed at the end of the measurements. Similar to Figure 5d, our observations revealed that perfusing cells with extracellular Ca^{2+} yielded cytosolic Ca^{2+} oscillation, coupled with NFATc3 translocation into the nucleus (Fig. 6a, e, f, g). In unstimulated states, NFATc3 localized in the cytosol. However, during measurements, consistent and robust cytosolic Ca^{2+} oscillation, coupled with GFP-NFATc3 nuclear translocation, strongly suggests that these phenomena are provoked during the measurement. Importantly, we employed a 405 nm laser for the excitation of Fura2-AM, a wavelength closely situated within the ultraviolet (UV) spectrum. It has previously been documented that this wavelength can exert an influence on cellular responses (108). To assess the potential effect of near-UV light, we repeated the same protocol, this time employing the alternate cytosolic Ca^{2+} dye Fluo-4 (λExcitation = 470 nm). Surprisingly, exciting the cells with 470 nm light failed to induce NFATc3 nuclear translocation and exhibited diminished Ca^{2+} oscillation (Fig. 6b, e, g). These findings suggest that Ca^{2+} oscillations and subsequent NFATc3 translocation into the nucleus were due to the near-UV light.

To trace the origins of near-UV light-induced Ca^{2+} oscillation, we subjected cells to verapamil treatment. Strikingly, verapamil treatment reduced the number of Ca^{2+} oscillation events to the levels observed in the absence of UV exposure and also inhibited the nuclear migration of

NFATc3 (Fig. 6c, e, g). This compellingly implicates the L-type Ca^{2+} channel as the source of near-UV light-induced Ca^{2+} oscillation. To dissect whether mitochondrial ATP production was pivotal for near-UV light-induced NFATc3 translocation to the nucleus, we administered oligomycin to the cells. In the presence of 2 mM extracellular Ca^{2+}, oligomycin treatment exhibited near-complete abolishment of cytosolic Ca^{2+} oscillation and hindered the nuclear translocation of NFATc3 (Fig. 6d-g). Taken together, these findings emphasize the indispensability of mitochondrial ATP production for the generation of near-UV light-induced cytosolic Ca^{2+} oscillations, chiefly orchestrated via the L-type Ca^{2+} channel.

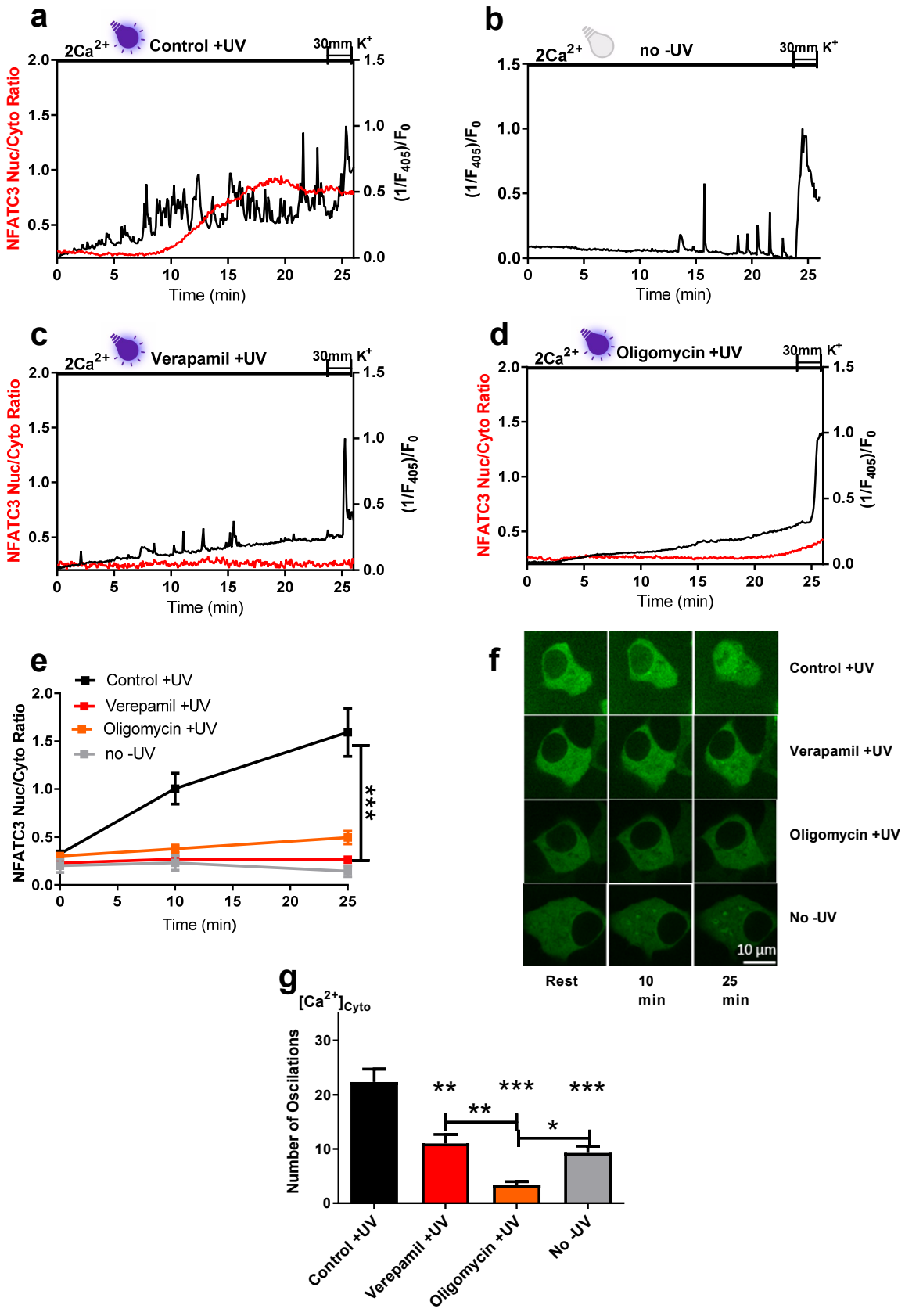
a
2Ca2+
Control +UV
30mm K+
NFATC3 Nuc/Cyto Ratio
(1/F405)/F0
Time (min)
b
2Ca2+
no -UV
30mm K+
(1/F405)/F0
Time (min)
c
2Ca2+
Verapamil +UV
30mm K+
NFATC3 Nuc/Cyto Ratio
(1/F405)/F0
Time (min)
d
2Ca2+
Oligomycin +UV
30mm K+
NFATC3 Nuc/Cyto Ratio
(1/F405)/F0
Time (min)
e
Control +UV
Verepamil +UV
Oligomycin +UV
no -UV
NFATC3 Nuc/Cyto Ratio
***
Time (min)
f
Control +UV
Verapamil +UV
Oligomycin +UV
No -UV
10 µm
Rest
10 min
25 min
g
[Ca2+]Cyto
Number of Oscillations
**
***
***
**
*
Control +UV
Verepamil +UV
Oligomycin +UV
No -UV

Figure 6. Near-UV light triggers cyclic cytosolic Ca^{2+} oscillations via the L-type Ca^{2+} channel which in turn induces NFATc3 nuclear translocation. Representative traces deoicts cytosolic Ca^{2+} oscillations (black) and GFP-NFATc3 translocation (red), in **a** control +UV, **b** no −UV, **c** 10 µM verapamil +UV, and **d** 2 µM oligomycin +UV. **e** GFP-NFATc3 translocation was measured in various conditions: control +UV (black), verapamil +UV (red), oligomycin +UV (orange), and no-stimulation +UV (green), utilizing the nucleus-to-cytosol ratio (MEAN + SEM). **f** Representative images depicting GFP-NFATc3 nuclear translocation in INS-1 cells (Scale bar = 10 µm). **g** The bar graphs illustrate cytosolic Ca^{2+} oscillations from 2 to 24 minutes. Significance was assessed using one-way ANOVA with Tukey's multiple comparison test, and the results are reported as specific p-values (* $p < 0.05$, ** $p < 0.01$, *** $p < 0.001$). Sample sizes for the GFP-NFATc3 translocation experiment are as follows: Control +UV (n = 19), Verapamil +UV (n = 18), Oligomycin +UV (n = 28), No −UV (n = 13), and for the cytosolic Ca2+ measurement, No −UV (n = 28). Figure is taken from my own publication (Oflaz et al. 2021) (10).

3.1.3 Near-UV light generates ROS production in the cytosol and mitochondria which fires the Ca^{2+} oscillations and the nuclear migration of NFATc3.

Previous studies have demonstrated that an excessive generation of ROS is linked to the occurrence of spatial Ca^{2+} oscillations (108). To delve into the causative relationship between near-UV light exposure and Ca^{2+} oscillations, we employed genetically encoded ROS sensors, cytoHyper7, and mitoHyper7, targeted respectively to the cytosol and mitochondria. To ascertain whether near-UV light, triggers ROS production, we replicated the previous experimental setup and included an additional treatment of 200 µM H_2O_2 for 2 minutes (Fig. 7a). Intriguingly, our investigations revealed that subjecting the samples to 20 mW near-UV light irradiation (high UV) resulted in a rapid and exponential escalation in both cytosolic and mitochondrial ROS production (Fig. 7a, c). In contrast, exposing the samples to 5 mW near-UV light (low UV) yielded only small alterations in mitochondrial and cytosolic ROS levels (Fig. 7a-d). These compelling findings collectively signify that the application of high UV during our measurements stimulates a robust and exponential production of ROS.

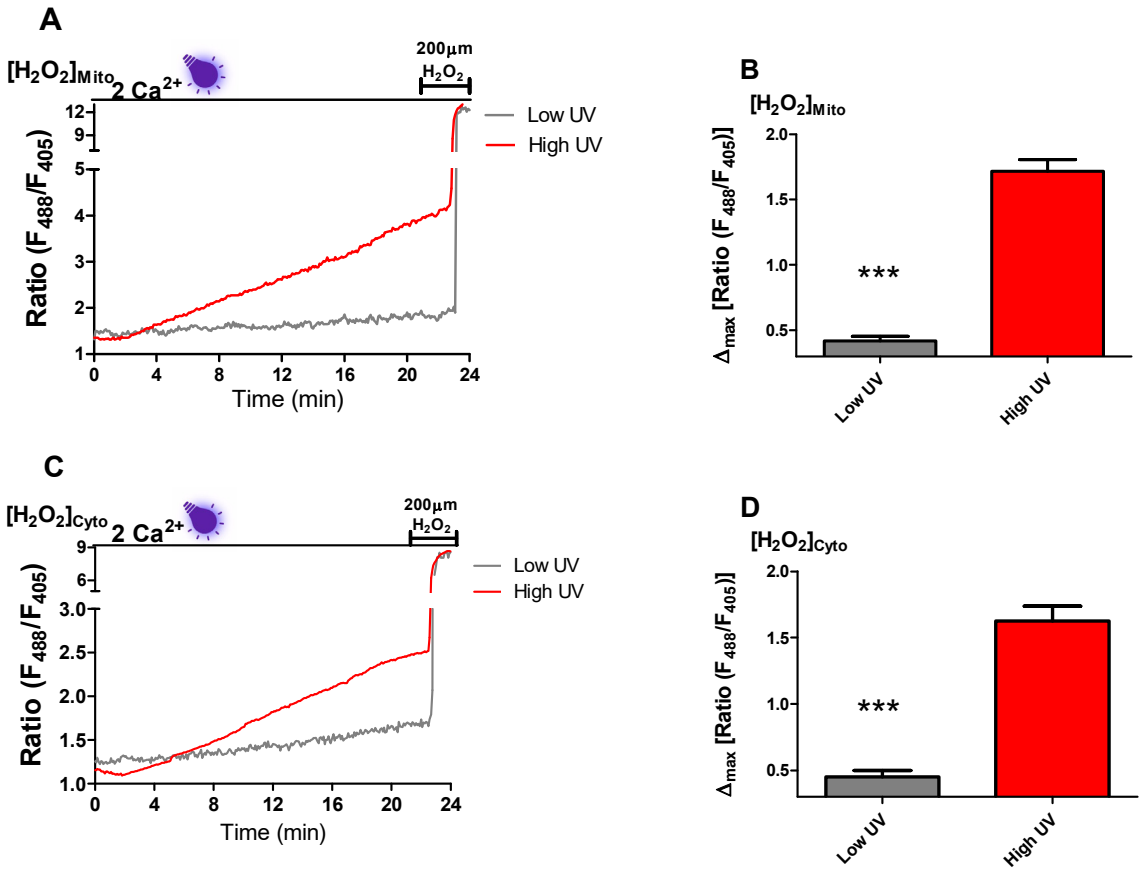

Figure 7. Near-UV light induces intracellular ROS production. Representative traces show H_2O_2 production in **a** mitochondria and **c** cytosol upon excitation with 5 mW (low-UV) and 20 mW of a 405 nm laser line (high-UV). The right panels represent MEAN + SEM of H_2O_2 levels after 20 minutes of low-UV (gray) and high-UV (red) exposure in **b** mitochondria and **d** cytosol. Significance was determined via unpaired t-tests and is denoted by specific p-values (*** $p < 0.001$). Sample sizes are as follows: Mitochondria - Low UV (n = 24) and High UV (n = 43), and Cytosol - Low UV (n = 20) and High UV (n = 30). Figure is taken from my own publication (Oflaz et al. 2021) (10).

Next, to ascertain whether the generated ROS is indeed responsible for the near-UV-induced cytosolic Ca^{2+} oscillations and the subsequent nuclear translocation of NFATc3, we pre-incubated the cells with N-Acetyl-L-cystein (NAC) for 30 minutes. Notably, NAC-treated cells exhibited a noteworthy reduction in the number of Ca^{2+} oscillations, accompanied by complete inhibition of the nuclear translocation of NFATc3 (Fig. 8a-e). Taken together, these findings provide compelling evidence that near-UV light prompts the production of ROS, which in turn initiates the distinct Ca^{2+} oscillation pattern, ultimately leading to NFATc3 translocation.

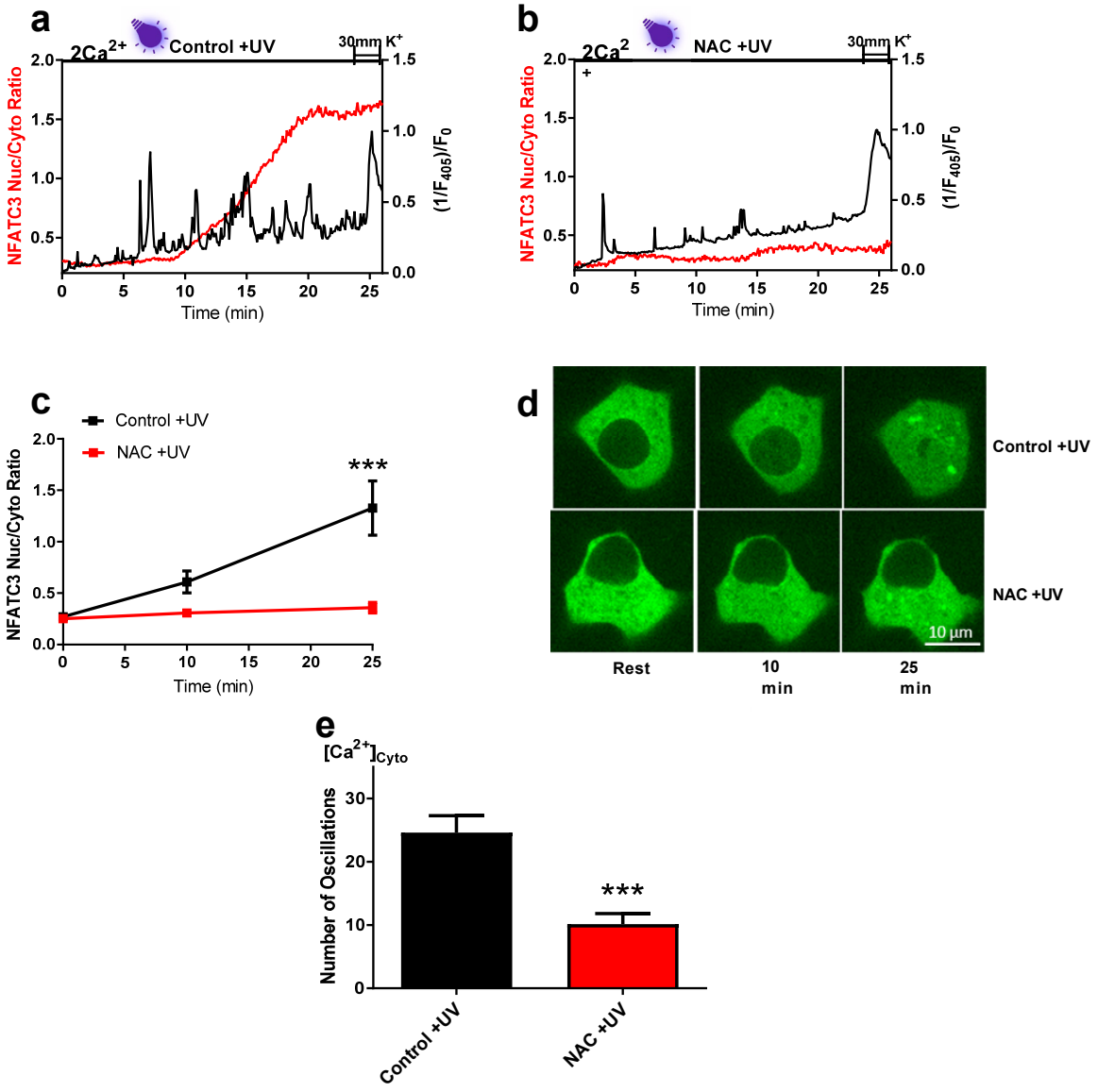

Figure 8 Application of a ROS scavenger reduces near-UV light-induced cytosolic Ca^{2+} oscillations and inhibits nuclear translocation of NFATc3. Representative trace depicts cytosolic Ca^{2+} oscillation (black) and GFP-NFATc3 translocation (red trace) **a** under normal conditions and **b** with the addition of 1 mM NAC (ROS scavenger) under UV exposure. **c** Time course of GFP-NFATc3 translocation as MEAN SEM ± in control +UV (black) and NAC +UV (red) assessed by the ratio of the nucleus to the cytosol. **d** Representative images of GFP-NFATc3 nuclear translocation in INS-1 cells (Scale bar = 10 µm). **e** Bar graphs depict the assessment of cytosolic Ca^{2+} oscillation frequency from 2 to 24 minutes. Significance was established using unpaired t-tests, with specific p-values noted as (*** $p < 0.001$). Sample sizes are as follows: Mitochondria - Control +UV (n = 18) and NAC (n = 33), Cytosol - Low UV (n = 20) and High UV (n = 30). Figure is taken from my own publication (Oflaz et al. 2021) (10).

3.1.4 Subplasmalemmal mitochondria buffers Near-UV light-induced Ca^{2+} oscillations and diminish nuclear translocation of NFATc3

We then investigated whether nuclear translocation of NFATc3 is initiated by ROS production or cytosolic Ca^{2+} oscillation. To address this question, we devised a strategy to buffer cytosolic Ca^{2+} oscillation, which is initiated through the L-type Ca^{2+} channel via enhancing the proximity between individual mitochondria and the plasma membrane by transfecting cells with an AKAP-RFP-CAAX construct. This construct employs the CAAX domain to tether individual mitochondria to the plasma membrane, enabling interaction between the CAAX domain on mitochondria and SNARE proteins present on the cell membrane (109). By co-transfecting AKAP-RFP-CAAX and NFATc3 along with Fura2-AM loading, we were able to dynamically follow Ca^{2+} oscillations with NFATc3 translocation. Upon expressing the AKAP-RFP-CAAX construct, cells displayed a reduction in the number of Ca^{2+} oscillations and a complete halt in the nuclear import of NFATc3 compared to control cells (Fig. 9a, b, e-g). This outcome pointed towards the effective buffering of local Ca^{2+} oscillation by mitochondria situated close to the L-type Ca^{2+} channel, thereby preventing NFATc3 migration. To challenge our hypothesis further, we employed MCU knockdown to compromise mitochondrial Ca^{2+} buffering. As a result, siMCU-treated AKAP-RFP-CAAX-expressing cells exhibited a notable increase in the count of Ca^{2+} oscillations compared to AKAP-RFP-CAAX-expressing cells (Fig. 9b, c, g). Intriguingly, siMCU+AKAP-RFP-CAAX-expressing cells demonstrated a nuclear translocation of NFATc3 similar to control cells (Fig. 9c-f). Moreover, cells treated with siMCU also displayed a comparable count of Ca^{2+} oscillations as well as NFATc3 translocation (Fig. 9d-g).

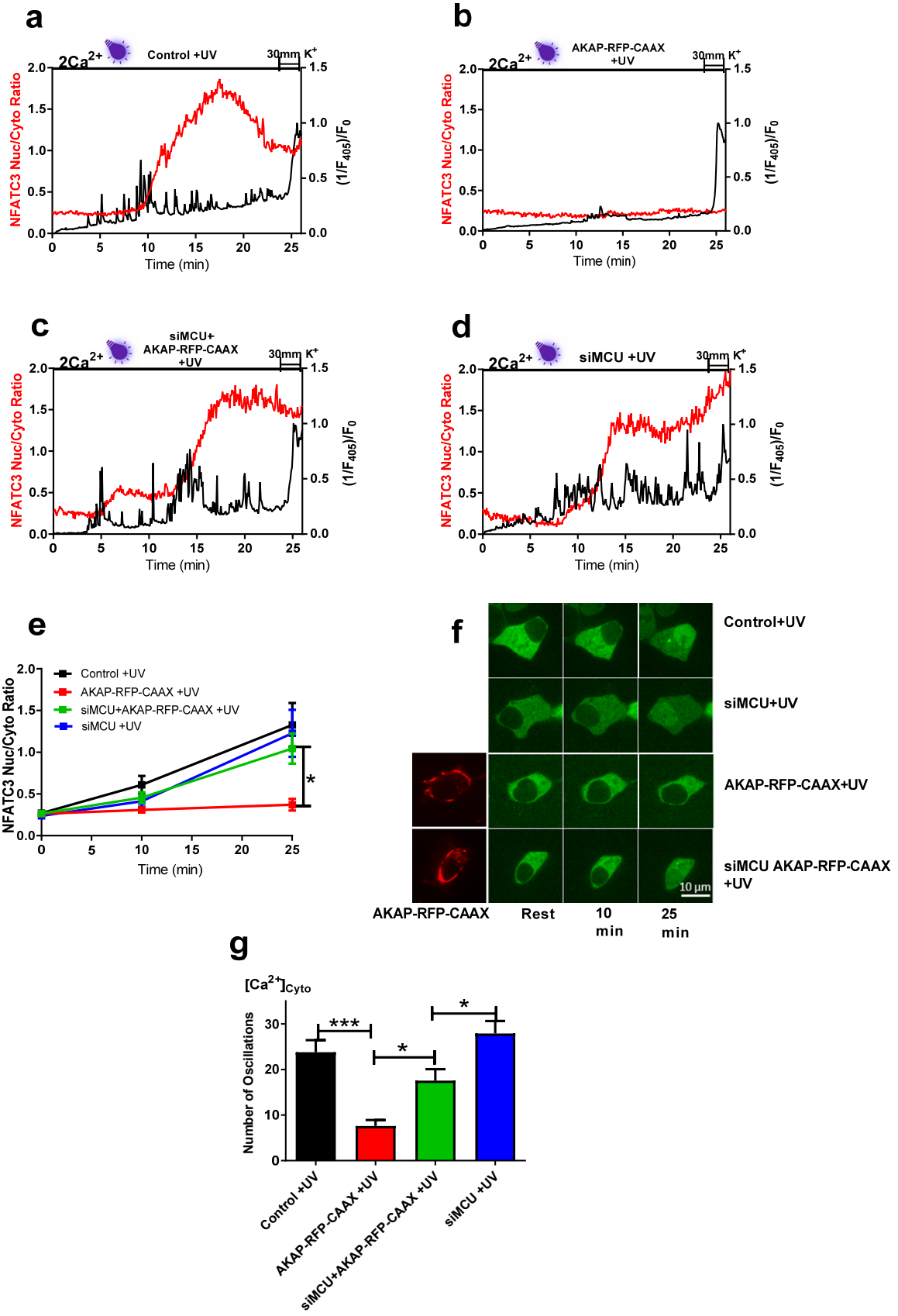
a
2Ca2+
Control +UV
30mm K+
NFATC3 Nuc/Cyto Ratio
(1/F405)/F0
Time (min)
b
2Ca2+
AKAP-RFP-CAAX +UV
30mm K+
NFATC3 Nuc/Cyto Ratio
(1/F405)/F0
Time (min)
c
2Ca2+
siMCU+ AKAP-RFP-CAAX +UV
30mm K+
NFATC3 Nuc/Cyto Ratio
(1/F405)/F0
Time (min)
d
2Ca2+
siMCU +UV
30mm K+
NFATC3 Nuc/Cyto Ratio
(1/F405)/F0
Time (min)
e
Control +UV
AKAP-RFP-CAAX +UV
siMCU+AKAP-RFP-CAAX +UV
siMCU +UV
NFATC3 Nuc/Cyto Ratio
Time (min)
*
f
Control+UV
siMCU+UV
AKAP-RFP-CAAX+UV
siMCU AKAP-RFP-CAAX +UV
10 μm
AKAP-RFP-CAAX
Rest
10 min
25 min
g
[Ca2+]Cyto
Number of Oscillations
***
*
*
Control +UV
AKAP-RFP-CAAX +UV
siMCU+AKAP-RFP-CAAX +UV
siMCU +UV

Figure 9. Assessing the impact of improved subplasmalemmal mitochondria Ca^{2+} buffering on near-UV light-induced cytosolic Ca^{2+} oscillation and nuclear migration of NFATc3. Representative traces of cytosolic Ca^{2+} oscillations (black) and GFP-NFATc3 translocation (trace) in **a** control +UV, **b** AKAP-RFP-CAAX +UV, **c** siMCU+AKAP-RFP-CAAX +UV, and **d** siMCU +UV. **e** Nuclear translocation of GFP-NFATc3 over time was assessed as MEAN + SEM for control +UV (black), AKAP-RFP-CAAX +UV (red), siMCU+AKAP-RFP-CAAX (green), and siMCU (blue), using the nucleus-to-cytosol ratio. **f** Representative images of GFP-NFATc3 nuclear translocation in INS-1 cells (Scale bar = 10 µm). Bar graphs depict the calculation of cytosolic Ca^{2+} oscillation frequency between 2 and 24 minutes. Statistical significance was determined using one-way ANOVA followed by Tukey's multiple comparison test, and the results are presented as specific p-values (* $p < 0.05$ and *** $p < 0.001$) for each group: control +UV (n = 18), AKAP-RFP-CAAX +UV (n = 30), siMCU+AKAP-RFP-CAAX +UV (n = 33), and siMCU +UV (n = 20). Figure is taken from my own publication (Oflaz et al. 2021) (10).

Subsequently, we explored whether the mitochondrial Ca^{2+} buffering ability influences near-UV light-induced ROS production in mitochondria or the cytosol. Measurement of ROS production under high near-UV irradiation across various conditions, encompassing control, MCU siRNA-treated, AKAP-RFP-CAAX-expressing, and cells with MCU knockdown in AKAP-RFP-CAAX expression, revealed consistent maximum ROS production levels (Fig. 10 a-d). Collectively, these findings underscore that near-UV light-induced spatial Ca^{2+} oscillation fires NFATc3 nuclear translocation, whereas ROS production appears not to be directly involved in this phenomenon.

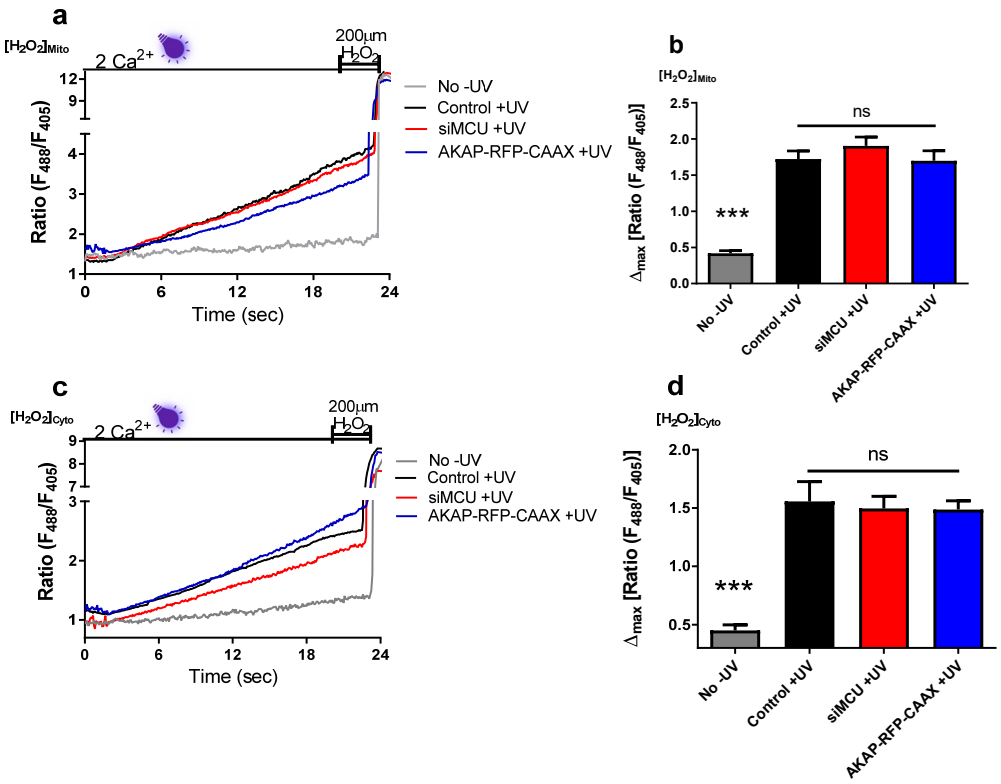

Figure 10. Near-UV light induces comparable levels of ROS production in different conditions. Representative traces show H_2O_2 production in **a** mitochondria and **c** cytosol upon excitation with 5 mW (low-UV) and 20 mW of a 405 nm laser line (high-UV) in Control +UV, siMCU +UV and AKAP-RFPCAAX +UV conditions. Bar graphs represent MEAN + SEM of H_2O_2 levels after 20 minutes of low-UV (gray) and high-UV (red) exposure in control +UV (black), siMCU +UV (red), AKAP-RFP-CAAX +UV (blue) and siMCU + AKAP-RFP-CAAX +UV (green) in mitochondria **b** and cytosol **d**. Statistical significance was evaluated with one-way ANOVA followed by Tukey's multiple comparison test, and the results are expressed as distinct *p*-values (*** $p < 0.001$, n.s. – not significant) for each group: Low-UV (n=24), Control +UV (n=46), siMCU +UV (n=19), AKAP-RFP-CAAX +UV (n=28) and siMCU + AKAP-RFP-CAAX +UV (n=13) in mitochondria and Low-UV (n=20), Control +UV (n=21), siMCU+UV (n=15), AKAP-RFP-CAAX +UV (n=16) and siMCU + AKAPRFP- CAAX +UV (n=16) in cytosol. Figure is taken from my own publication (Oflaz et al. 2021) (10).

3.2 Modulation of the Sigma-1 Receptor activity controls the cancer cell energy metabolism.

This section is based on my co-shared first-author publication (Oflaz & Koshenov et al. 2022) which focuses on the impact of the S1R on cancer cell energy metabolism (9). Briefly, we found that pharmacological activation of the S1R enhances the OXPHOS in cancer cells while reducing their reliance on aerobic glycolysis (9).

3.2.1 Sigma-1 Receptor expression differs in lung carcinoma and breast cancer cells.

To understand the role of S1R in cancer cell energy metabolism we used two human cancer cell lines with differential S1R protein expression (9). With the western blot technique, we were able to show that A549 lung adenocarcinoma cells express S1R, while MCF7 breast cancer cells show minimal S1R expression (Fig. 11a, b) thereby MCF7 cell line serves as an effective control. To downregulate the expression level of S1R in A549 cells we knockdown S1R. We achieved a 25% reduction in S1R protein levels through small interfering RNA (siRNA) knockdown in A549 cells without transfection selection markers (Figure 11B). However, our recent findings suggest that this knockdown efficiency in the whole cell population does not accurately reflect protein downregulation levels in positively transfected individual cells (73). To accurately assess the percentage of downregulated cells while excluding untransfected cells from the calculation, we quantified S1R protein downregulation in single, transfection-positive sorted A549 cells. With sorted cells, we reached up to 55% reduction in S1R expression level (Fig. 11c, d). Therefore we conducted S1R knockdown experiments with transfection selection markers for enhanced accuracy.

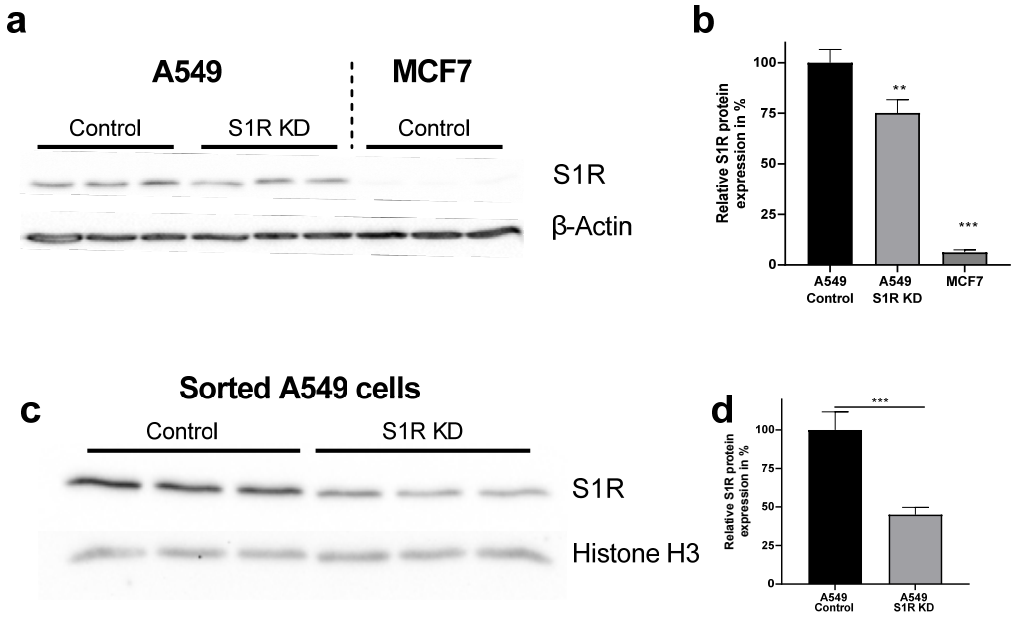

Figure 11. The Sigma-1 Receptor expression levels in A549 and MCF-7 cell lines. a Immunoblot images show S1R expression levels in two conditions: control siRNA and siRNA directed against S1R (on the left) in A549 cells, alongside non-transfected MCF7 cells (on the right). **b** Bar charts depict the levels of S1R expression (MEAN±SEM) in A549 cells treated with control siRNA, S1R-targeting siRNA, and non-transfected MCF7 cells. **c** Immunoblot image reveals S1R expression levels in sorted, transfection-positive A549 cells, either transfected with control siRNA or siRNA targeting S1R. **d** Bar graphs display the mean ± SEM of S1R expression levels in sorted A549 cells. Statistical significance was determined using one-way ANOVA with Tukey's multiple comparison tests (for b) or unpaired t-test (for d) and denoted as (** $p < 0.01$, *** $p < 0.001$). Sample sizes were as follows: A549 cells - A549 Control (n = 3), A549 S1R KD (n = 3); MCF7 (n = 3); sorted A549 cells Control (n = 3), sorted A549 S1R KD (n = 3). Figure is taken from my own publication (Oflaz & Koshenov et al. 2022) (9).

3.2.2 Pharmacological modulation of Sigma-1 Receptor activity regulates mitochondrial bioenergetics: Activation enhances it, while inhibition has no impact.

The effect of ligand activation and inhibition of S1R on intracellular Ca^{2+} homeostasis has been previously shown (72,73). However, the role of S1R in mitochondrial energy metabolism has not been studied before. To investigate the roles of S1R in cellular energy metabolism upon activation or inhibition with well-characterized S1R ligands, we conducted real-time mitochondrial-matrix ATP measurements (Fig. 12a(i–iii)). Therefore, we employed a comprehensive two-phase protocol previously published by our group (59). The first phase involves glucose removal, where we perfuse the cells with a glucose-containing buffer for 2

minutes and then remove the glucose. This phase offers insights into the cellular dependence on glucose metabolism, mainly reflecting the flow of glycolytic ATP. Once we reach the reduced plateau phase of mitochondrial ATP levels, we reintroduce the glucose-containing buffer to restore mitochondrial ATP levels to their basal state before entering the second phase (Fig. 12a). The second stage encompasses the introduction of oligomycin, which indicates the mitochondrial ATP generation and OXPHOS levels. By calculating the ratio of the second phase to the first phase, we assessed the cell's metabolic state and its preference for OXPHOS versus glycolysis (Fig. 12a(i–iii)). Pre-incubating the cells with the S1R agonist, SKF-10047, known to activate S1R (110), enhanced mitochondrial bioenergetics in A549 cells, increasing their reliance on mitochondrial ATP production over glycolysis (Fig. 12b) (numbers ≥ 1 in Fig. 12b indicate a greater Oxphos than Glycolysis). In contrast, pre-incubation with the S1R antagonist BD-1047 (111) had no impact on the metabolic status and mitochondrial bioenergetics (Fig. 12b). We assessed whether the effect of S1R ligands is specific. Therefore, we knocked down S1R in A549 cells. Neither the S1R agonist nor the antagonist had any effect on S1R-depleted A549 cells, nor did they affect MCF7 cells (Fig. 12c, d). Furthermore, preincubation of transiently S1R-expressing MCF7 cells with agonist enhanced mitochondrial bioenergetics, whereas antagonist had no impact (Fig. 12d, e). These findings emphasize S1R's role in promoting OXPHOS upon activation, while its inactivation has a limited impact on energy metabolism, suggesting S1R's resting state inactivity in cellular energy metabolism.

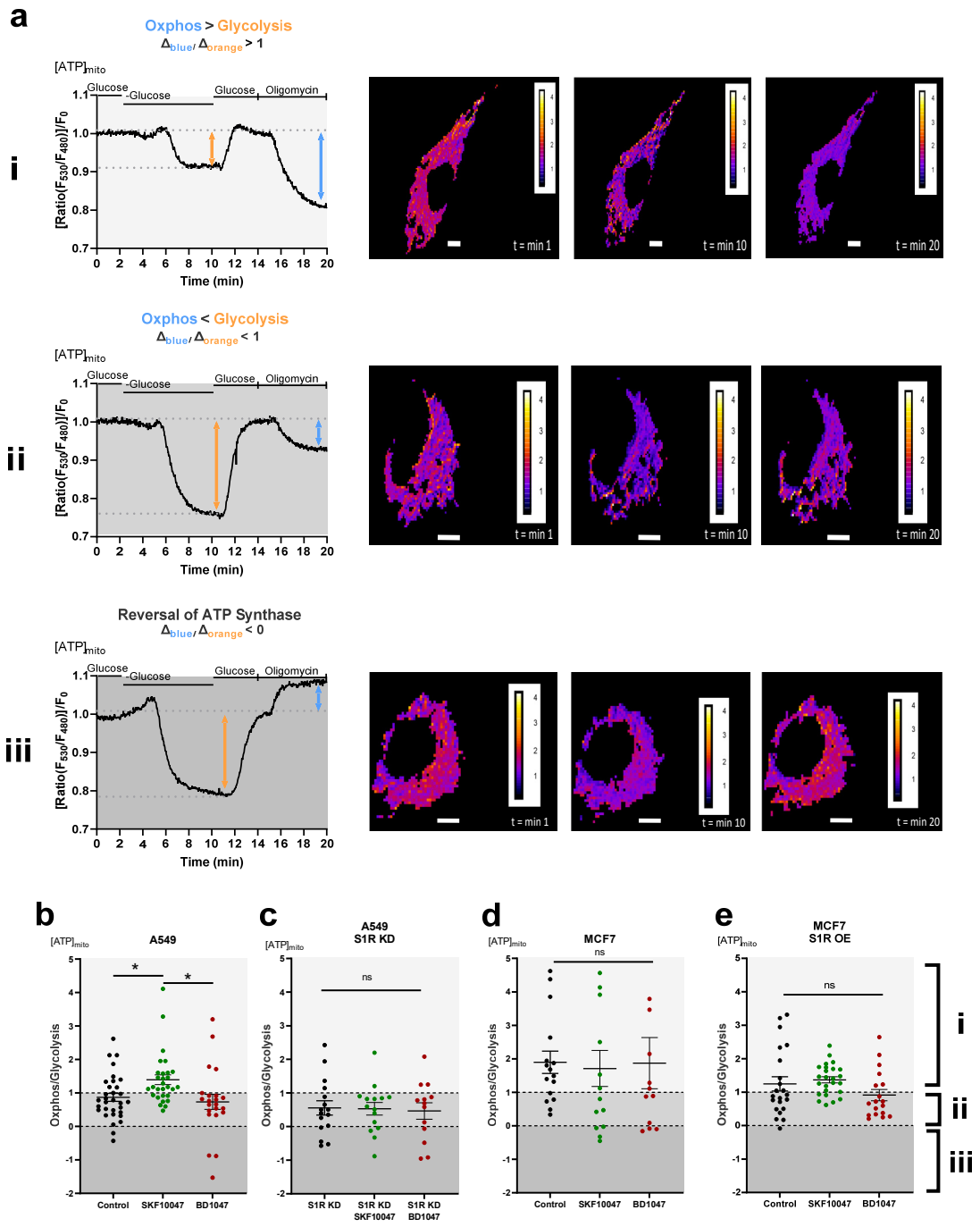

Figure 12. Impact of pharmacological modulation of Sigma-1 Receptor on mitochondrial energy metabolism. a Exemplary recordings of mitochondrial ATP levels, accompanied by corresponding representative visuals of cells transfected with mtAT.1.03, are presented in MCF7 (i) and A549 (ii, iii) cell lines. The cells have been assigned pseudocolors to indicate mitochondrial ATP levels, expressed as the mtAT1.04 ratio, and calibration bars have been included on the right side of the cells for reference (Scale bar = 10 µm). The change in the ratio of oligomycin addition to glucose deprivation was utilized as an Oxphos/Glycolysis ratio and is presented as Oxphos > Glycolysis (a(i)), Oxphos < Glycolysis

(a(ii)), and the reversal of ATP synthase (a(iii)). In panels (b-e), the white area (marked as (i)) signifies Oxphos > Glycolysis, the light gray area (indicated as (ii)) signifies Oxphos < Glycolysis and the dark gray area (denoted by (iii)) signifies the reversal of ATP synthase. Scatter plots displaying individual values represent the Oxphos-to-Glycolysis ratio with mean ± SEM for the following conditions: **b** A549 cells: Control (black), Control+SKF10047 (green), Control+BD1047 (red). **c** A549 cells: S1R KD (black), S1R KD +SKF10047 (green), S1R KD +BD1047 (red). **d** MCF7 cells: Control (black), Control+SKF10047 (green), Control+BD1047 (red). **e** MCF7 cells with S1R OE: Control (black), Control+SKF10047 (green), Control+BD1047 (red). Cells were pre-treated with the respective ligands 2-4 hours before each experiment. Statistical significance was determined using one-way ANOVA with Tukey's multiple comparison test and is presented as (* $p < 0.05$, ns: not significant). Sample sizes were as following: For A549 cells: Control (32/16), Control + SKF10047 (29/15), Control + BD1047 (22/13), S1R KD (16/10), S1R KD + SKF10047 (15/10), S1R KD + BD1047 (13 /8), For MCF7 cells: Control (15/6), Control + SKF10047 (13/4), Control + BD1047 (11/5), S1R OE (22/7), S1R OE + SKF10047 (25/8), S1R OE + BD1047 (18 /5). Figure is taken from my own publication (Oflaz & Koshenov et al. 2022) (9).

3.2.3 Pharmacological activation of Sigma-1 Receptor boosts mitochondrial membrane potential and reduces aerobic glycolysis, while its inhibition enhances glycolysis.

Next, we examined the effect of S1R ligands on Ψm. To do this, we used tetramethylrhodamine methyl ester (TMRM) dye, which accumulates in the mitochondria in response to Ψm (Fig. 13a). In line with our previous experiment, the activation of S1R with its agonist increased Ψm in A549 cells. In contrast, the S1R antagonist had no effect (Fig. 13a). Similarly, as seen in the mitochondrial ATP measurements, neither agonist nor antagonist affected Ψm in MCF7 cells (Fig. 13c). These results collectively suggest that S1R activation with the agonist significantly contributes to the enhancement of OXPHOS therefore boost Ψm. The lack of effect with the antagonist implies that S1R remains dormant in terms of this specific function.

To monitor changes in cellular energy levels, we utilized a state-of-the-art genetically encoded sensor named Lapronic, specifically designed to measure the pyruvate-to-lactate ratio in the cytosol (112) which serves as a valuable indicator of cell's preference for aerobic glycolysis versus OXPHOS. Upon activation of S1R with its agonist, we observed an increase in the pyruvate/lactate ratio in A549 cells, as well as in MCF7 cells with transient S1R expression (Fig. 13e, h). However, S1R activation did not affect the cytosolic pyruvate-to-lactate ratio in S1R-depleted A549 cells and also in MCF7 cells (Fig. 13f, g). Notably, S1R antagonist BD1047, as well as the depletion of S1R, led to a reduction in the pyruvate/lactate ratio in A549 cells (Fig. 13e, f). These results suggest that S1R activation with its agonist in A549 cells and

MCF7 cells overexpressing S1R results in reduced production of lactate compared to pyruvate. Consequently, redirects pyruvate toward the TCA cycle. Conversely, a decreased pyruvate/lactate ratio (as we observed in BD1047 preincubation and S1R depletion in A549 cells) indicates that the cell contains relatively more lactate compared to pyruvate, suggesting a higher rate of aerobic glycolysis. Moreover, S1R inactivation or depletion appears to increase aerobic glycolysis without affecting mitochondrial ATP production or Ψm, indicating a hidden role of S1R's basal involvement in balancing aerobic glycolysis and OXPHOS. These measurements added new insights into the role of S1R under basal conditions, upon activation or inactivation.

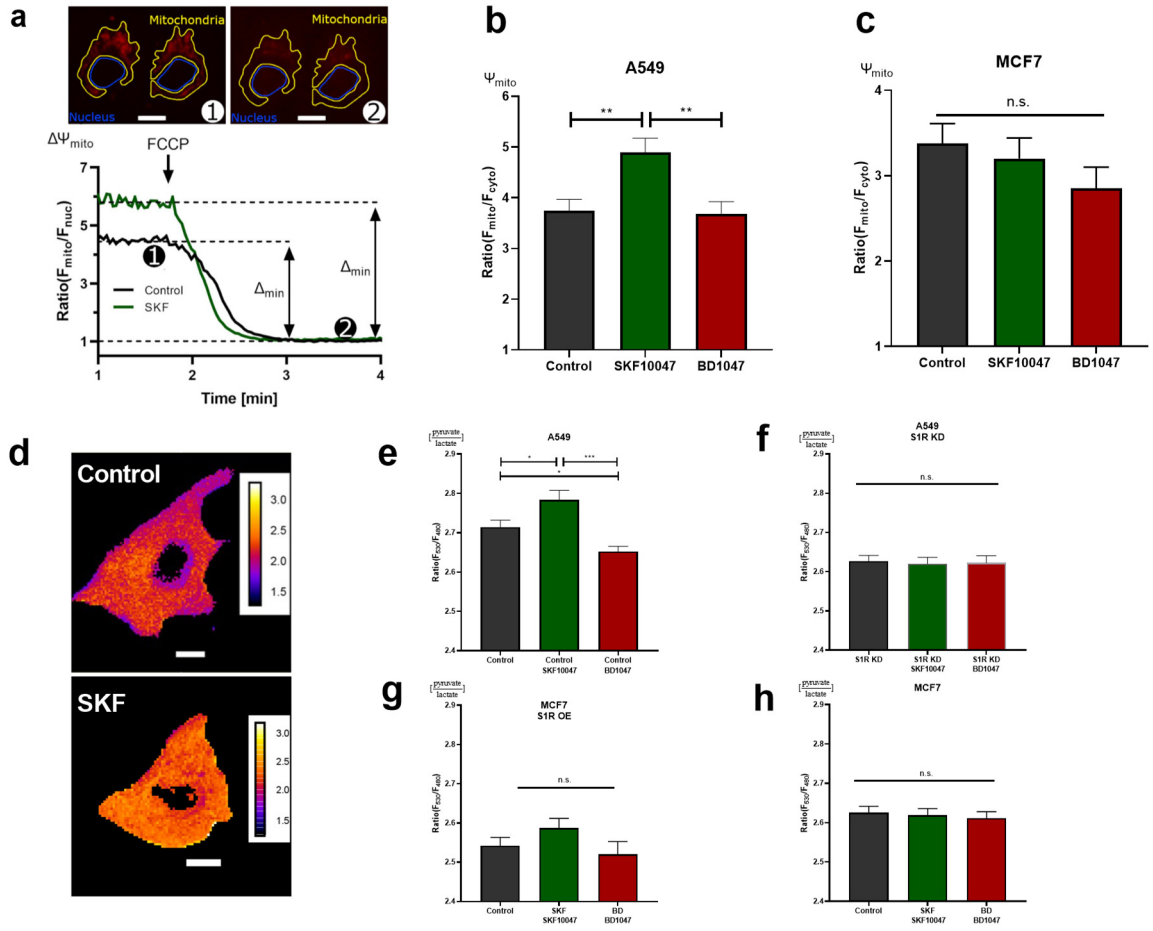

Figure 13. Sigma-1 Receptor ligands regulate the energy metabolism of cancer cells. a Representative images of A549 cells stained with TMRM, along with designated regions of interest (ROI) for both mitochondria and the nucleus are displayed (scale bar = 10 μm). The experimental protocol is displayed, including representative ratio traces of mitochondrial-to-nucleus ROIs for both control (black) and control+SKF10047 (green). The protocol described in **a** was employed to assess mitochondrial membrane potential for Control (black) and Control+SKF10047 (green) by measuring the change in fluorescence ratio in mitochondria and the nucleus following 1 μM FCCP treatment. **b** Bar graphs display

the mitochondrial membrane potential with mean ± SEM for Control (black), Control+SKF10047 (green), and Control+BD1047 (red) in A549 cells and **c** MCF7 cells. **d** Representative images of A549 cells transfected with a ratiometric pyruvate/lactate sensor. The upper image represents the Control condition, while the lower image represents Control+SKF10047. The cells have been pseudocolored to indicate the pyruvate/lactate ratio and calibration bars are included on the right-hand side of both cells for reference (Scale bar = 10 µm). **e** Bar graphs with mean ± SEM depict the cytoplasmic ratio of pyruvate to lactate for A549 cells, including Control (black), Control+SKF10047 (green), Control+BD1047 (red), **f** S1R KD (black), S1R KD +SKF10047 (green), and S1R KD +BD1047 (red), **g** in MCF7 cells for Control (black), Control+SKF10047 (green), Control+BD1047 (red) and **h** in MCF7 cells with S1R OE, for Control (black), Control+SKF10047 (green), and Control+BD1047 (red). Cells were pre-treated with the respective ligands 2-4 hours before each experiment. Statistical differences were assessed using one-way ANOVA with Tukey's multiple comparison test and are presented as follows: (* $p < 0.05$, ** $p < 0.01$, *** $p < 0.001$, ns: not significant). Sample sizes were as follows: TMRM Measurements: For A549 cells: Control (90/4), Control + SKF10047 (114/5), and Control + BD1047 (92/4). For MCF7 cells: Control (72/4), Control + SKF10047 (111 /4), and Control + BD1047 (81/4). Pyruvate to Lactate Ratio: For A549 cells: Control (69/6), Control + SKF10047 (60/6), and Control + BD1047 (69/6). S1R KD (58/5), S1R KD + SKF10047 (49 /4), and S1R KD + BD1047 (45/4). For MCF7 cells: Control (54 /4), Control + SKF10047 (52 /4), and Control + BD1047 (53/4). For MCF7 cells with S1R-mCherry OE: Control (65/8), Control + SKF10047 (83/9), and Control + BD1047 (49/7). Figure is taken from my own publication (Oflaz & Koshenov et al. 2022) (9).

3.2.4 Activation of Sigma-1 Receptor with agonist enhances mitochondrial Ca^{2+} access capacity.

As Ca^{2+} plays a critical role in regulating mitochondrial bioenergetics, we investigated whether S1R ligands influence mitochondrial Ca^{2+} levels. To do so, we transfected A549 and MCF7 cells with the genetically encoded matrix-targeted ratiometric Ca^{2+} sensor, 4mtD3cpv (96). Pre-treatment of cells with an S1R agonist resulted in increased mitochondrial matrix Ca^{2+} levels under both resting and IP_3-induced ER Ca^{2+} release conditions in A549 cells (Fig. 14a-c). However, this effect was abolished upon S1R depletion in A549 cells (Fig. 14d-f) and in MCF7 cells (Fig. 14g-i). Transient expression of the S1R-mCherry construct in MCF7 cells mimicked the increase in basal mitochondrial Ca^{2+} levels induced by (+)-SKF10047 but did not affect mitochondrial Ca^{2+} uptake upon IP_3-induced ER Ca^{2+} release (Fig. 14j-l). These results collectively provide mechanistic insights into the OXPHOS-promoting effect of S1R activation by (+)-SKF10047, where the S1R agonist enhances mitochondrial bioenergetics by increasing mitochondrial matrix Ca^{2+} levels under resting and upon ER Ca^{2+} release. This specific function of (+)-SKF10047 boosts the activity of mitochondrial matrix-residing Ca^{2+}-sensitive dehydrogenases and IMS-residing Ca^{2+}-sensitive metabolite shuttles (11). In contrast to the

S1R agonist, the S1R antagonist BD1047 did not affect mitochondrial Ca^{2+} levels under either resting conditions or upon IP_3-induced ER Ca^{2+} release (Fig. 14).

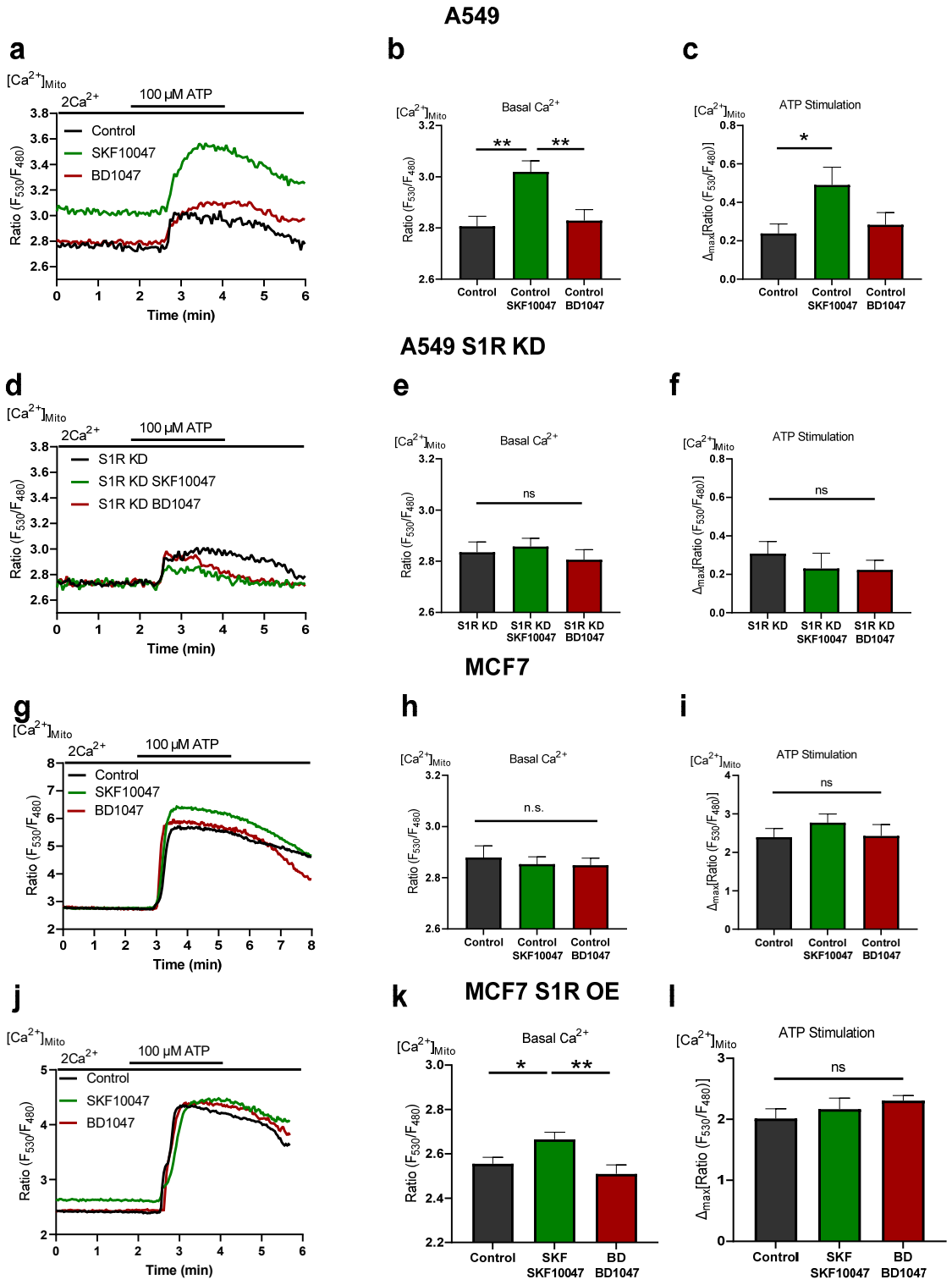

Figure 14. Activation of the Sigma-1 Receptor enhances mitochondrial Ca^{2+} signaling both under basal conditions and upon ER Ca^{2+} release. a Mean curve of mitochondrial Ca^{2+} dynamics measured using 4mtD3cpv in A549 cells under different conditions: Control (black), Control+SKF10047 (green), and Control+BD1047 (red). **b** The bar graphs display the mean ± SEM of basal mitochondrial Ca^{2+} levels for A549 cells under different conditions: Control (black), Control+SKF10047 (green), and Control+BD1047 (red). **c** The bar graphs present the mean ± SEM of ATP (100 µM) induced mitochondrial Ca^{2+} uptake for A549 cells in different conditions: Control (black), Control+SKF10047 (green), and Control+BD1047 (red). **d** Representative traces of mitochondrial Ca^{2+} dynamics measured in A549 cells under different conditions: S1R KD (black), S1R KD +SKF10047 (green), and S1R KD +BD1047 (red). **e** The bar graphs display the mean ± SEM of basal mitochondrial Ca^{2+} levels for A549 cells under different conditions: S1R KD (black), S1R KD +SKF10047 (green), and S1R KD +BD1047 (red). **f** The bar graphs present the mean ± SEM of ATP (100 µM) induced mitochondrial Ca^{2+} uptake for A549 cells in different conditions: S1R KD (black), S1R KD +SKF10047 (green), and S1R KD +BD1047 (red). **g** Representative traces of mitochondrial Ca^{2+} dynamics measured in MCF7 cells under different conditions: Control (black), Control+SKF10047 (green), and Control+BD1047 (red). **h** The bar graphs display the mean ± SEM of basal mitochondrial Ca^{2+} levels for MCF7 cells under different conditions: Control (black), Control+SKF10047 (green), and Control+BD1047 (red). **i** The bar graphs present the mean ± SEM of ATP (100 µM) induced mitochondrial Ca^{2+} uptake for MCF7 cells in different conditions: Control (black), Control+SKF10047 (green), and Control+BD1047 (red). **j** Representative traces of mitochondrial Ca^{2+} dynamics measured in S1R-mCherry OE MCF7 cells under different conditions: Control (black), Control+SKF10047 (green), and Control+BD1047 (red). **k** The bar graphs display the mean ± SEM of basal mitochondrial Ca^{2+} levels for S1R-mCherry OE MCF7 cells under different conditions: Control (black), Control+SKF10047 (green), and Control+BD1047 (red). **l** The bar graphs present the mean ± SEM of ATP (100 µM) induced mitochondrial Ca^{2+} uptake for S1R-mCherry OE MCF7 cells in different conditions: Control (black), Control+SKF10047 (green), and Control+BD1047 (red). Statistical differences were evaluated using one-way ANOVA with Tukey's multiple comparison test and are presented as specific p-values: (* $p < 0.05$, ** $p < 0.01$, ns: not significant). Sample sizes were as following: A549 Cells Basal Ca^{2+} Measurements: Control (44/9), Control + SKF10047 (44/8), Control + BD1047 (38/7), S1R KD (32/7), S1R KD + SKF10047 (43/8), S1R KD + BD1047 (25/7), A549 Cells ATP Stimulation: Control (17/9), Control + SKF10047 (20/8), Control + BD1047 (18/7), S1R KD (11/7), S1R KD + SKF10047 (12/8), and S1R KD + BD1047 (9 /7). MCF7 Cells Basal Ca^{2+} Measurements: Control (34/3), Control + SKF10047 (54/5), and Control + BD1047 (44 /4). MCF7 Cells ATP Stimulation: Control (16/3), Control + SKF10047 (18/5), and Control + BD1047 (20/4). S1R-mCherry OE MCF7 Cells Basal Ca^{2+} Measurements: Control (26/6), Control + SKF10047 (31/6), and Control + BD1047 (22/6). S1R-mCherry OE MCF7 Cells ATP Stimulation: Control (17/6), Control + SKF10047 (17/6), and Control + BD1047 (14/6). Figure is taken from my own publication (Oflaz & Koshenov et al. 2022) (9).

Subsequently, we sought to determine whether the activation of S1R with an agonist amplifies the efficient transfer of Ca^{2+} from the ER to the mitochondria or merely elevates cytosolic Ca^{2+} levels initially. To address this question, we transfected cells with the genetically encoded FRET-based cytosolic Ca^{2+} sensor, D3cpv (96). Our findings revealed that neither the S1R agonist nor the antagonist had any discernible impact on cytosolic Ca^{2+} levels (Fig. 15). These results suggest that the activation of S1R indeed directs the flow of Ca^{2+} ions from the ER to the mitochondria, thus contributing to mitochondrial bioenergetics.

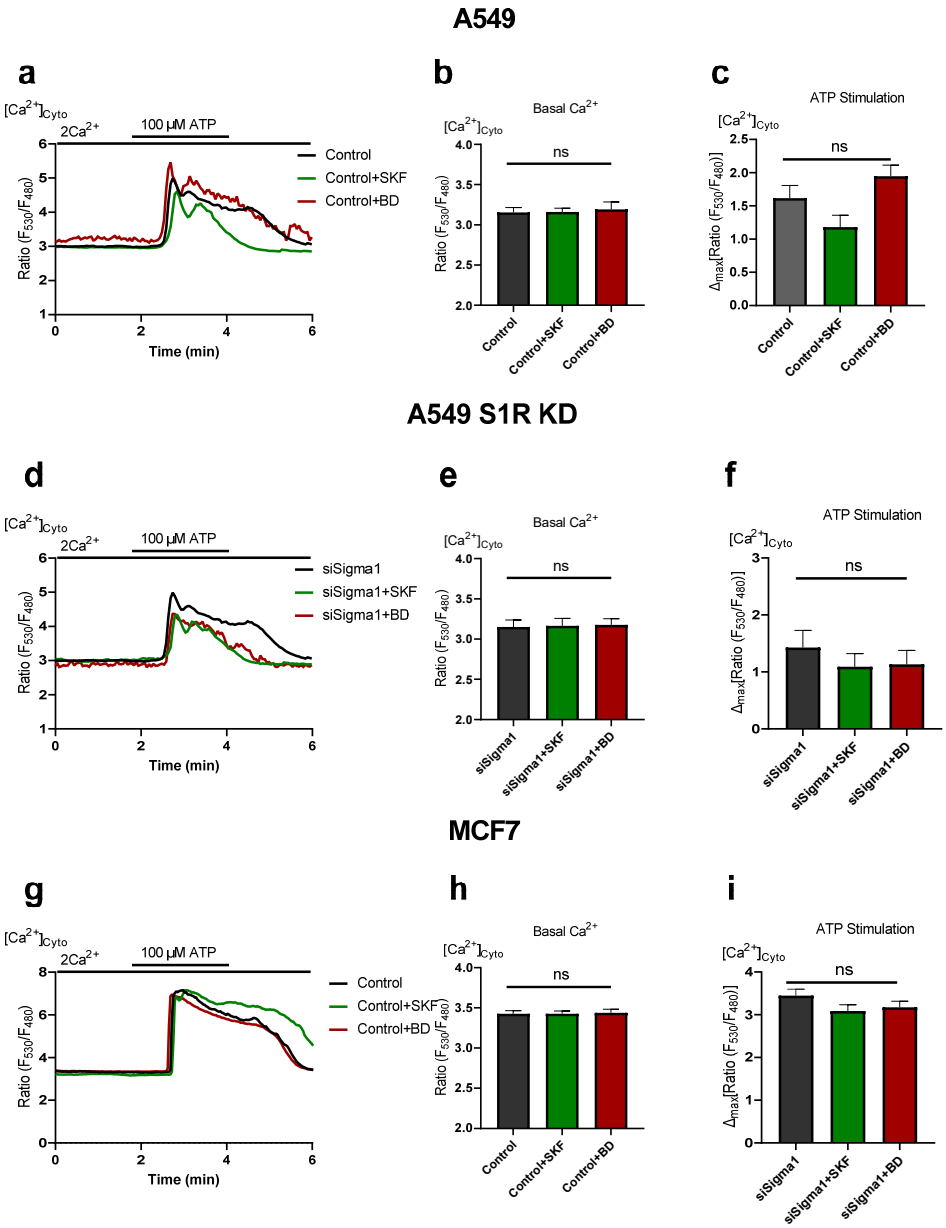

Figure 15. Effect of S1R ligands on cytosolic Ca^{2+} levels. a Representative traces of cytosolic Ca^{2+} dynamics measured using D3cpv in A549 cells under different conditions: Control (black),

Control+SKF10047 (green), and Control+BD1047 (red). **b** The bar graphs display the mean ± SEM of basal cytosolic Ca^{2+} levels for A549 cells under different conditions: Control (black), Control+SKF10047 (green), and Control+BD1047 (red). **c** The bar graphs present the mean ± SEM of ATP (100 μM) induced cytosolic Ca^{2+} levels for A549 cells in different conditions: Control (black), Control+SKF10047 (green), and Control+BD1047 (red). **d** Representative traces of cytosolic Ca^{2+} dynamics measured in A549 cells under different conditions: S1R KD (black), S1R KD +SKF10047 (green), and S1R KD +BD1047 (red). **e** The bar graphs display the mean ± SEM of basal cytosolic Ca^{2+} levels for A549 cells under different conditions: S1R KD (black), S1R KD +SKF10047 (green), and S1R KD +BD1047 (red). **f** The bar graphs present the mean ± SEM of ATP (100 μM) induced cytosolic Ca^{2+} rise for A549 cells in different conditions: S1R KD (black), S1R KD +SKF10047 (green), and S1R KD +BD1047 (red). **g** Representative traces of cytosolic Ca^{2+} dynamics measured in MCF7 cells under different conditions: Control (black), Control+SKF10047 (green), and Control+BD1047 (red). **h** The bar graphs display the mean ± SEM of basal cytosolic Ca^{2+} levels for MCF7 cells under different conditions: Control (black), Control+SKF10047 (green), and Control+BD1047 (red). **i** The bar graphs present the mean ± SEM of ATP (100 μM) induced cytosolic Ca^{2+} rise for MCF7 cells in different conditions: Control (black), Control+SKF10047 (green), and Control+BD1047 (red). Statistical differences were evaluated using one-way ANOVA with Tukey's multiple comparison tests and are presented as specific p-values: (ns: not significant). A549 cells basal Ca^{2+} measurements: Control (30/6), Control + SKF10047 (33/ 7), Control + BD1047 (36/6), SR1 KD (27/7), S1R KD + SKF10047 (29/8) and S1RKD + BD1047 (27/7). A549 cells ATP stimulation: Control (14/6), Control + SKF10047 (13/7), Control + BD1047 (21/6), SR1 KD (14/7), S1R KD + SKF10047 (15 /8) and S1RKD + BD1047 (12 /7). MCF7 cells basal Ca^{2+} measurements: Control (33/3), Control + SKF10047 (44/4), and Control + BD1047 (45/3). MCF7 cells ATP stimulation: Control (14/3), Control + SKF10047 (17/4) and Control + BD1047 (18/ 3). Figure is taken from my own publication (Oflaz & Koshenov et al. 2022) (9).

3.3 Role of AnxA5 on mitochondrial Ca^{2+} homeostasis and apoptosis

This section is based on my first-author paper (Oflaz et al, 2023, under review) (84). In this study, we focused on the role of AnxA5 in intracellular Ca^{2+} signaling. Our findings revealed that AnxA5 regulates IMS Ca^{2+} signaling by facilitating Ca^{2+} permeability of VDAC1 upon ER Ca^{2+} release. Additionally, we discovered that AnxA5 controls the dimerization of VDAC1, thereby affecting apoptotic cell death in response to cisplatin treatment (84).

3.3.1 AnxA5 regulates the mitochondrial matrix Ca^{2+} homeostasis

To investigate the potential role of AnxA5 in regulating mitochondrial Ca^{2+} balance, we utilized the CRISPR/Cas method to generate AnxA5 knockout (AnxA5-KO) cells in both HeLa and EA.hy926 cell lines (Fig. 16a, b). We checked the Ca^{2+} levels within the mitochondrial matrix Ca^{2+} by using a genetically encoded ratiometric Ca^{2+} sensor, 4mtD3cpv (96), specifically targeted to the mitochondrial matrix. Under baseline conditions, mitochondrial matrix Ca^{2+} levels were similar between wild-type (WT) and AnxA5-KO cells in HeLa (Figure 16c, d) and EA.hy926 cells (Figure 16f, g). Strikingly, stimulation of these cells with an IP_3-generated agonist which leads to ER Ca^{2+} release led to a significant reduction in mitochondrial matrix Ca^{2+} signaling in HeLa (Figure 16c, e) and EA.hy926 cells (Figure 16f, h). Furthermore, transiently expressing AnxA5 in the KO cells successfully restored the mitochondrial matrix Ca^{2+} signal induced by the IP_3-generating agonist ATP (Figure 16c-e).

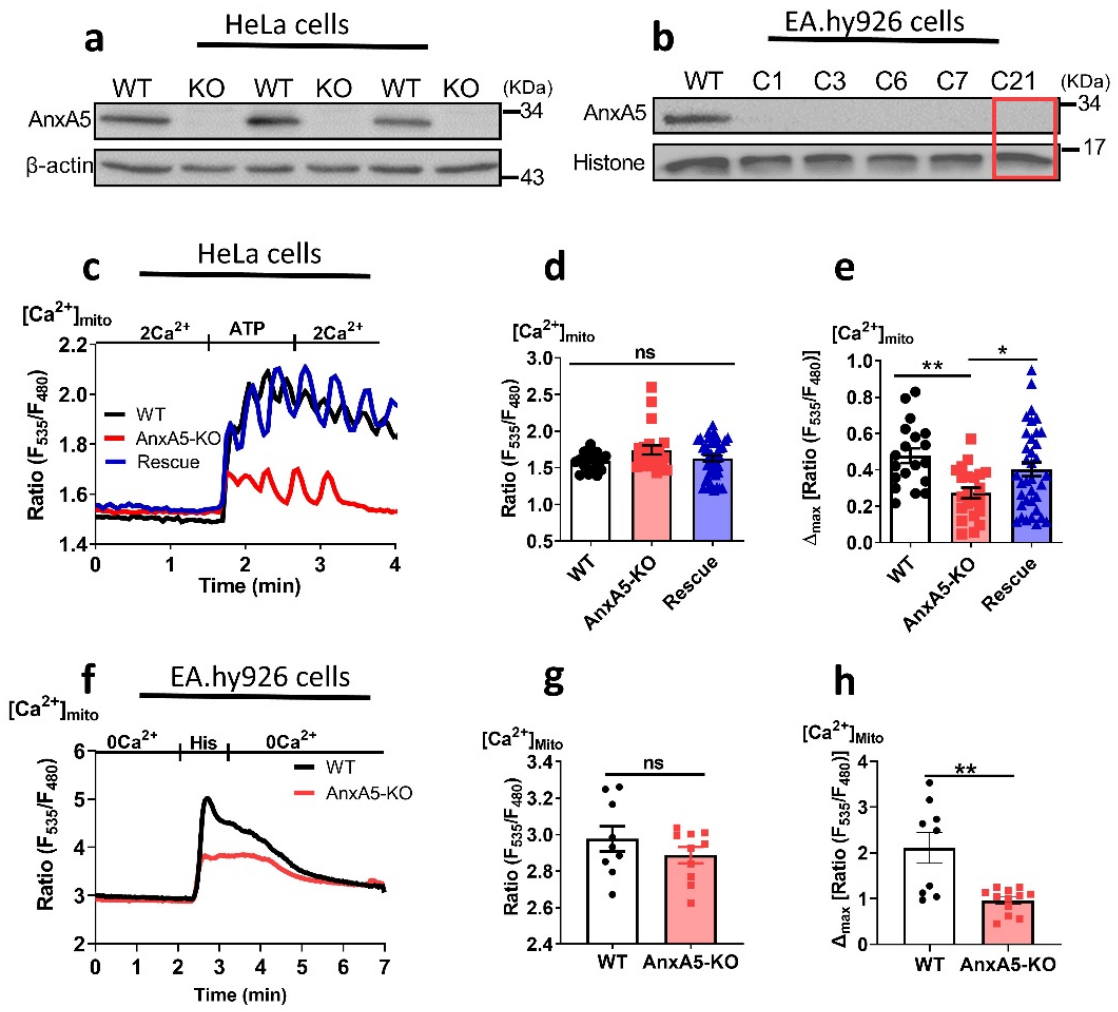

Figure 16. AnxA5 dynamically regulates mitochondrial matrix Ca^{2+} signaling in HeLa and EA.hy926 cell lines. a Immunoblots display AnxA5 expression in WT and AnxA5-KO HeLa and **b** EA.hy926 cells (experiments are performed with clone 21). **c** Average traces of the ATP-induced matrix Ca^{2+} responses in HeLa cells. **d** The bar graphs depict basal and **e** maximum matrix Ca^{2+} levels in WT (black), AnxA5-KO (red), and Rescue (blue). Data points represent the mean ± SEM with sample sizes indicated as WT = 19/5; AnxA5-KO = 22/5; Rescue = 36/9. **f** Average traces of 100 µM ATP-induced matrix Ca^{2+} responses in WT (black) and AnxA5-KO (red) EA.hy926 cells. **g** Bar graphs depict basal and **h** ATP-induced maximum matrix Ca^{2+} levels in WT (black) and AnxA5-KO (red) cells. Data points show the mean ± SEM with sample sizes of WT = 9/6; and AnxA5-KO = 12/6. Significant differences were determined using one-way ANOVA with Tukey's multiple comparison tests (* $p < 0.05$, ** $p < 0.01$) or the unpaired Student's t-test (** $p < 0.001$), with "ns" indicating no significance. Figure is taken from my own publication (Oflaz et al, 2023) (84).

Subsequently, we delved into the underlying cause for the diminished mitochondrial Ca^{2+} signaling in response to IP_3-triggered ER Ca^{2+} release observed in both HeLa cells and EA.hy926 AnxA5-KO cells. To confirm whether the absence of AnxA5 has an impact on the

level of ER Ca^{2+} release, we measured cytosolic Ca^{2+} levels using cytosolic Ca^{2+} dye Fura2-AM. Under baseline conditions or following agonist stimulation, the cytosolic Ca^{2+} levels in AnxA5-KO-HeLa cells closely resembled those in WT HeLa cells (Figure 17 a-c). In EA.hy926 cells, basal cytosolic Ca^{2+} levels were also similar between AnxA5-KO and WT cells (Figure 17 d, e). However, compared to WT cells, AnxA5-KO EA.hy926 cells displayed an amplified cytosolic Ca^{2+} rise upon ER Ca^{2+} release (Figure 17 d, f), indicating a diminished capacity for mitochondrial Ca^{2+} buffering in AnxA5KO EA.hy926 cells.

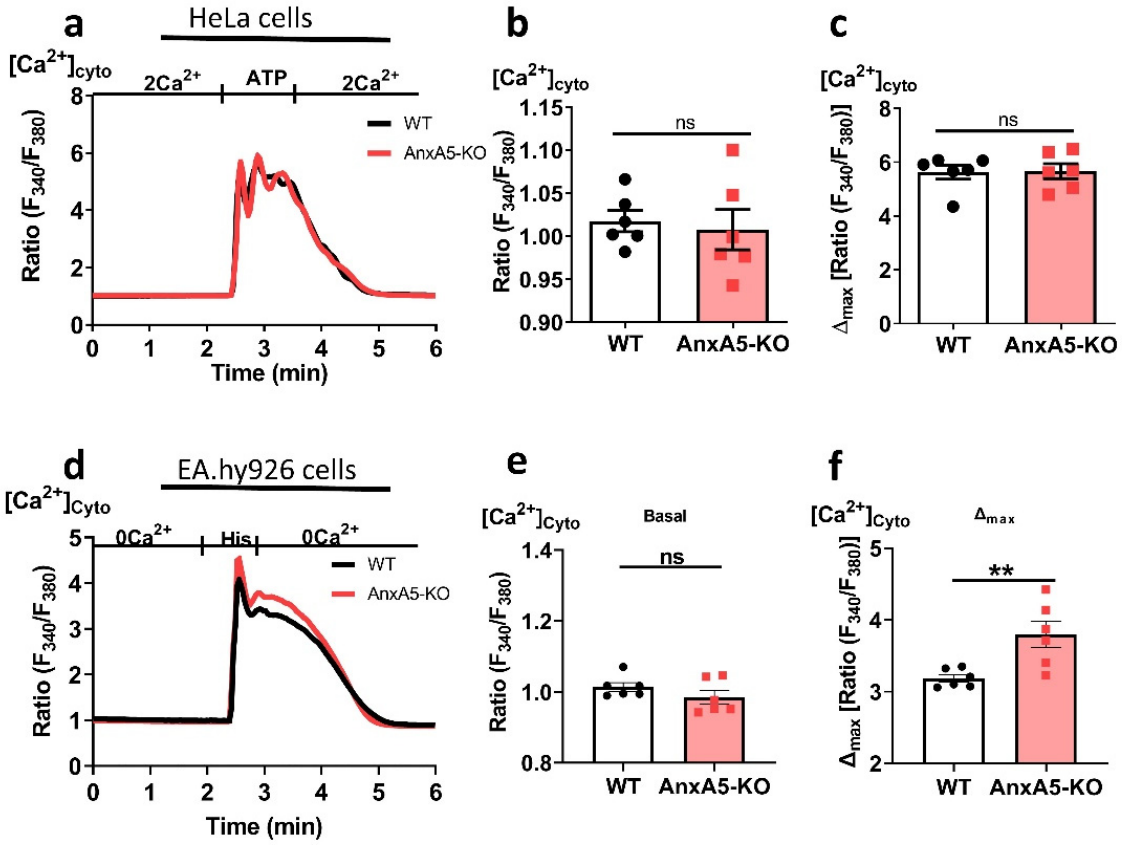

Figure 17. AnxA5 regulates mitochondrial matrix Ca^{2+} signaling in perivascular cells isolated from AnxA5KO mice. a Average traces of the ATP-induced matrix Ca^{2+} responses in perivascular cells. **b** The bar graphs depict basal and **c** maximum matrix Ca^{2+} levels in WT (black) and AnxA5-KO (red) cells. Data points represent the mean ± SEM with sample sizes indicated as WT = 29/6 and AnxA5-KO = 40/6. **d** Average cytosolic Ca^{2+} responses to 100 µM ATP in perivascular cells for WT (black) and AnxA5-KO (red). **e** Bar graphs display basal and **f** ATP-induced maximum cytosolic Ca^{2+} levels for WT (black) and AnxA5-KO (red). Data points show the mean ± SEM with sample sizes WT = 46/6 and AnxA5-KO = 33/6. Significant differences were determined using the unpaired Student's t-test (** $p < 0.001$), with "ns" indicating no significance. Figure is taken from my own publication (Oflaz et al, 2023) (84).

Additionally, we tracked ER Ca^{2+} levels by employing a genetically encoded ratiometric Ca^{2+} sensor explicitly targeted to the ER (97). To capture the dynamic ER Ca^{2+} changes, cells were stimulated with an IP_3-generating agonist in the absence of extracellular Ca^{2}, followed by perfusion with a Ca^{2+}-containing buffer to observe how quickly the ER replenished its Ca^{2+} stores in WT and AnxA5KO cells (Figure 18a). Notably, both the release of Ca^{2+} from the ER triggered by IP_3 and its subsequent refilling kinetics were comparable between WT and AnxA5-depleted cells (Figure 18a, b). Moreover, when we inhibited the SERCA by using tert-Butylhydroquinone (BHQ), we observed similar depletion kinetics in both WT and AnxA5-KO cells indicating that AnxA5 is not involved in the ER Ca^{2+} signaling (Figure 18a-c). Moreover, to exclude any potential differences in the rate at which NCLX removes Ca^{2+} between WT and AnxA5-depleted cells, we stimulated the cells with histamine while using the NCLX inhibitor CGP37157. Notably, the NCLX inhibitor prevented the extrusion of Ca^{2+} from the mitochondria in AnxA5-depleted cells without impacting the maximum increase in matrix Ca^{2+}, ruling out the possibility of AnxA5 regulating the activity rate of NCLX (Figure 18d). These findings underscore that AnxA5 contributes to the mitochondrial matrix Ca2+ signaling without affecting ER Ca^{2+} signaling, cytosolic Ca^{2+} homeostasis, and the NXLX activity

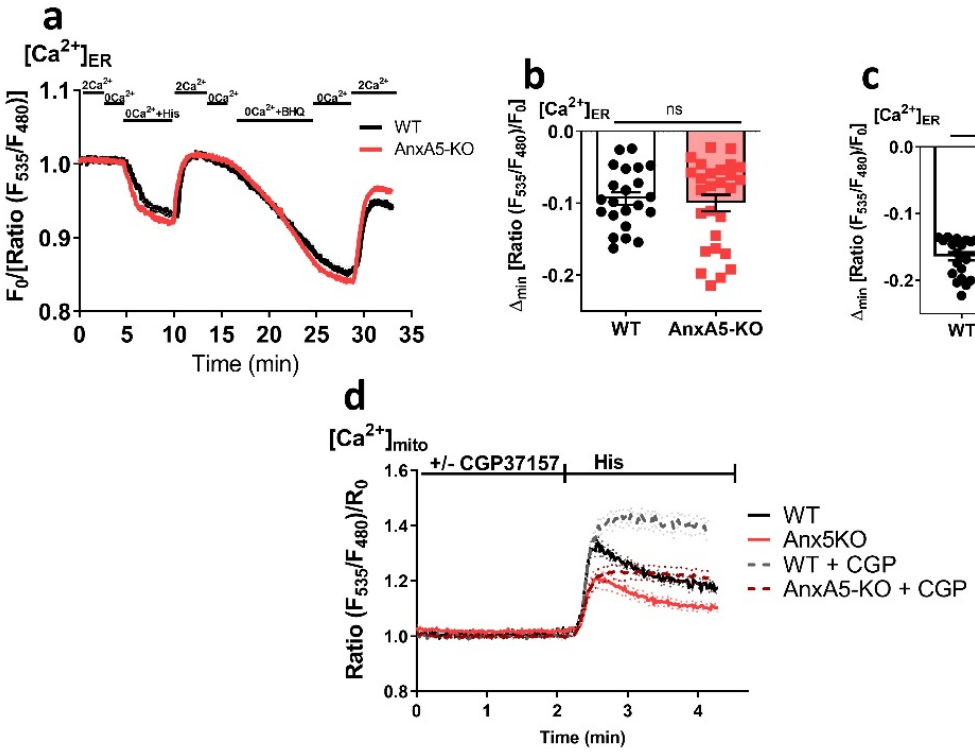

Figure 18. AnxA5 is not involved in ER Ca^{2+} signaling and mitochondrial Ca^{2+} extrusion. a Average treaces of ER Ca^{2+} responses to histamine and BHQ in WT (black) and AnxA5-KO (red) HeLa cells. **b** Bar graphs depict ER Ca^{2+} responses to 100 µM histamine and **c** 15 µM BHQ in WT (black) and AnxA5-

KO (red) cells. Data points represent the mean ± SEM with sample sizes of WT = 22/4 and AnxA5-KO = 27/5. **d** Average traces of 100 µM histamine-induced matrix Ca^{2+} responses in HeLa cells with and without CGP37157 for WT (black) and AnxA5KO (red). Data points show the mean ± SEM with sample sizes as follows: WT = 29/3, AnxA5-KO = 28/4, WT-CGP37157 = 56/3, AnxA5-KO-CGP37157 = 43/4. Significant differences were determined using the unpaired Student's t-test ("ns" for not significant). Figure is taken from my own publication (Oflaz et al, 2023) (84).

To rule out the potential off-target effect of AnxA5KO clones, we checked the mitochondrial matrix Ca^{2+} levels in perivascular cells (PCs) isolated from both WT and AnxA5-KO mice (99,113). Similar to our observations in HeLa and Ea.hy926 cells, baseline matrix Ca^{2+} levels were comparable between WT and AnxA5KO PCs (Figure 19a, b). However, upon ATP-induced ER Ca^{2+} release, we observed a pronounced reduction in mitochondrial matrix Ca^{2+} levels in AnxA5KO cells (Figure 19a, c). Importantly, both the baseline and ATP-induced cytosolic Ca^{2+} elevations were comparable in WT and AnxA5KO PCs (Figure 19d-f). These results collectively underscore AnxA5's pivotal role in regulating mitochondrial matrix Ca^{2+} homeostasis.

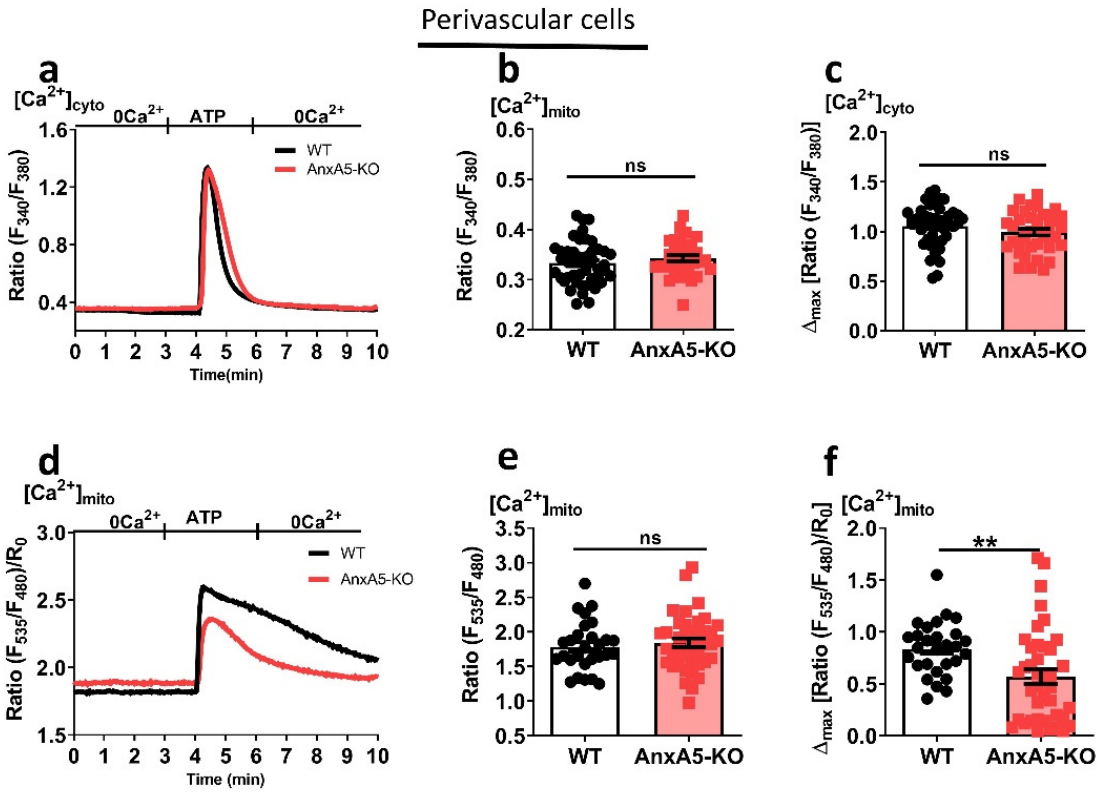

Figure 19. AnxA5 controls the mitochondrial matrix Ca^{2+} signaling in perivascular cells. a Average traces of ATP-induced matrix Ca^{2+} responses in WT (black) and AnxA5-KO (red) perivascular cells. **b** Bar graphs depict basal and **c** ATP-induced maximum matrix Ca^{2+} levels in WT (black) and AnxA5-KO

(red) cells. Data points show the mean ± SEM with sample sizes of WT = 29/6 and AnxA5-KO = 40/6. d Average traces of ATP-induced matrix Ca^{2+} responses in WT (black) and AnxA5-KO (red) perivascular cells. **e** Bar graphs depict basal and **f** ATP-induced maximum cytosolic Ca^{2+} levels in WT (black) and AnxA5-KO (red) cells. Data points represent the mean ± SEM with sample sizes of WT = 46/6 and AnxA5-KO = 33/6. Significant differences were evaluated using the unpaired Student's t-test (** $p < 0.001$, "ns" for not significant). Figure is taken from my own publication (Oflaz et al, 2023) (84).

3.3.2 Depletion of AnxA5 does not influence Ψ_{mito} and expression level of Ca^{2+} uniporter machinery

Given that Ψmito plays a crucial role in governing efficient mitochondrial Ca^{2+} sequestration by providing the driving force for ion influx (114), we investigated the impact of AnxA5 depletion on Ψmito. Using Tetramethylrhodamine, Methyl Ester, Perchlorate (TMRM), a cationic dye that binds to mitochondria based on their membrane potential, we demonstrated that the absence of AnxA5 had no impact on Ψmito (Figure 20a, b). Subsequently, we checked the expression levels of crucial proteins associated with mitochondrial Ca^{2+} signaling, namely VDAC1, MICU1, UCP2, and MCU (Figure 20c). Immunoblot quantification demonstrated similar expression levels of the tested proteins in both WT and AnxA5-KO HeLa cells (Figure 20c, d). Taken together, these findings collectively indicate that the reduction in mitochondrial matrix Ca^{2+} signaling observed in AnxA5-KO cells is not a result of changes in protein expression levels associated with mitochondrial Ca^{2+} homeostasis or modifications in Ψ_{mito}.

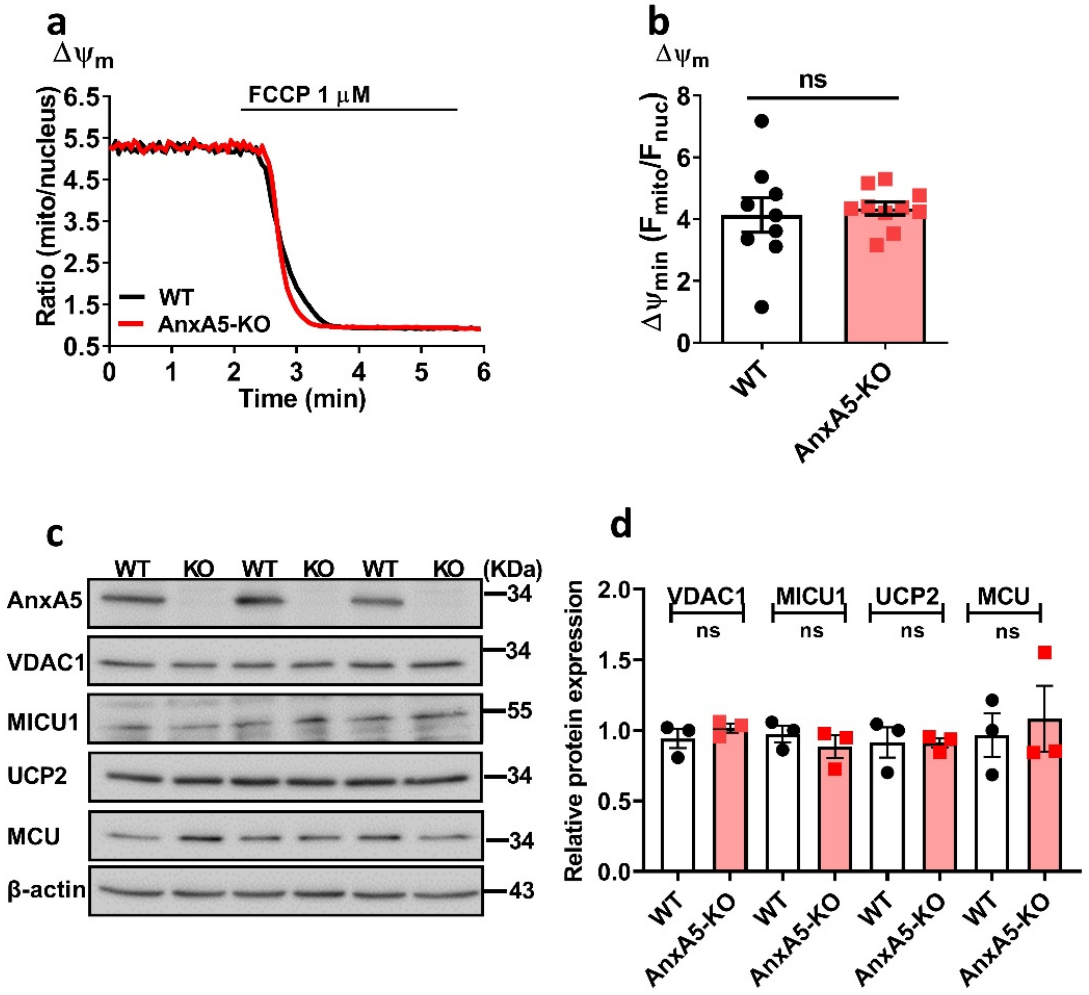

Figure 20. Effect of AnxA5 on Ψ_{mito} and expression level of proteins responsible for mitochondrial Ca^{2+} homeostasis. a Average traces of Ψ_{mito} before and after FCCP treatment in TMRM-stained HeLa cells, with WT (Black) and AnxA5-KO (red).b Bar graph depicts mitochondrial membrane potential. Data points indicate the mean ± SEM with sample sizes of WT =87/9; and AnxA5-KO =106/10. **c** Immunoblots show the expression level of AnxA5, VDAC1, MICU1, UCP2, and MCU in WT and AnxA5-KO HeLa cell lysates. **d** Bar graph shows the expression level analysis of the respective proteins. Data points indicate the mean ± SEM with sample sizes of WT = 87/9 and AnxA5-KO = 106/10. Significant differences were evaluated using the unpaired Student's t-test ("ns" for not significant). Figure is taken from my own publication (Oflaz et al, 2023) (84).

3.3.3 AnxA5 depletion has no impact on MAMs but alters the structure of mitochondria

Mitochondria form connections with the ER through structures known as "mitochondrial-associated ER membranes" (MAMs), enabling mitochondria to benefit from localized Ca^{2+} hotspots driven by IP_3-mediated ER Ca^{2+} release (16,115). Any disruption in these contact

sites could potentially impede the effective transfer of Ca^{2+} from the ER to the mitochondria (116). To assess the integrity of ER-mitochondria contact sites in both WT and AnxA5KO cells, we employed 3D-confocal microscopy (Figure 21a). The analysis, as indicated by the Pearson correlation coefficient, revealed that MAM regions were comparable in WT and AnxA5-depleted cells (Figure 21b). Additionally, we explored mitochondrial morphology in WT and AnxA5-depleted cells (Figure 21a). Interestingly, we observed that AnxA5-depleted cells have an increased mitochondrial volume (Figure 21c), and elevated branching factor (Figure 21d).

We proceeded to investigate whether the elevated mitochondrial volume influence the cristae architecture. To this end, we evaluated mitochondrial structure by examining crista membrane density and distribution by employing transmission electron microscopy (TEM) (Figure 21e). The assessment of cristae membrane density, determined by the ratio of cristae membrane length to mitochondrial length and cristae membrane length to mitochondrial area, showed no significant changes in AnxA5-depleted cells (Figure 21e-g). We then examined the distribution of cristae membrane within each single mitochondria by analyzing consecutive circular sections as depicted illustrate at Figure 21h. We found an increase in cristae membrane density in AnxA5KO cells, particularly concentrated in the central region of mitochondria (Figure 21i). These findings underscore the crucial role of AnxA5 in modulating mitochondrial architecture, potentially through the regulation of mitochondrial Ca^{2+} signaling, which will be discussed in broader detail below.

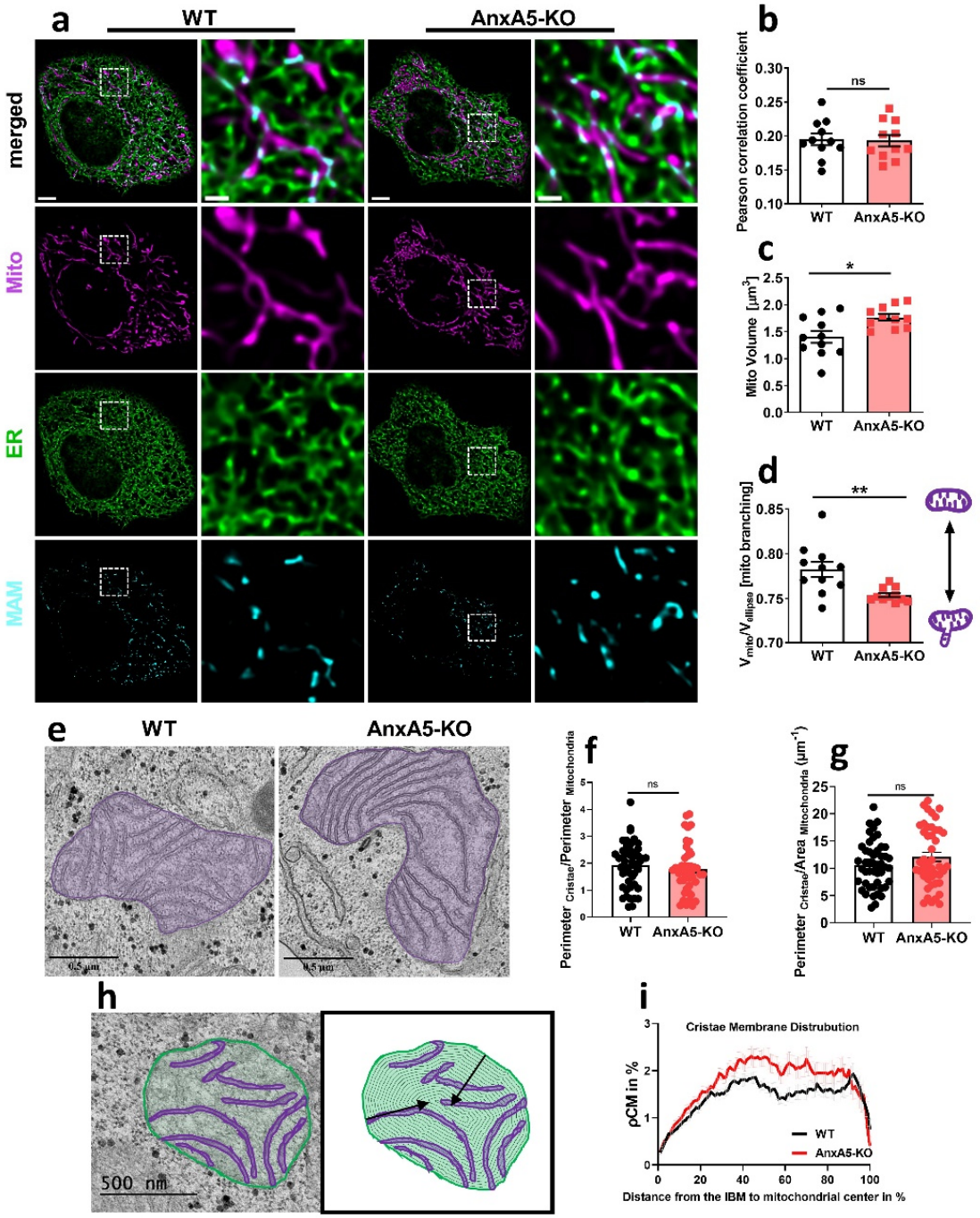

Figure 21. AnxA5-depleted cells do not alter ER-mitochondria contact sites but show more voluminous mitochondria. a Confocal images of WT and AnxA5-KO HeLa cells stained with MTR-CMX (magenta) and ERAT4.03 NA (green) were used to visualize MAM. Images include cell overviews (scale bar = 10 µm) and magnified regions (scale bar = 1 µm). **b** Bar graphs represent MAMs (Pearson's R-value), **c** mitochondrial volume, and **d** mitochondrial branching (lower value = more branching). Data points represent the mean ± SEM with sample sizes of WT = 91/11 and AnxA5-KO = 88/11. **e** TEM images of mitochondria in WT and AnxA5-KO HeLa cells, with mitochondria highlighted in magenta

(scale bar = 500 nm). **f** Bar graphs show the cristae membrane amount, calculated by normalizing the cristae perimeter to the mitochondrial perimeter, and **g** cristae density was calculated as cristae perimeter divided by mitochondrial area. **h** The schematic illustrates measuring cristae membrane density (ρCM) in segmented mitochondria using progressively downsized circular segments **i** Demonstrates ρCM distribution in both WT and AnxA5-KO cells, employing the techniques outlined in Figure **h**. The x-axis spans from 0 to 100, where 0 corresponds to the outermost mitochondrial shell and 100 signifies the mitochondrial center. Data points represent the mean ± SEM with sample sizes of WT = 44/3 and AnxA5-KO = 47/3. Significant differences were determined using the unpaired Student's t-test (* $p < 0.05$, ** $p < 0.01$, and "ns" for not significant). Figure is taken from my own publication (Oflaz et al, 2023) (84).

3.3.4 AnxA5 localizes both at the OMM and within mitochondria

AnxA5 has been previously reported to associate with mitochondria (93) and localize to cardiolipin-rich regions (94,95). Considering the observed reduction in the mitochondrial matrix Ca^{2+} in AnxA5-KO cells, our subsequent aim was to determine whether AnxA5 regulates matrix Ca^{2+} homeostasis at the OMM or the IMM. To investigate this query, we initially checked the cellular positioning of AnxA5 using a subcellular fractionation technique. We isolated crude mitochondrial fractions and subsequently purified the crude mitochondrial fraction using Percoll gradient centrifugation (107). The immunoblot findings indicated the presence of AnxA5 in both the cytosol and mitochondria (Figure 22a).

Subsequently, we treated pure mitochondrial fractions with proteinase K (PK) to specifically degrade proteins localized on the cytosolic side of the OMM. PK treatment was highly effective in eliminating the bands corresponding to HK1 in the pure mitochondrial fraction, with only a slight reduction in the bands corresponding to VDAC1 and Cyt-C observed (Figure 22a). Intriguingly, the application of PK resulted in the degradation of most of AnxA5, leaving a faint band, indicating the localization of AnxA5 within the mitochondria (Figure 22a). To further validate these findings, we utilized TEM to explore the subcellular distribution of immunogold-labeled AnxA5. Consistent with our Western blot results, we detected immunogold particles not only in the cytosol but also in the OMM and within the mitochondria (Figure 22b).

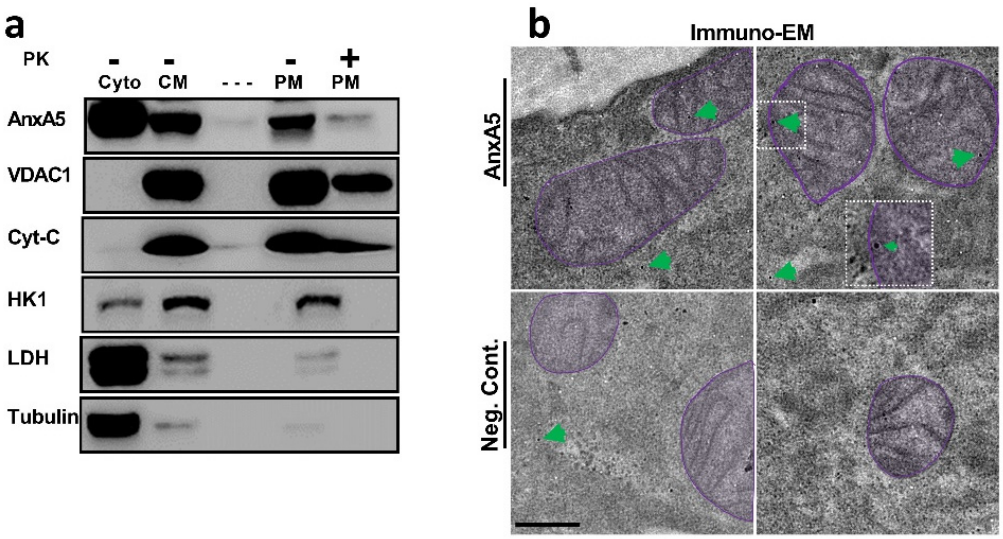

Figure 22. AnxA5 localizes on the OMM and within the mitochondria. a Immunoblot images display protein components in subcellular fractions: cytosol (Cyto), crude mitochondria (CM), and pure mitochondria (PM) from HeLa cells. To degrade cytosolic-facing OMM proteins, the pure mitochondrial fraction was incubated with 100 µg/ml Proteinase K (PK) for 30 minutes. **b** Exemplary immunoelectron micrographs of mitochondria-derived from HeLa cells. The upper panel shows AnxA5 localization through individual gold particles, while the lower panel serves as a negative control with the omission of the primary antibody. Magenta was used to highlight mitochondria while green arrows were used to show individual gold particles (scale bar = 250 nm). Figure is taken from my own publication (Oflaz et al, 2023) (84).

3.3.5 AnxA5 controls the IMS Ca^{2+} signaling upon IP_3-induced ER Ca^{2+} release

After confirming the localization of AnxA5 on the OMM and within the mitochondria, we aimed to investigate whether AnxA5 regulates mitochondrial Ca^{2+} signaling in the OMM or the IMM. To address this question, we employed a recently developed genetically encoded ratiometric Ca^{2+} sensor, specifically targeted to the IMS. Depletion of AnxA5 resulted in a significant reduction in IMS Ca^{2+} signaling in both HeLa (Figure 23a, b) and EA.hy926 cells (Figure 23c, d) upon IP_3-induced ER Ca^{2+} release. Moreover, the transient expression of AnxA5 in KO cells restored IMS Ca^{2+} signaling (Figure 23a, b. These results provide compelling evidence that AnxA5 actively regulates IMS Ca^{2+} signaling at the OMM.

Numerous studies reported that the mitochondrial Ca^{2+} uptake mechanism varies depending on the source of Ca^{2+} (52,117). To assess Ca^{2+} dynamics in the IMS, we employed a comprehensive protocol involving three different Ca^{2+} sources: 1) assessment of ER Ca^{2+} leakage by BHQ treatment; 2) IP_3-mediated Ca^{2+} release from the ER via histamine stimulation;

and 3) initiation of SOCE by reintroducing extracellular Ca^{2+} following depletion of Ca^{2+} stores in the ER (Figure 23e). The BHQ-induced ER- Ca^{2+} leakage resulted in a minor but comparable increase in IMS levels in both WT and AnxA5-depleted cells (Figure 23e, f). Subsequently, the elevation of IMS Ca^{2+} levels in response to IP_3-induced ER-Ca^{2+} release was significantly reduced in AnxA5-KO cells (Figure 23e, g). In contrast, the increase in IMS Ca^{2+} levels in response to SOCE displayed a similar elevation in both WT and KO cells (Figure 23e, h). These results imply that AnxA5 plays a distinct role in facilitating Ca^{2+} influx through the OMM upon IP_3-induced ER-Ca^{2+} release.

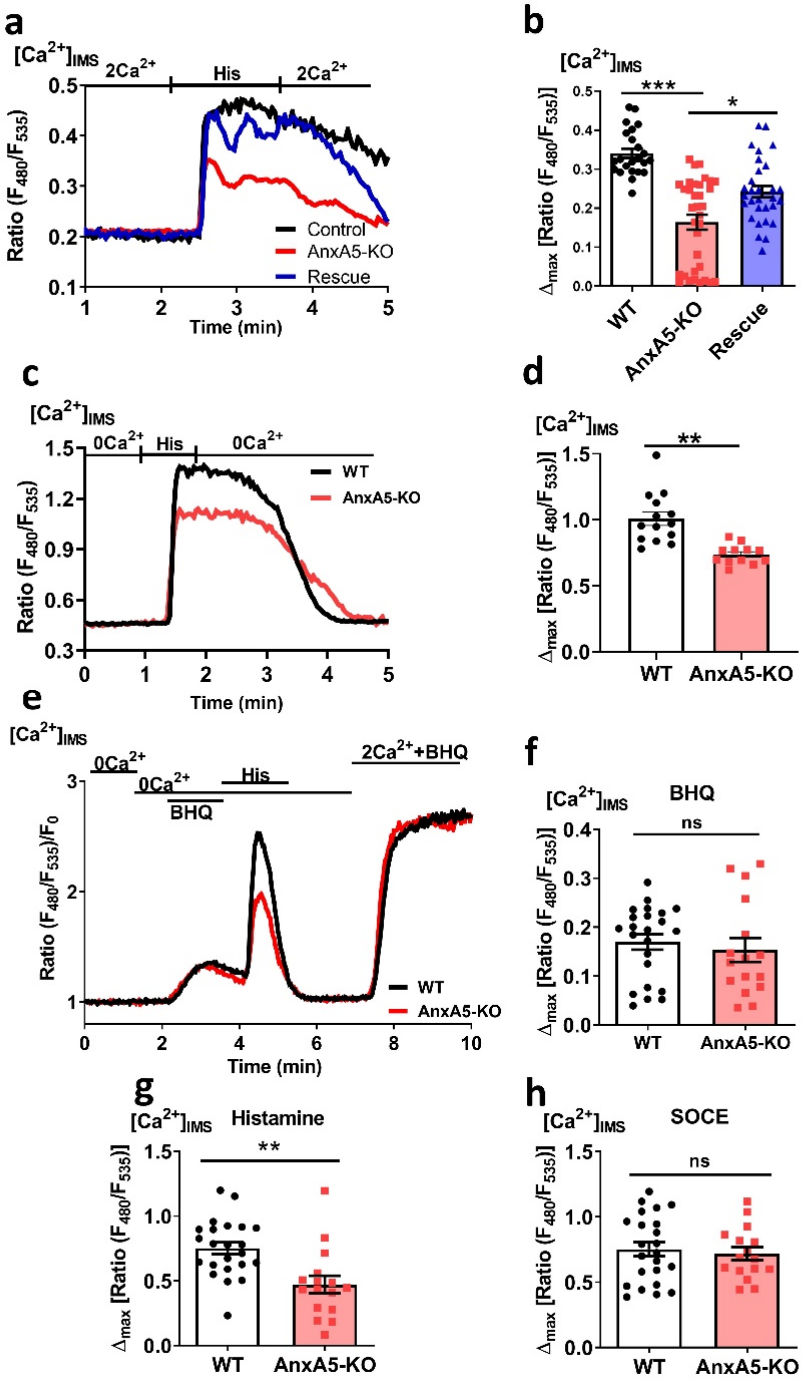

Figure 23. AnxA5 regulates IMS Ca^{2+} signaling depending on the source of the supplied Ca^{2+}. a Represenative traces of histamine-induced IMS Ca^{2+} responses in HeLa cells: WT (black), AnxA5-KO (red), and rescue (blue). **b** Bar graphs depict histamine-induced maximum IMS Ca^{2+} levels in WT (black), AnxA5-KO (red), and Rescue (blue). Data points represent the mean ± SEM with sample sizes of WT = 23/7, AnxA5-KO = 34/8, and Rescue = 30/9. **c** Represenative traces of histamine-induced IMS Ca^{2+} responses in EA.hy926 cells: WT (black) and AnxA5-KO (red). **d** Bar graphs depict histamine-induced maximum IMS Ca^{2+} levels in WT (black) and AnxA5-KO (red) cells. Data points indicate the mean ± SEM with sample sizes of WT = 14/6 and AnxA5-KO = 12/6. **e** Representative traces of BHQ and

histamine-induced IMS Ca^{2+} responses and SOCE in HeLa cells: WT (black) and AnxA5-KO (red). **f** Bar graphs display maximum IMS Ca^{2+} responses induced by BHQ, **g** histamine, and **h** SOCE in WT (black) and AnxA5-KO (red) cells. Data points represent the mean ± SEM with sample sizes of WT = 23/5 and AnxA5-KO = 16/4. Significant differences were determined by the unpaired Student's t-test (* $p < 0.05$, ** $p < 0.01$, *** $p < 0.001$, ns: not significant) (Oflaz et al, 2023). Figure is taken from my own publication (84).

After establishing AnxA5's role in IMS Ca^{2+} signaling triggered by IP_3-induced ER Ca^{2+} release, we investigated whether AnxA5's involvement in IMS Ca^{2+} signaling is contingent on a specific Ca^{2+} level. To achieve different levels of ER-Ca^{2+} release (low, medium, and high), we stimulated the cells with varying histamine concentrations including 1, 3, 10, 30, and 100 µM. AnxA5-KO cells showed reduced IMS Ca^{2+} elevation at all histamine concentrations in comparison to WT cells (Figure 24a). However, cytosolic Ca^{2+} levels were comparable between WT and AnxA5KO cells (Figure 24b). Subsequently, we generated concentration-response curves to analyze the impact of histamine on Ca^{2+} levels within both the IMS and cytosol in WT and KO cells. Notably, a significant distinction emerged in the half-maximal effective concentration (EC_{50}) for IMS Ca^{2+} signaling. In WT cells, the EC_{50} stood at 1.3 µM (with a range of 1-1.6 µM), while in AnxA5-KO cells, this value shifted notably to 4.8 µM (with a range of 2.7-7.8 µM) (Figure 24c). In contrast, the EC_{50} for cytosolic Ca^{2+} elevation exhibited consistency, remaining at 2 µM (with a range of 1.7-2.3 µM) in WT cells and 2 µM (with a range of 1.7-2.5 µM) in AnxA5-KO cells (Figure 24d).

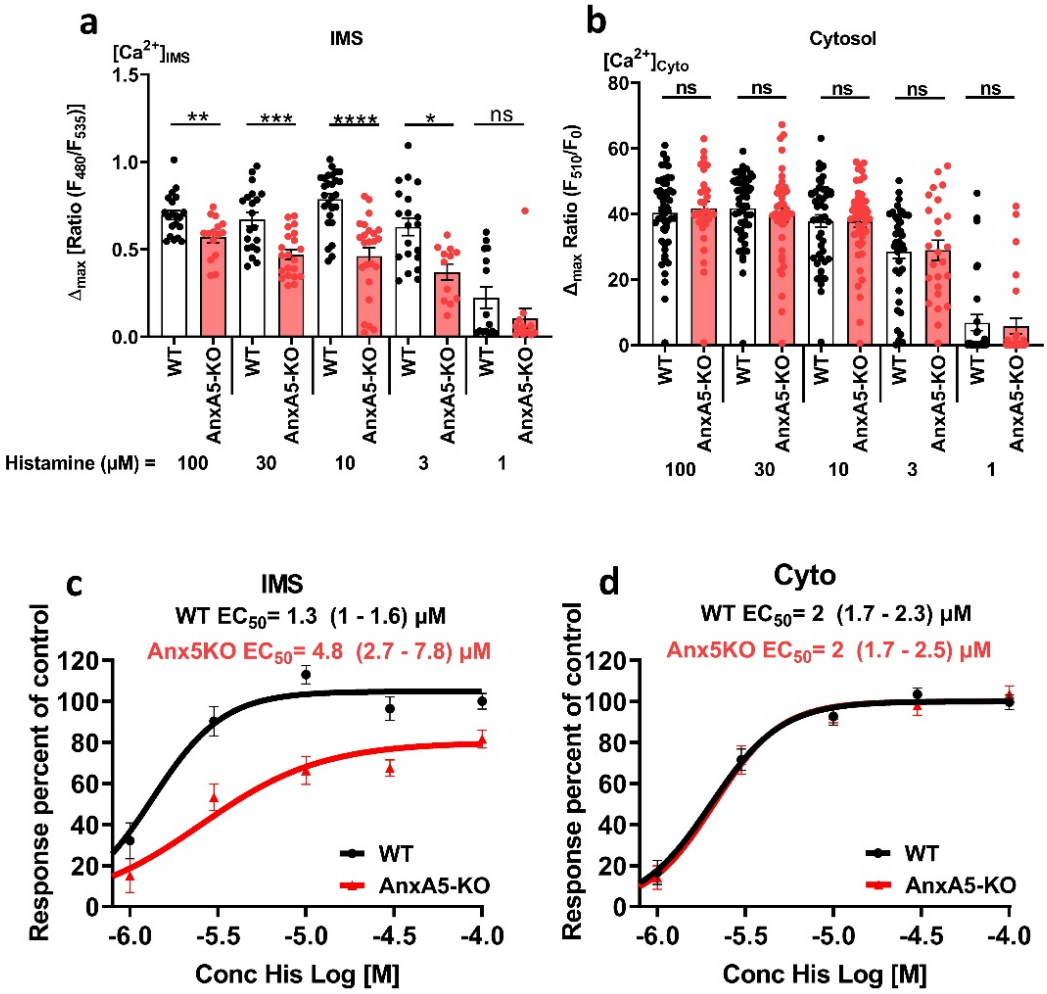

Figure 24. AnxA5 regulates IMS Ca^{2+} signaling in response to different concentrations of IP_3-generating agonists. a Bar graphs depict histamine-induced maximum IMS and **b** cytosolic Ca^{2+} levels in WT (black) and AnxA5-KO (red) cells. **c** Concentration-response curve of histamine (1-100 μM) for IMS Ca^{2+} and **d** cytosolic Ca^{2+} in WT (black) and AnxA5-KO (red) cells. Data points represent mean ± SEM for IMS and cytosol (In each condition, measurements were repeated on three different days, with a total sample size of 6). Significant differences were determined by the unpaired Student's t-test (* $p < 0.05$, ** $p < 0.01$, *** $p < 0.001$, **** $p < 0.0001$, ns: not significant) (Oflaz et al, 2023) (84).

3.3.6 AnxA5 actively influences the IMM dynamics through its modulation of IMS Ca^{2+} homeostasis.

Upon IP_3-induced Ca^{2+} release from the ER, these ions traverse VDAC1 in the OMM. Inside the IMS, Ca^{2+} binds to MICU1, initiating a structural change that disassembles its oligomer (118). To investigate the impact of AnxA5-mediated Ca^{2+} signaling on MICU1's structural rearrangements, we utilized the MICU1-FRET sensor (38) (Figure 25a). While ER Ca^{2+} release significantly reduced the MICU1-FRET ratio in WT cells (Figure 25b), in KO cells, this reduction

was less pronounced, indicating the role of AnxA5 in regulating MICU1 dimerization through the regulation of IMS Ca^{2+} signaling (Figure 25b, c).

In our previous study, we reported that the elevation of Ca^{2+} levels in the IMS activates the dimerization of MICU1, leading to the spatial opening of the cristae junction during ER Ca^{2+} release (41) (Figure 25d). Consequently, this cristae junction opening slows down the cristae membrane dynamics in the MAM region (42) (Figure 25d). To investigate cristae membrane dynamics in both WT and AnxA5-KO cells in MAM regions, we employed structured illumination microscopy. Upon IP_3-induced ER Ca^{2+} release, we observed a significant reduction in cristae membrane dynamics in the WT cells. Intriguingly, no such changes were observed in AnxA5-depleted cells (Figure 25e). Notably, when AnxA5 was transiently expressed in the KO cells, it resulted in effects similar to those seen in WT cells (Figure 25e). These findings indicate that AnxA5-mediated IMS-Ca^{2+} signaling regulates cristae and membrane dynamics in the MAMs. Furthermore, we wondered whether reduced cristae junction openings reduce cristae Ca^{2+} signaling in AnxA5KO cells. To address this, we employed a cristae-targeted ratiometric Ca^{2+} sensor (98). Our experiments revealed that ER Ca^{2+} release led to a significant decrease in cristae Ca^{2+} in AnxA5-KO cells compared to WT cells (Figure 25f, g).

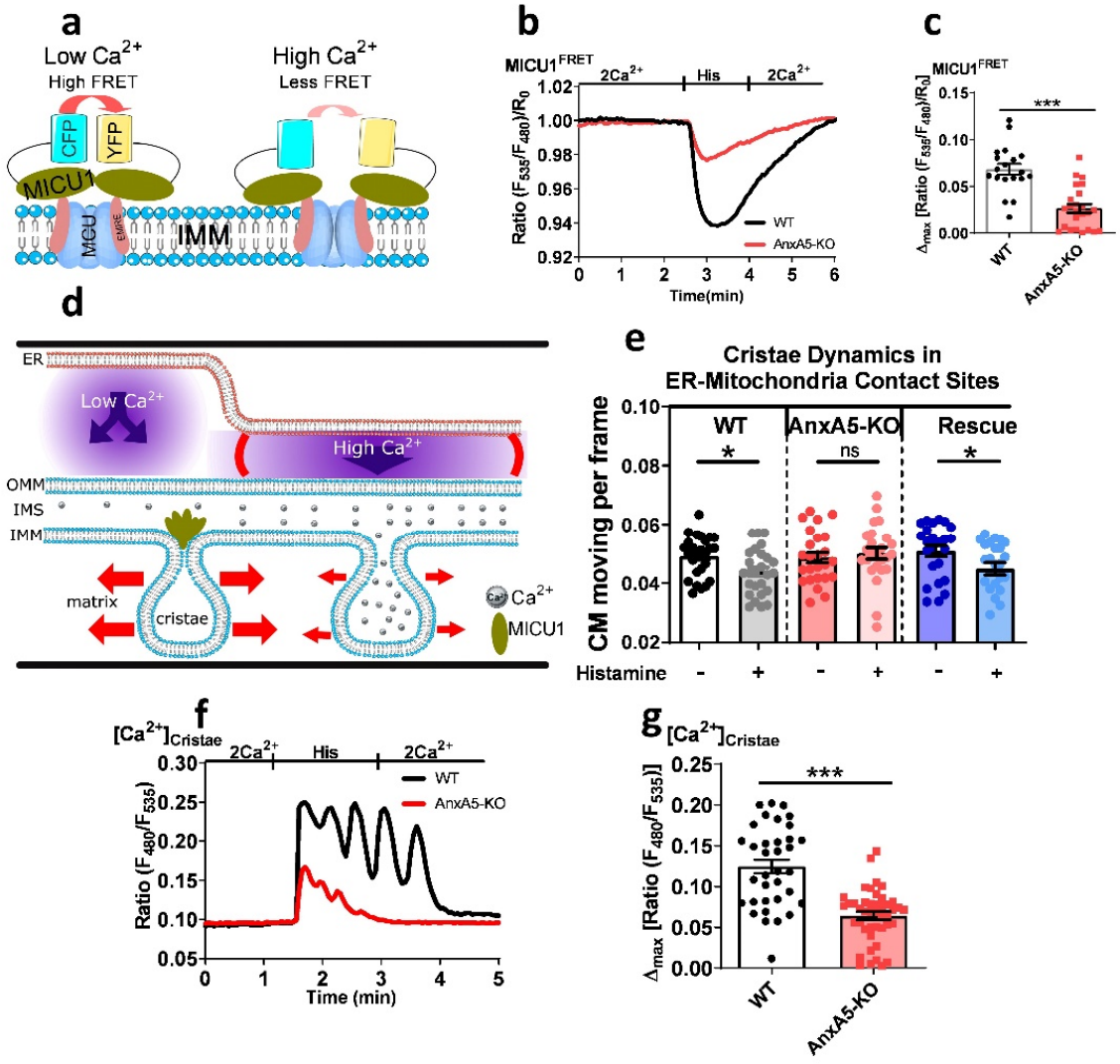

Figure 25. AnxA5 actively participates in the MICU1 rearrangement and cristae junction openings by facilitating the IMS Ca^{2+} signaling. a The schematic shows histamine-induced rearrangement of the MICU1-FRET construct. **b** Average traces of histamine-induced MICU1 FRET ratio in WT (black) and AnxA5-KO (red) cells. Bar graphs display histamine-induced MICU1 FRET ratio changes in WT (black) and AnxA5-KO (red) cells. Data points represent the mean ± SEM with sample sizes of WT = 19/6 and AnxA5-KO = 24/6. **d** The schematic shows cristae membrane dynamics under low and high Ca^{2+} conditions. **e** Bar graph depicts cristae membrane movements in MAM regions under basal and IP_3-induced ER Ca^{2+} release in WT (black), AnxA5-KO (red), and Rescue (blue). Data points represent the mean ± SEM with sample sizes of WT = 26/6, AnxA5-KO = 25/6, and Rescue = 24/6. **f** Average traces of histamine-induced cristae Ca^{2+} levels in WT (black) and AnxA5-KO (red) cells. **g** Bar graph displays maximum histamine-induced cristae Ca^{2+} levels in WT (black) and AnxA5-KO (red) cells. Data points represent the mean ± SEM with sample sizes of WT = 35/6 and AnxA5-KO = 44/6. Significant differences were determined by the unpaired Student's t-test (* $p < 0.05$, *** $p < 0.001$, ns: not significant). Figure is taken from my own publication (Oflaz et al, 2023) (84).

Previous studies demonstrated that histamine-induced openings of cristae junctions facilitate the relocation of the MCU from the cristae lumen to the IBM (39). To investigate the role of AnxA5 in MCU shuttling, we transfected the cells with MCU-mCherry (located in the IMM) and MICU1-YFP (located in the IBM) constructs (Figure 26a). In WT cells, the release of Ca^{2+} from the ER led to a significant translocation of MCU from the cristae lumen to the IBM, whereas this phenomenon did not occur in AnxA5-depleted cells (Figure 26b). Moreover, ER Ca^{2+} release resulted in a pronounced mitochondrial fragmentation in WT cells as shown by mitochondrial area and aspect ratio. Conversely, AnxA5-KO cells exhibited no change in the mitochondrial area and a slight decrease in aspect ratio after ER Ca^{2+} release (Figure 26c, d). These findings highlight the crucial role of AnxA5-mediated IMS Ca^{2+} signaling in orchestrating MCU repositioning and in modulating mitochondrial morphology during ER Ca^{2+} release.

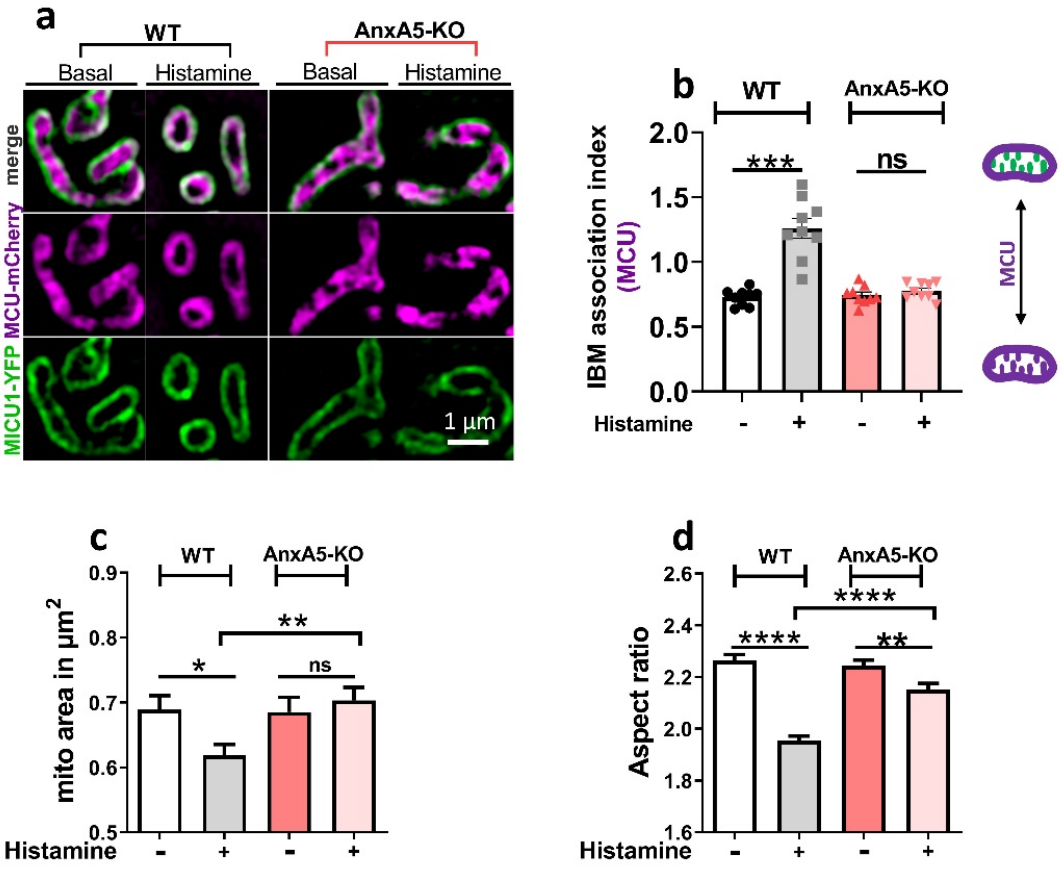

Figure 26. AnxA5 actively shapes the mitochondrial ultrastructure and dynamism of MCUc. a SIM images of HeLa cells show MICU1-YFP (green) and MCUmcherry (magenta) in WT (left) and AnxA5-KO (right) before and 90 seconds after ER Ca^{2+} release. **b** Bar graph displays MCU's IBM association index in WT and AnxA5-KO before and 90 seconds after ER Ca^{2+} release, indicating MCU translocation from cristae to IBM as per the schematic. **c** Bar graphs show mitochondrial area and **d** aspect ratio in WT and AnxA5-KO before and after ER Ca^{2+} release. Data points represent the mean ± SEM with

sample sizes of WT = 84/9 and AnxA5-KO = 88/9. Significant differences were determined using one-way ANOVA with Tukey's multiple comparison tests (*** $p < 0.001$, ns: not significant) or the unpaired Student's t-test (* $p < 0.05$, *** $p < 0.001$, *** $p < 0.0005$, ns: not significant). Figure is taken from my own publication (Oflaz et al, 2023) (84).

3.3.7 AnxA5 resides close to VDAC1 and accumulates in the OMM in response to ER Ca^{2+} release.

After demonstrating AnxA5's role in regulating IMS Ca^{2+} homeostasis, we proceeded to investigate its potential interaction or proximity to VDAC1. Initially, we used the co-immunoprecipitation (Co-IP) method; however, we did not detect a physical interaction between AnxA5 and VDAC1 (Figure 27a). Subsequently, we assessed their proximity using the proximity ligation assay (PLA), which allows us to visualize protein proximity, particularly when the proteins are within a distance of less than 30 nm (119). This method revealed PLA signals in WT cells, indicating a close association between AnxA5 and VDAC1 (Figure 27b, c). Conversely, AnxA5-KO cells showed minimal PLA signal (Figure 27b, c). Notably, siRNA-mediated depletion of VDAC1 resulted in a 70% decrease in PLA signals and a 60% reduction in protein expression level (Figure 27d). These results validate the methodology's specificity and credibility and support the conclusion that, in an unstimulated state, AnxA5 localizes near VDAC1.

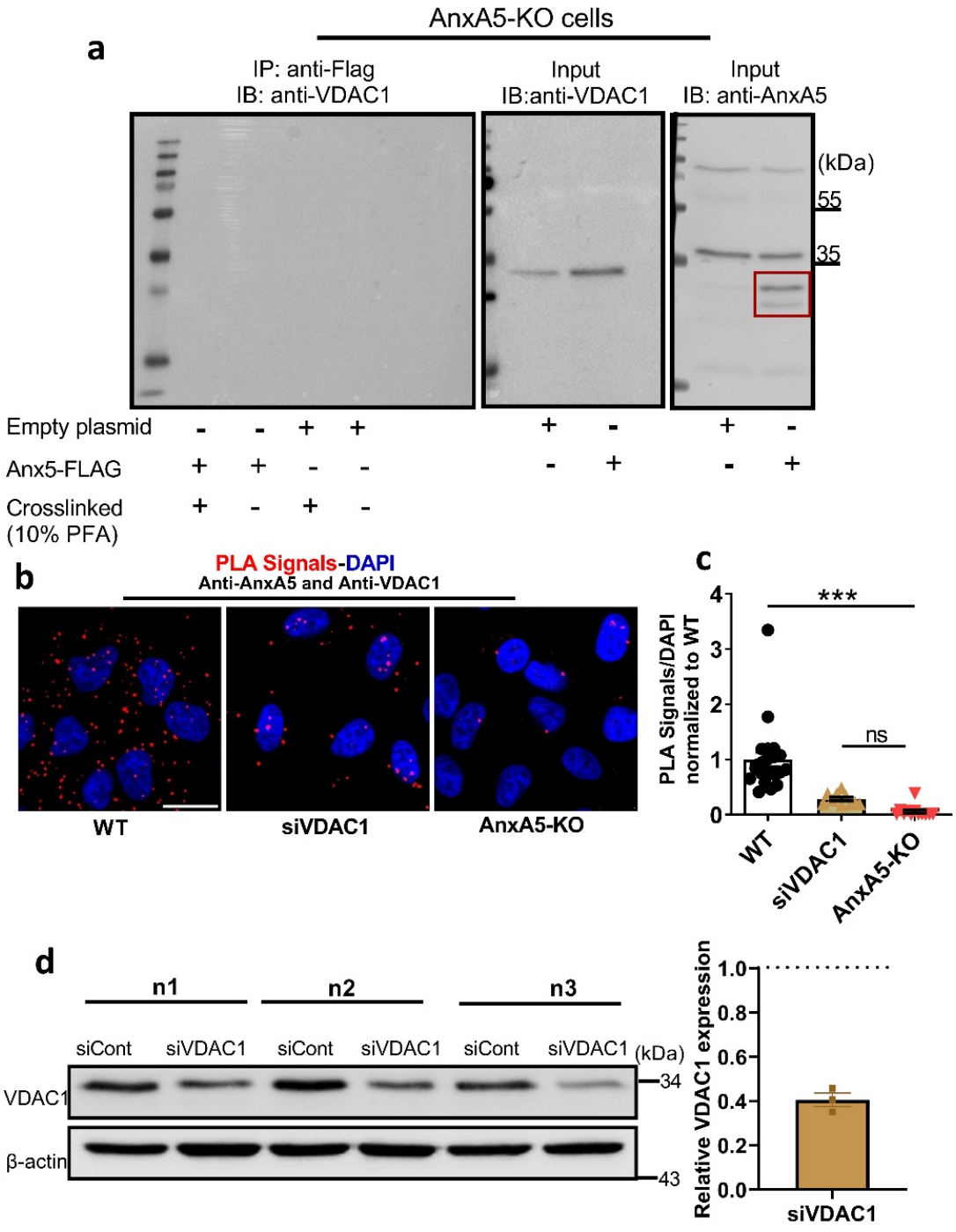

Figure 27. AnxA5 localizes in the vicinity of VDAC1. a Immunoblots show AnxA5-KO HeLa cells transfected with AnxA5-FLAG or empty plasmid, fixed with 10% PFA as described in methods. AnxA5 was immunoprecipitated from whole cell lysate using the FLAG tag, and co-immunoprecipitation of VDAC1 was confirmed by immunoblotting with a VDAC1 antibody. **b** Representative PLA assay image showing protein-protein proximity between AnxA5 and VDAC1 (scale bar = 10 µm). **c** The bar graph illustrates the ratio of total PLA signals to the number of cells. Data points indicate the mean ± SEM, with sample sizes of siNeg = 4, siVDAC1 = 3, and AnxA5-KO = 4. **d** The immunoblots display VDAC1

expression levels in cells transfected with either siNeg or siVDAC1. The bar graph represents immunoblot analysis of VDAC1 expression as mean ± SEM, with sample sizes of siControl = 3 and siVDAC1 = 3. Significant differences were determined using one-way ANOVA with Tukey's multiple comparison tests (*** $p < 0.001$, ns: not significant). Figure is taken from my own publication (Oflaz et al, 2023) (84).

AnxA5 functions as an intracellular Ca^{2+} sensor, detecting elevated Ca^{2+} and translocating to regions with heightened Ca^{2+} concentrations to bind to negatively charged PL (120). In light of this, our study sought to elucidate the role of ER Ca^{2+} release, which generates Ca^{2+} hotspots peaking at 16µM in the MAMs regions (16), in influencing the dynamic movement of AnxA5 towards mitochondria. To achieve this, we employed a cryo-fixation method together with immunogold labeling of AnxA5. This approach allowed us to monitor the subcellular localization of AnxA5 with TEM under both basal conditions and 20 seconds following ER Ca^{2+} release (Figure 28a). Immunogold particles were observed within both the mitochondria and the cytosol under basal conditions and after ER Ca^{2+} release (Figure 28a). Intriguingly, the release of ER-derived Ca^{2+} led to the accumulation of gold particles within a 20 nm proximity to the OMM from both cytosolic and IMS leaflets of the OMM (Figure 28a, b). Consequently, we propose a novel model in which the release of Ca^{2+} from the ER dynamically triggers the accumulation of AnxA5 to the OMM, potentially near VDAC1 (Figure 28c).

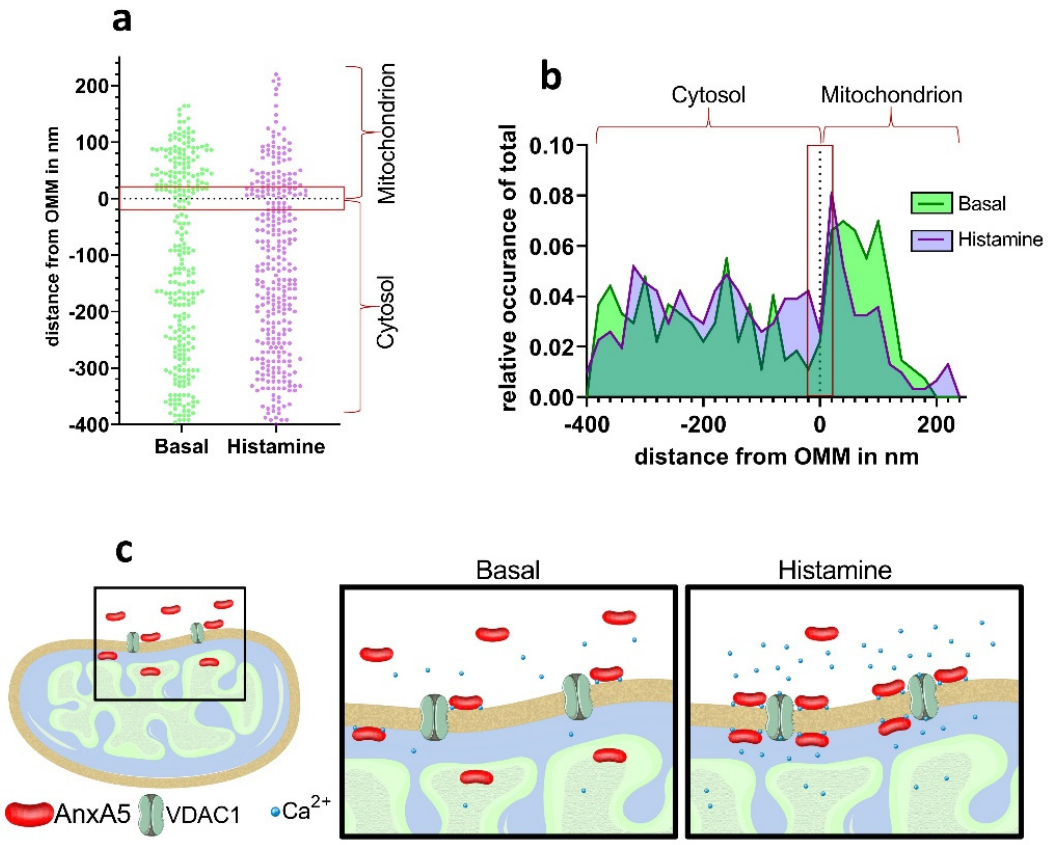

Figure 28. IP_3-induced ER Ca^{2+} release induces translocation of AnxA5 to the OMM. a AnxA5-labeled gold particle distribution in the entire cell, showing their presence on mitochondria and in the cytosol under basal (green) and 20-second post-histamine (magenta) stimulation. Positive values indicate gold particles are closer to the mitochondrial matrix side, while negative values indicate proximity to the cytosol from the OMM. **b** The relative occurrence of gold particles was calculated from panel **a**. Data points represent the subcellular localization of gold particles with sample sizes of WT-Basal = 10/3 and WT-Histamine = 10/3. c The schematic shows the basal localization and histamine-triggered translocation of AnxA5 to the OMM. Figure is taken from my own publication (Oflaz et al, 2023) (84).

3.3.8 AnxA5 modulates the open probability of an OMM channel

To gain deeper insights into whether the reduced IMS Ca^{2+} homeostasis observed in AnxA5-depleted cells is due to impaired Ca^{2+} permeability of the OMM, we conducted patch clamp experiments on intact mitochondria isolated from both WT and AnxA5-KO cells. Employing a voltage protocol involving stepwise hyperpolarization in 20 mV increments (ranging from -60 to -120 mV), we successfully identified the single-channel activity of the inward currents (Figure 29a). The recorded channels exhibited a single-channel conductance of 35 pS and demonstrated an increased single-channel opening probability (NPo) in response to varying

voltage conditions (Figure 29b). These recordings were conducted using a pipette solution containing 10 µM free Ca^{2+} and 140 mM K^{+} while, in the absence of Ca^{2+}, we did not observe single-channel activity within the same voltage range (Figure 29c).

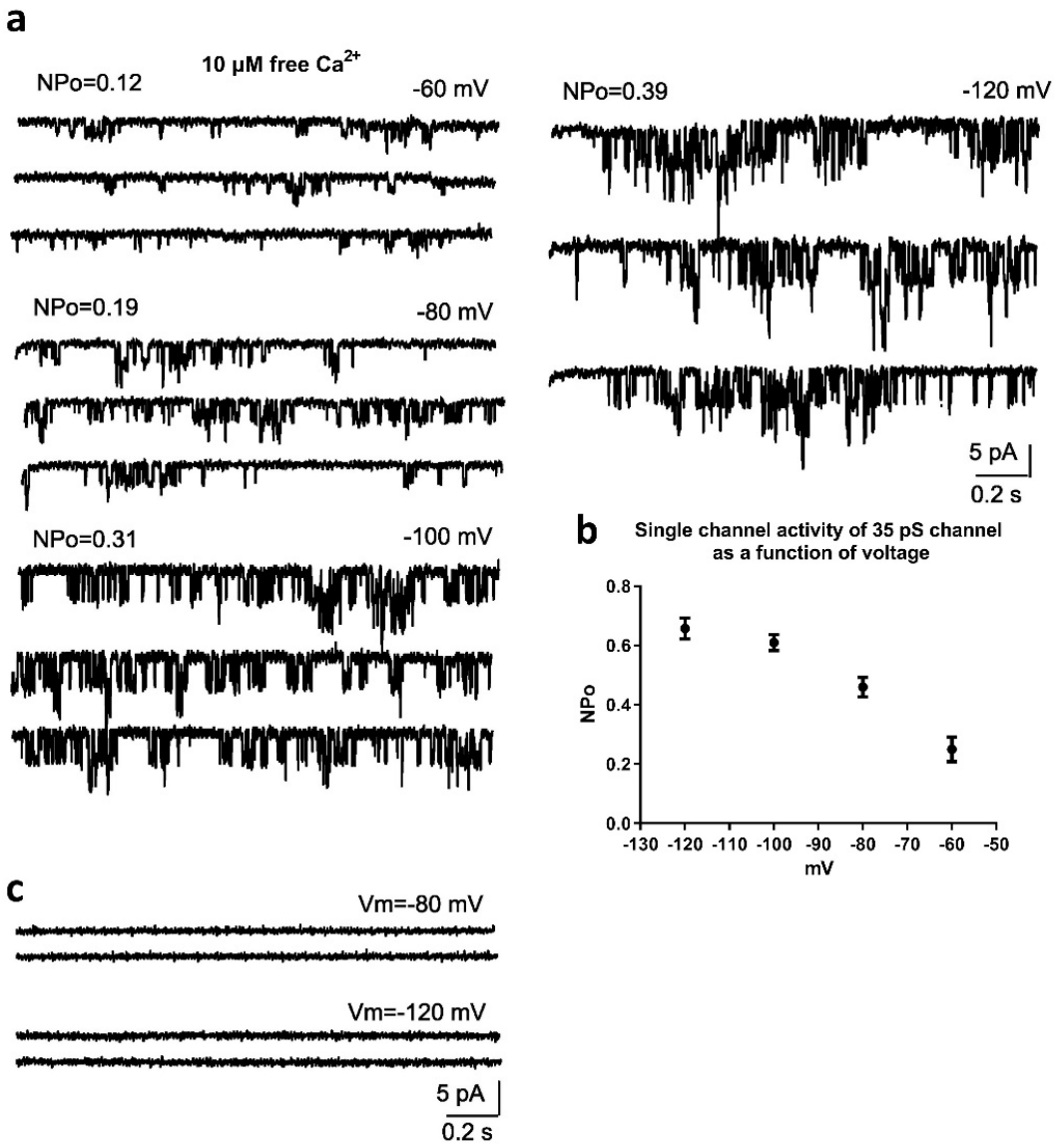

Figure 29. OMM harbors 35 pS single channel. a Representative single-channel traces of the 35 pS channel at different voltages in intact mitochondria isolated from WT HeLa cells. **b** The graph illustrates the average NPo of the 35 pS channel at different voltages. **c** Representative single-channel traces in the Ca^{2+}-free conditions demonstrate the absence of channel activity in intact mitochondria isolated from WT HeLa cells. Data points indicate the mean ± SEM with sample sizes of WT-60 = 3, WT-80 = 7, WT-100 = 7, and WT-120 = 10. Figure is taken from my own publication (Oflaz et al, 2023) (84).

Interestingly, we detected 35 pS channel activity in both WT and AnxA5-depleted cells (Figure 30a). To delve into the influence of AnxA5 on transmitochondrial Ca^{2+} fluxes, we conducted a

comparison of the mean NPo values at a test potential of -80 mV between mitochondria from WT and AnxA5-KO cells. Notably, the absence of AnxA5 resulted in a reduction in the mean NPo of the channel (Figure 30b). Collectively these results underscore the critical role of AnxA5 in regulating the Ca^{2+} permeablelity of the 35 pS channel in the OMM.

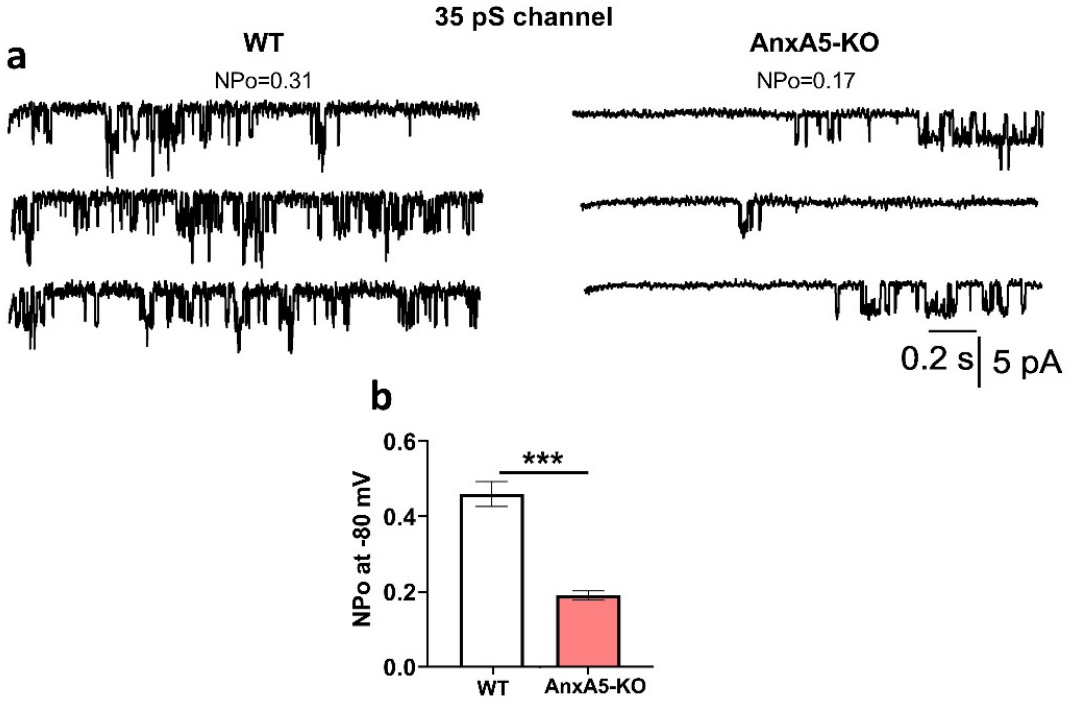

Figure 30. The impact of AnxA5 on the 35 pS conductance single-channel on the OMM. a Representative single-channel traces of the 35 pS channel in mitochondria from WT and AnxA5-KO HeLa cells, and **b** bar graphs showing NPo at -80 mV. Data points represent mean ± SEM with sample sizes of nWT = 7 and nAnxA5-KO = 4. Significant differences were determined by the unpaired Student's t-test (*** $p < 0.001$). Figure is taken from my own publication (Oflaz et al, 2023) (84).

3.3.9 Annexin 5-VDAC1 interaction serves as a protective mechanism, safeguarding against VDAC1 dimerization during cisplatin-induced cell death

Multiple research investigations have established that various factors leading to cell apoptosis can trigger a rise in intracellular Ca^{2+} levels in HeLa cells (104,121). Particularly noteworthy is the finding that cisplatin effectively induces the movement of Ca^{2+} from the ER toward the mitochondria (122,123). To examine how cisplatin affects Ca^{2+} levels within specific subcellular compartments, we measured the levels of Ca^{2+} within the mitochondria and cytosol. Consequently, following 12 hours of treatment with cisplatin at concentrations of 5 and 10 µM, we observed a substantial increase in matrix and IMS Ca^{2+} levels in WT HeLa cells (Figure

31a, b). However, this effect was not observed in AnxA5KO cells (Figure 31a, b). Furthermore, cisplatin treatment resulted in a slight, comparable increase in cytosolic Ca^{2+} concentration in both WT and AnxA5-depleted cells (Figure 31c), Collectively these results suggest that cisplatin-induced Ca^{2+} mobilization is directed to mitochondria in WT but not in KO cells. Following that, we investigated how elevated mitochondrial Ca^{2+} levels affect cell viability and apoptosis. To do so, we employed flow cytometry. Cisplatin treatment resulted in enhanced apoptotic cell death in AnxA5KO cells compared to WT in a concentration-dependent manner (Figure 31d, e). These results imply that although AnxA5KO cells display resistance to cisplatin-triggered mitochondrial Ca^{2+} overload, they demonstrate an increased susceptibility to apoptosis.

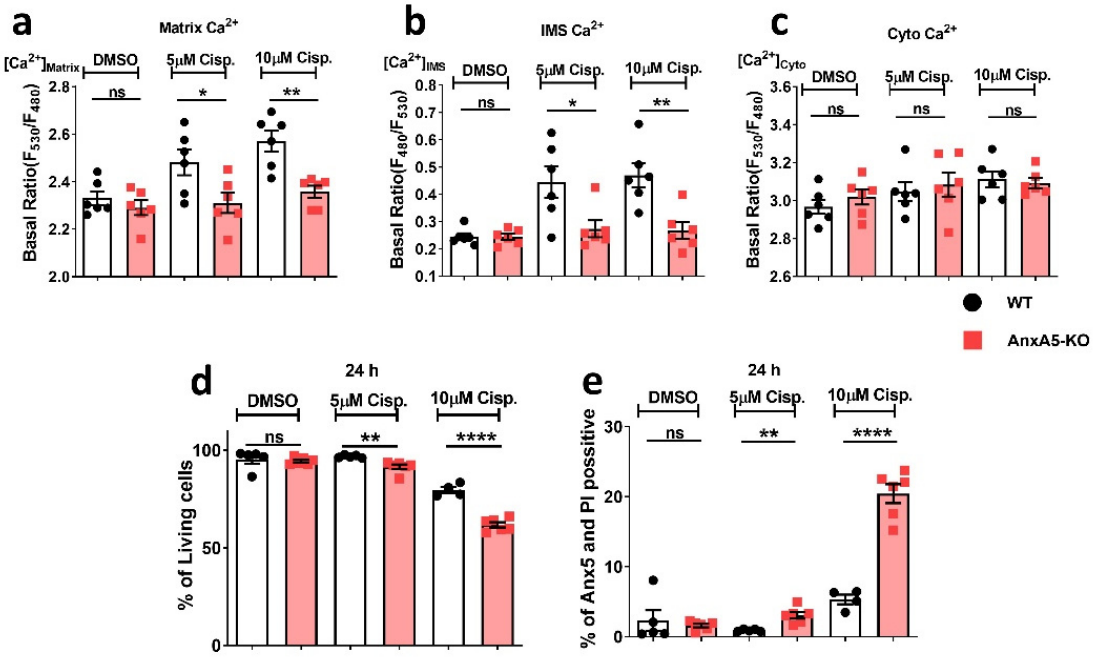

Figure 31. AnxA5 prevents cisplatin-induced mitochondrial Ca^{2+} overload yet exhibits enhanced sensitivity to apoptosis. a Bar graphs depict basal Ca^{2+} levels in the matrix, **b** IMS, **c,** and cytosol of WT (black) and AnxA5-KO (red) cells upon 12 h DMSO, 5 µM, and 10 µM cisplatin treatment. Data points represent mean ± SEM (data collected from 6 wells over 3 days). **d** Bar graphs show cell viability and **e** late apoptosis (Annexin5-FITC/PI staining) in WT (black) and AnxA5-KO (red) cells after 24 h of DMSO, 5 µM, and 10 µM cisplatin treatment. Data points represent mean ± SEM (data collected from 6 wells over 3 days). Significant differences were determined by the unpaired Student's t-test (* $p < 0.05$, ** $p < 0.01$, **** $p < 0.0001$, ns: not significant). Figure is taken from my own publication (Oflaz et al, 2023) (84).

Apoptotic signals induce the formation of VDAC1 oligomers, a process associated with mitochondria-mediated apoptosis (78). However, the prevention of VDAC1 oligomerization

using a novel compound called VBIT-4 has been shown to protect cells from undergoing apoptosis (78). To explore whether the heightened vulnerability of AnxA5-depleted cells to cisplatin treatment is influenced by VDAC1 oligomerization, we exposed the cells to cisplatin in the presence or absence of VBIT-4. Consistent with our prior experiments, treatment with cisplatin resulted in a significant decrease in cell viability of AnxA5KO cells (Figure 32a, b). However, co-treatment with cisplatin and VBIT-4 prevented apoptotic cell death in both WT and AnxA5-depleted cells (Figure 32a, b). These results suggest that the susceptibility of KO cells to cisplatin-induced cell death relies on the formation of VDAC1 oligomers induced by cisplatin.

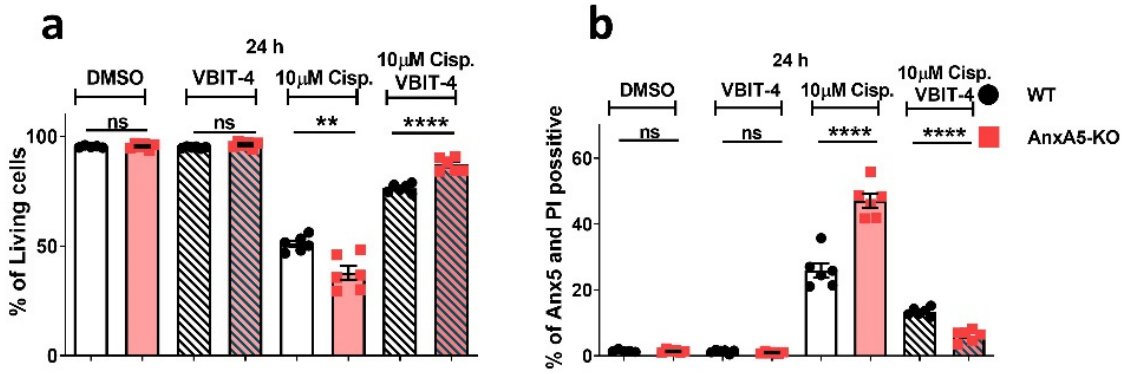

Figure 32. Inhibition of VDAC1 oligomerization rescues the mitochondrial-mediated apoptosis. a Bar graphs show cell viability and **b** late apoptosis in WT (black) and AnxA5-KO (red) cells after 24 h of DMSO, 20 μM VBIT-4, 10 μM cisplatin, and cisplatin+VBIT-4 treatments. Data points represent mean ± SEM (data collected from 6 wells over 3 days). Significant differences were assessed using the unpaired Student's t-test (** $p < 0.01$, **** $p < 0.0001$, and ns: not significant). Figure is taken from my own publication (Oflaz et al, 2023) (84).

Subsequently, we carried out cross-linking and immunoblotting assays to investigate possible variations in cisplatin-triggered VDAC1 oligomerization between WT and AnxA5-depleted cells. In their unstimulated state, we observed dimeric VDAC1, with a 3.2-fold increase in WT cells and a 5.2-fold increase in AnxA5KO cells after 24 hours of cisplatin treatment (Figure 33a, b). When we treated the cells with cisplatin for 48 hours, we observed an 8.4-fold increase in WT cells and a 9.9-fold increase in AnxA5-depleted cells in the dimeric status of VDAC1 indicating that cisplatin treatment induces a higher oligomeric level of VDAC1 in AnxA5-depleted cells (Figure 33c, d). Notably, the concurrent application of cisplatin and VBIT-4 prevented the formation of VDAC1 oligomers in both WT and KO cells (Figure 33a-d).

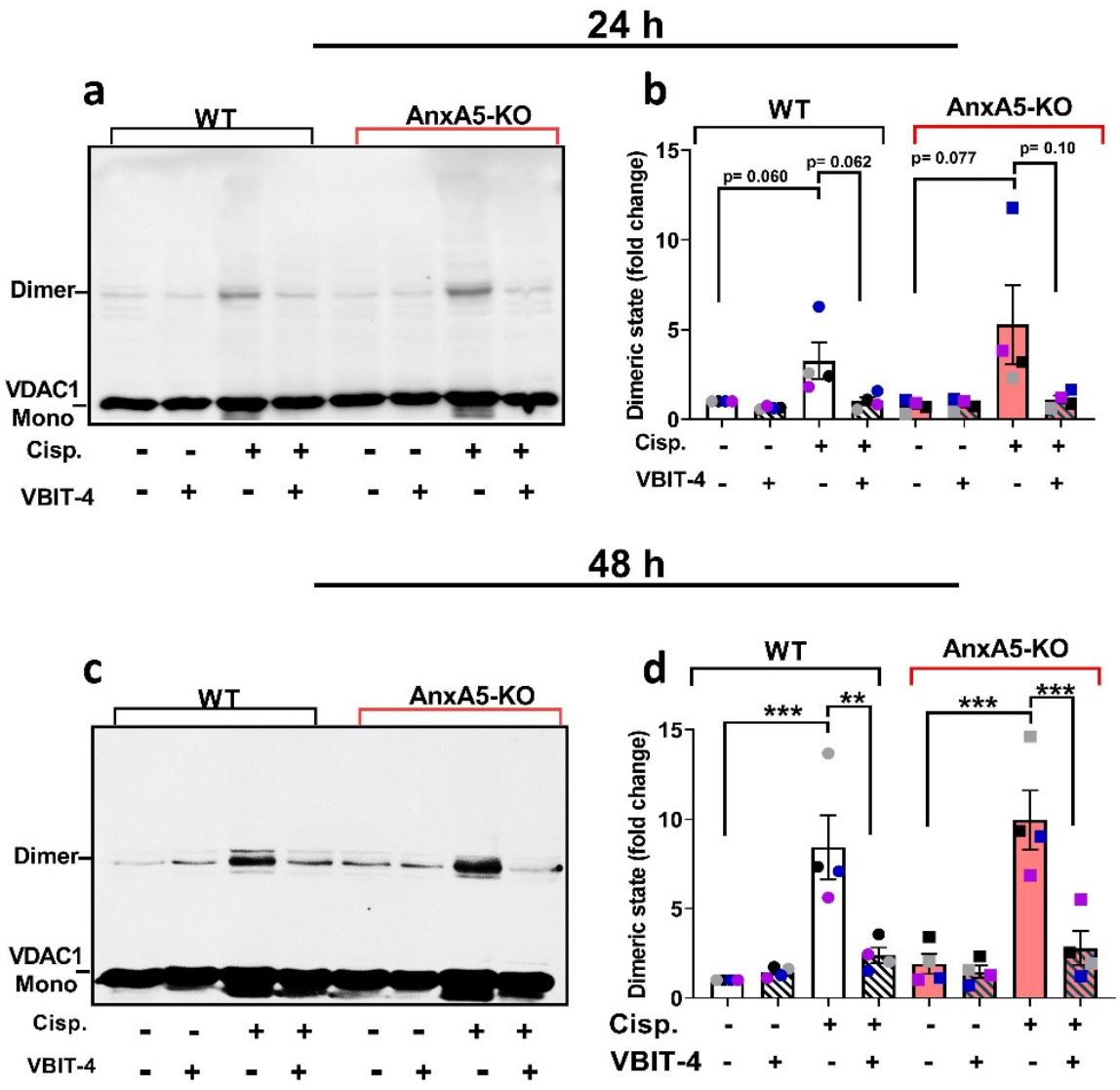

Figure 33. Cisplatin induces more VDAC1 dimerization in AnxA5-depleted cells. a Immunoblot displays VDAC1 monomers and dimers. **b** Bar graph quantifies immunoblot results in WT (black) and AnxA5-KO (red) cells after 24-hour treatments: DMSO, 20 μM VBIT-4, 10 μM cisplatin, and cisplatin+VBIT-4 (colors represent experiments from the same day). Data is presented as Mean ± SEM, with 4 samples for both WT and AnxA5-KO. **c** Immunoblot displays VDAC1 monomers and dimers. **d** Bar graph quantifies immunoblot results in WT (black) and AnxA5-KO (red) cells after 48-hour treatments: DMSO, 20 μM VBIT-4, 10 μM cisplatin, and cisplatin+VBIT-4 (colors represent experiments from the same day). Data is presented as Mean ± SEM, with 4 samples for both WT and AnxA5-KO. Statistical significance was determined using one-way ANOVA with Tukey's multiple comparison tests (** $p < 0.01$ and *** $p < 0.001$). Figure is taken from my own publication (Oflaz et al, 2023) (84).

Furthermore, as an alternative approach, we transiently introduced tetracysteine-tagged VDAC1 into both WT and AnxA5-depleted cells. Next, we visualized the cells 12 hours after cisplatin treatment and the cotreatment with cisplatin+VBIT-4 (Figure 34a). We noted the

existence of clustered VDAC1 in both WT and AnxA5-depleted cells, even when cisplatin treatment was not administered (Figure 34a). In line with our western blot experiments, cisplatin prompted the development of more extensive VDAC1 clusters in AnxA5-KO cells, whereas the inclusion of VBIT-4 resulted in a decrease in the size of these clusters (Figure 34a, b). These findings collectively underscore that AnxA5 localized close to the VDAC1 microenvironment acts as a protective barrier, regulating the extent of cisplatin-induced VDAC1 dimerization.

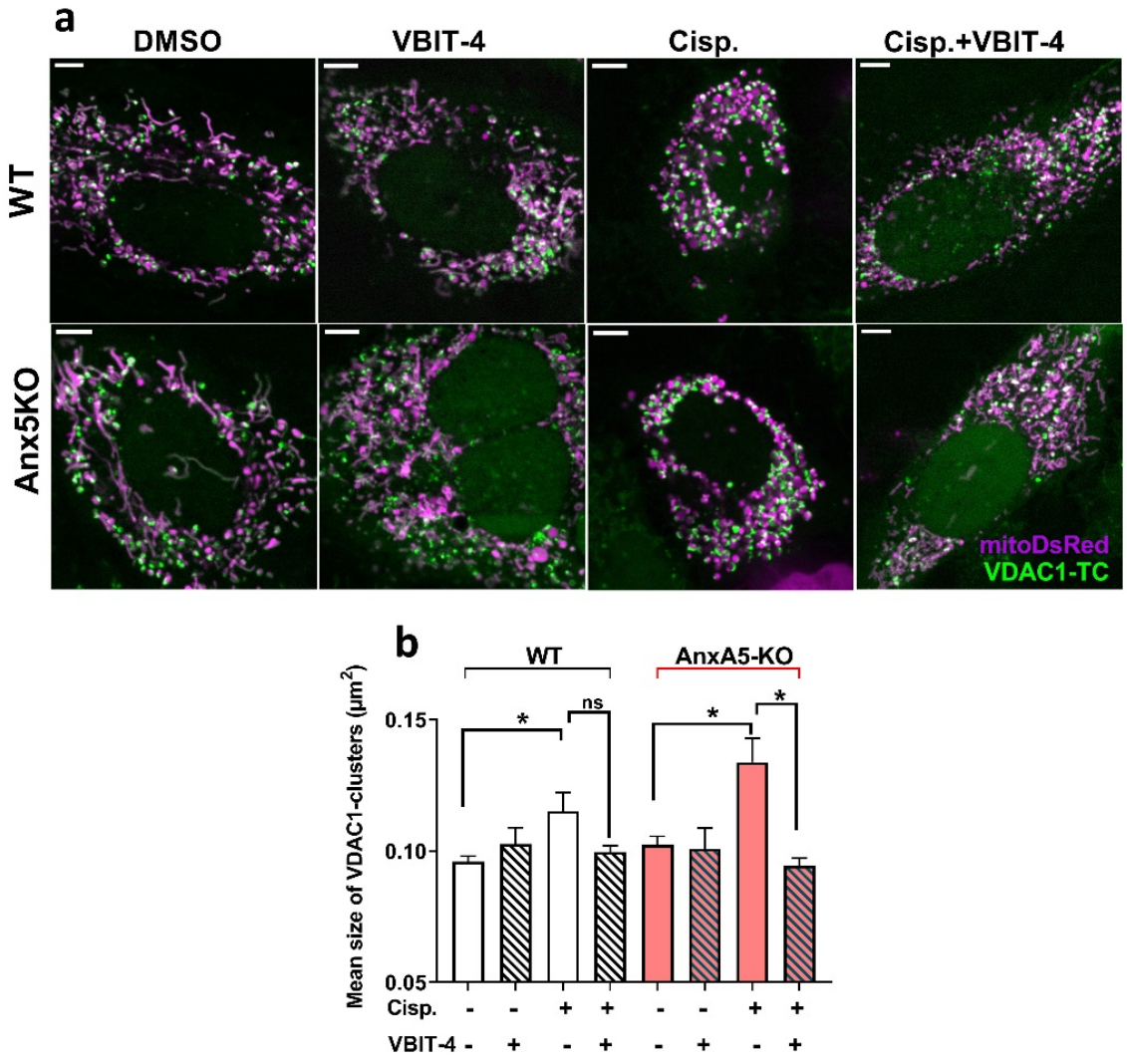

Figure 34. Cisplatin treatment induces enhanced VDAC1 clusters in AnxA5-depleted cells. a Representative confocal images of WT and AnxA5-KO HeLa cells with VDAC1-TC (green) and mitoDsRed (red). **b** Bar graph quantifies VDAC1 cluster size (μm²) in WT (black) and AnxA5-KO (red) cells after 12-hour treatments: DMSO, 20 μM VBIT-4, 10 μM cisplatin, and cisplatin+VBIT-4. The data is presented as the mean ± SEM, with sample sizes as follows: WT-DMSO = 7, WT-VBIT-4 = 6, WT-cisp. = 8, WT-cisp.+VBIT-4 = 3, AnxA5-KO-DMSO = 7, AnxA5-KO-VBIT-4 = 6, AnxA5-KO-cisp. = 8,

AnxA5-KO-cisp.+VBIT-4 = 3. Statistical significance was evaluated using one-way ANOVA with Tukey's multiple comparison tests (* $p < 0.05$, ns: not significant). Figure is taken from my own publication (Oflaz et al, 2023) (84).

4 Discussion

4.1 General Outlook

During my PhD studies, I conducted an extensive investigation into intracellular Ca^{2+} signaling, the regulation of Ca^{2+} signaling on transcription factors (10), mitochondrial Ca^{2+} homeostasis (84), and bioenergetics (9). In my first publication (Oflaz et al., 2021) (10), we discovered that the near-UV light, commonly employed for cytosolic Ca^{2+} measurements with Fura2-AM, induces intracellular ROS production in pancreatic β-cells which in turn activates the L-type Ca^{2+} channel, initiating cytosolic Ca^{2+} oscillations. While Near-UV light immediately induced ROS production at the beginning of the experiments, cytosolic Ca^{2+} oscillations started approximately 8 minutes later, indicating that a specific ROS threshold was necessary to trigger the activation of the L-type Ca^{2+} channels. To discern whether ROS or ROS-induced Ca^{2+} oscillations regulate the nuclear migration of NFATc3, we tagged mitochondria to the subplasmalemal region to buffer Ca^{2+} oscillations while maintaining the same ROS production (10). This experiment revealed that near UV-induced cytosolic Ca^{2+} oscillations were the driving force behind the nuclear migration of NFATc3, but not the ROS itself. This study highlights the dynamic synchronization between the nuclear translocation of NFATc3 and the Ca^{2+} ions, shedding light on the potential side effects of near-UV light exposure in the context of single-cell measurements.

The role of Ca^{2+} in mitochondrial energy metabolism has been extensively studied by our group and others (11,59,124). However, how S1R contributes to this process has remained elusive. In my second publication (Oflaz & Koshenov. 2022) (9), we delve into the role of S1R in cancer cell energy metabolism across its basal, activated, and inhibited states. Our findings revealed that S1R activation by its ligand enhances mitochondrial bioenergetics by boosting ER-to-mitochondria Ca^{2+} flux while reducing their reliance on aerobic glycolysis. Intriguingly, our research suggests that under basal conditions, S1R does not significantly impact mitochondrial bioenergetics, as antagonizing or downregulating S1R does not affect these processes. Our study underscores the multifaceted role of S1R and highlights the potential use of S1R ligands to modulate cancer cell energy metabolism (9).

In my latest research (Oflaz et al., 2023, under review) (84), we have unveiled the indispensable role of AnxA5 in mitochondrial Ca^{2+} homeostasis upon ER Ca^{2+} release. We showed the dynamic translocation of AnxA5 to the OMM following ER Ca^{2+} release. The wide range of sub-mitochondrial targeted sensors developed in our lab has allowed us to discern

that AnxA5 specifically participates in IMS Ca^{2+} signaling. We have also discovered that by localizing in the vicinity of VDAC1, AnxA5 regulates the Ca^{2+} permeability of VDAC1. Furthermore, we revealed that AnxA5KO cells are resistant to cisplatin-induced mitochondrial Ca^{2+} overload while exhibiting enhanced sensitivity to apoptosis. Moreover, our further efforts have shown that by localizing close to VDAC1, AnxA5 regulates the oligomerization of VDAC1, thereby controlling apoptotic cell death during cisplatin treatment.

In summary, during my PhD journey, I investigated intracellular Ca^{2+} signaling, specifically AnxA5's contribution to mitochondrial Ca^{2+} homeostasis and apoptotic responses during cisplatin exposure (84). I also studied the role of S1R in mitochondrial bioenergetics in cancer cells (9) and the impact of cytosolic Ca^{2+} oscillations on nuclear migration of NFATc3 (10). In the subsequent subsections of the discussion, I have individually discussed the key findings and contributions of my three papers.

4.1.1 Near UV-induced ROS production activates L-type Ca^{2+} oscillation to fire nuclear migration of NFATc3

Among various NFAT members, NFATc3 is highly expressed in pancreatic B-cell lines and regulates cell proliferation and insulin secretion (125). During our investigation into the dynamic translocation of NFATc3 to the nucleus, we observed a two-phase translocation process. In the first phase, nuclear migration of NFATc3 is initiated by IP_3-induced ER Ca^{2+} release while In the second phase, sustained Ca^{2+} oscillations generated by the near-UV induced activation of the L-type Ca^{2+} channels re-initiate the nuclear migration of NFATc3. The removal of the IP_3-generating agonist resulted in the restoration of cytosolic Ca^{2+} levels to their basal state during the initial phase, subsequently prompting the nuclear export of NFATc3 while starting from min 10 repetitive Ca^{2+} oscillations led to a rapid nuclear migration of NFATc3. These results align with previously reported findings that in comparison to other NFATs, NFATc3 exhibits a remarkable level of dynamism and reversibility in nuclear migration, indicating the highly dynamic nature of Ca^{2+}-dependent nuclear translocation of NFATc3 (18,22,126).

Prior research highlighted the significant role of the L-type Ca^{2+} channel in facilitating repetitive Ca^{2+} oscillations in pancreatic β-cells (125). Our experiments with the L-type Ca^{2+} channel inhibitor, verapamil, not only decreased the number of Ca^{2+} oscillations during the second phase but also reduced NFATc3 translocation. However, during the first phase, verapamil treatment didn't affect either the CCh-induced ER Ca^{2+} release or NFATc3 translocation. This suggests that the L-type Ca^{2+} channel isn't involved in the initial phase of NFATc3 translocation and doesn't contribute to IP_3-induced Ca^{2+} signaling. Instead, ER Ca^{2+} release and the influx

of Ca^{2+} through calcium release-activated channels (CRAC channels), triggered by the initial ER Ca^{2+} release, are the primary factors maintaining the first phase of NFATc3 translocation.

Previous studies have shown that in INS-1 cells, cytosolic Ca^{2+} oscillations depend on membrane potential changes and can be triggered by ATP production (125). When ATP binds to ATP-sensitive potassium channels, it leads to membrane depolarization, which activates the L-type Ca^{2+} channel (127). We questioned whether the Ca^{2+} oscillations in the second phase were a result of enhanced ATP production following the ER Ca^{2+} release in the first phase. Remarkably, inhibition of the mitochondrial ATP production diminished Ca^{2+} oscillations and NFATc3 translocation in the second phase, while the first phase remained unaffected (Figure 6). This outcome led us to formulate a hypothesis: during the first phase, ER Ca^{2+} release enhances mitochondrial ATP production, causing membrane depolarization, and consequently, the activation of Ca^{2+} oscillations through the L-type Ca^{2+} channel. However, a control experiment in which cells were perfused without CCh stimulation for 20 minutes, yielded surprising results. After approximately 10 minutes, cytosolic Ca^{2+} oscillations started and induced NFATc3 translocation. This observation indicated that the second phase of Ca^{2+} oscillations does not rely on ER Ca^{2+} release triggered ATP production in the first phase (Figure 7). However, the precise mechanism underlying the ATP dependency of near-UV light-induced Ca^{2+} oscillation and NFATc3 translocation remains unclear and needs further investigation.

To further understand the reason behind the second-phase oscillations we considered whether exposure to near-UV light (405nm wavelength) used during Fura2-AM measurements might induce the oscillations. Notably, we observed a substantial reduction in the number of Ca^{2+} oscillations, decreasing from 20 to 10, with NFATc3 remaining within the cytosol when we used another Ca^{2+} dye called Fluo-4 which is excited with 488 nm (Figure 7). Our further investigations involving the use of verapamil revealed that the source of UV-induced cytosolic Ca^{2+} oscillations was indeed the L-type Ca^{2+} channel. Intriguingly, inhibiting the L-type Ca^{2+} channel reduced the number of Ca^{2+} oscillations from 20 to 10. Similarly, when we used Fluo-4, we still observed 10 oscillations regardless of verapamil treatment (Figure 7). These results indicate that the L-type Ca^{2+} channel does not solely contribute to cytosolic Ca^{2+} oscillations under basal conditions. Furthermore, the Ca^{2+} oscillations in the absence of UV light failed to activate NFATc3 translocation suggesting that repetitive and localized Ca^{2+} entry through the L-type Ca^{2+} channel is responsible for the nuclear migration of NFATc3 rather than global Ca^{2+} oscillations. In this line, it has been previously demonstrated that calmodulin interacts with the L-type Ca^{2+} channel, and local Ca^{2+} elevations in the vicinity of the L-type Ca^{2+} channel activate nuclear migration of the NFATc3 (128).

To investigate the mechanisms by which UV light activates the L-type Ca^{2+} channel and triggers NFATc3 translocation, we conducted further investigations. Previous studies have suggested that an overproduction of ROS modulates the activity of the L-type Ca^{2+} channel (108). To investigate whether the imaging parameters we employed induced ROS production, we conducted additional experiments. By using recently developed ultra-sensitive cytosolic and mitochondrial ROS sensors (129), we observed exponential ROS production both in the cytosol and within the mitochondria (Figure 7). Remarkably, in most of our Fura2-AM experiments, cytosolic Ca^{2+} oscillations initiated around the 7th minute (Figure 6). This observation suggests that a certain level of ROS production is required for the activation of the L-type Ca^{2+} channel, which subsequently triggers NFATc3 translocation. Intriguingly, prior research has indicated that moderate ROS levels can enhance β-cell proliferation (130). NFATc3 translocating to the nucleus increases the expression of genes responsible for cell proliferation (131). Therefore, it's tempting to speculate that cells maintain a specific ROS balance to use it as a second messenger to activate transcription factors through the activation of L-type Ca^{2+} channels. This intricate interplay between ROS, Ca^{2+} channels, and transcription factors underscores the synchronization of cellular signaling pathways in regulating essential processes like cell proliferation.

Our data demonstrate that ROS scavenging with NAC not only abolishes NFATc3 translocation but also reduces cytosolic Ca^{2+} oscillations (Figure 8). These compelling findings provide further support for our hypothesis that UV-induced ROS production is responsible for cytosolic Ca^{2+} oscillations, subsequently driving NFATc3 translocation into the nucleus. However, we do not yet know whether near-UV light generates ROS in the cytosol, mitochondria, or a combination of both. NAC can scavenge ROS both in the cytosol and the mitochondria, thus it does not answer the question of whether it is mitochondrial or cytosolic ROS that plays the primary role. It would be interesting to specifically scavenge ROS within the mitochondria using mitochondrial ROS scavengers to pinpoint the source of the ROS. Previous studies have elegantly shown that mitochondria-derived ROS do not penetrate the OMM (dynamic experiments were recorded for 8 min) (129). Therefore, it is tempting to speculate that cytosolic but not mitochondrial ROS production is responsible for the activation of L-type Ca^{2+} channels.

After confirming that ROS triggers repetitive cytosolic Ca^{2+} oscillations through the activation of L-type Ca^{2+} channels, which subsequently facilitate the translocation of NFATc3 to the nucleus, our objective was to differentiate between the direct influence of ROS and the impact of ROS-induced cytosolic Ca^{2+} oscillations on NFATc3 translocation. To address this, we formulated a hypothesis: if we buffer Ca^{2+} oscillations while maintaining the same ROS levels,

we would observe diminished NFATc3 translocation and Ca^{2+} oscillations. To experimentally test this notion, we manipulated the positioning of mitochondria to the sub-plasma membrane region by using the AKAP-RFP-CAAX construct (128) to locally buffer Ca^{2+} oscillations in the vicinity of the L-type Ca^{2+} channel. Notably, cells expressing AKAP-RFP-CAAX exhibited a reduction in the number of Ca^{2+} oscillations and prevented nuclear translocation of NFATc3 (Figure 9). Importantly, the ROS production remained unchanged under similar conditions (Figure 10). These findings provide robust evidence in favor of our hypothesis, suggesting that the crucial factor for NFATc3 translocation to the nucleus is the cytosolic Ca^{2+} oscillation induced by ROS, rather than ROS itself. To further support this finding, we suppressed MCU protein expression in AKAP-RFP-CAAX-expressing cells to reduce mitochondrial Ca^{2+} uptake and buffering ability. This resulted in the restoration of cytosolic Ca^{2+} oscillation and the re-establishment of NFATc3 translocation to the nucleus. In a recent study, it was noted that approximately 18% of the sub-plasma membrane region is taken up by mitochondria in β-cells (132). Despite the knockdown of MCU, UV light-induced Ca^{2+} oscillation and NFATc3 translocation remained unaffected (Figure 9). This could be attributed to the free motility of mitochondria located in the sub-plasma membrane region. Consistent with this, a prior investigation revealed that Ca^{2+} entry via L-type Ca^{2+} channels notably reduces the portion of mitochondria residing in the sub-plasma membrane area, decreasing it from 18% to 13% in MIN6 cells (132). Therefore, it is intriguing to consider that in WT or siMCU-treated cells, mitochondria positioned beneath the plasma membrane may have a constrained ability to dampen UV light-triggered Ca^{2+} oscillations due to the influence of Ca^{2+} on mitochondrial motility and repositioning.

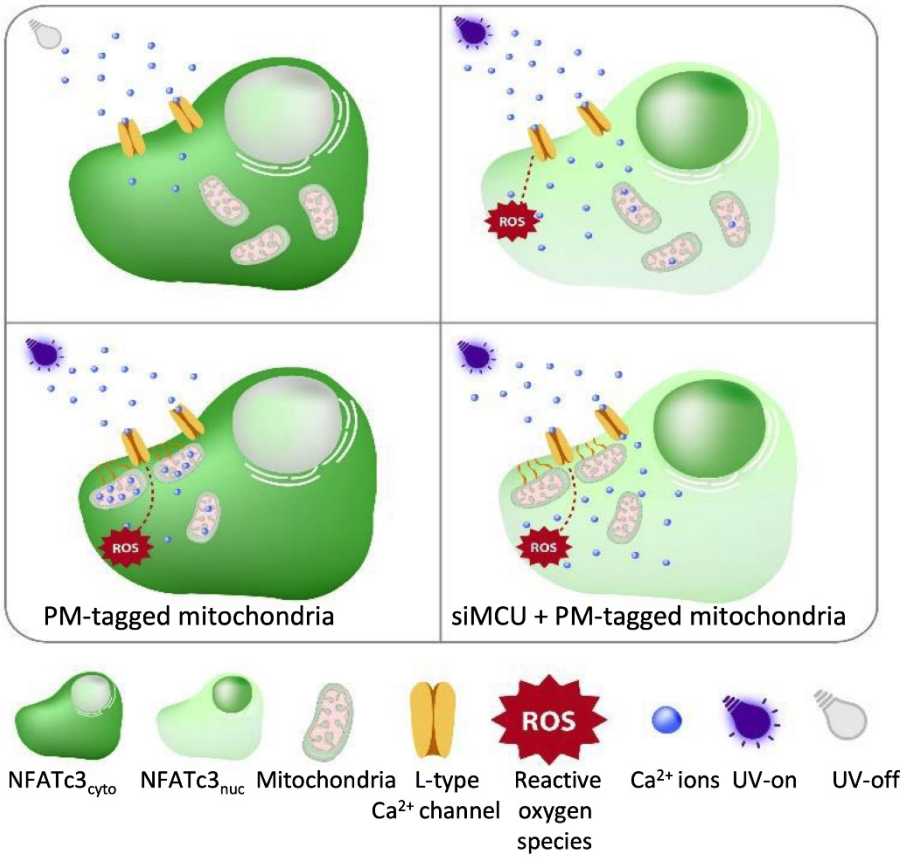

Figure 35. Schematic illustration of the near-UV light-induced Ca^{2+} oscillation mechanism and its influence on NFATc3 nuclear migration. Under basal conditions, NFATc3 localized in the cytosol (upper right panel). Near-UV exposure generates ROS, triggering cytosolic Ca^{2+} oscillations through L-type Ca^{2+} channels. Repetitive Ca^{2+} oscillations fire NFATc3 translocation to the nucleus (upper right panel). Mitochondria, tagged to the plasma membrane, buffer locally generated Ca^{2+} oscillations by L-type Ca^{2+} channels, leading to the attenuation of Ca^{2+} oscillations and NFATc3 translocation (lower left panel). Downregulating MCU in plasma membrane-tagged mitochondria diminishes their capacity to buffer Ca^{2+} oscillations, consequently restoring cytosolic Ca^{2+} oscillations and facilitating NFATc3 migration to the nucleus (lower right panel). Figure is taken from my own publication (Oflaz et al. 2021) (10).

In summary, our findings unveiled that ROS generation triggered by 405 nm laser light results in cytosolic Ca^{2+} oscillations through the activation of L-type Ca^{2+} channels, facilitating the nuclear migration of the NFATc3. Furthermore, we introduced the concept of mitochondria acting as efficient local Ca^{2+} buffers when anchored to the cell membrane, thereby mitigating cytosolic Ca^{2+} oscillations induced by L-type Ca2+ channels and subsequent NFATc3 translocation. Moreover, our research highlights the heightened sensitivity of pancreatic β-cells to commonly utilized near-UV light wavelengths in the context of live-cell imaging applications.

4.1.2 Sigma1 Receptor activations enhance mitochondrial bioenergetics in cancer cells

Cancer cells are known for their ability to reprogram their metabolism to support uncontrolled proliferation and survival (11,59). While anticancer treatments target cancer energy metabolism, there is still a need for a deeper understanding to develop more effective treatment strategies. In our study, we investigated how S1R influences cancer energy metabolism, aiming to understand its role in basal, activated, and inactivated states. To accomplish this, we selected two distinct cancer cell lines characterized by varying S1R expression levels. Subsequently, we treated these cells with the S1R agonist (+)-SKF10047 or antagonist BD1047 and closely monitored changes in their energy metabolism dynamics. Through these approaches, we revealed the role of S1R in cancer energy metabolism during its basal, activated, and inactivated states.

In this study, we conducted real-time measurements of mitochondrial ATP production, mitochondrial Ca^{2+} homeostasis, Ψm, and the cytosolic pyruvate-to-lactate ratio to investigate the effects of S1R activation and antagonism in two distinct cell models: S1R-expressing A549 cells and non-expressing MCF7 cells (Figure 10). Our findings revealed that activating S1R with its agonist boosts OXPHOS and decreases their reliance on aerobic glycolysis in S1R-expressing A549 cells, as well as in transiently S1R-overexpressing MCF7 cells (Figure 12). This suggests that S1R activation profoundly influences cancer cell energy metabolism, making them more dependent on OXPHOS. Moreover, neither the S1R antagonist nor depletion of S1R had an impact on mitochondrial ATP production or Ψm in A549 cells (Figure 12). Supporting these findings, transient overexpression of S1R in MCF7 cells did not affect mitochondrial ATP production unless treated with the S1R agonist (Figure 12). Therefore, our findings underscore that under resting conditions, S1R does not significantly contribute to mitochondrial bioenergetics, suggesting that under basal conditions, S1R may be dormant. This aligns with our earlier research indicating that in an unstimulated state, S1R remains inactive and does not contribute to mitochondrial bioenergetics (73).

In our prior study, we established that S1R boosts mitochondrial bioenergetics at the onset of ER stress by promoting the leakage of ER Ca^{2+} toward the mitochondria (73). Given the known association between ER stress and S1R activation, we hypothesized that S1R remains dormant under basal conditions, and its activation enhances the Ca^{2+} transfer from the ER to the mitochondria, thereby enhancing the activity of matrix-residing dehydrogenases. In our experiments, the application of an S1R agonist resulted in a substantial elevation of basal mitochondrial Ca^{2+} levels and elevated mitochondrial Ca^{2+} uptake upon IP_3-induced ER Ca^{2+}

release in A549 cells (Figure 14). Notably, these changes occurred without any impact on cytosolic Ca^{2+} levels (Figure 15). Conversely, depleting S1R in A549 cells had no impact on mitochondrial and cytosolic Ca^{2+} levels, indicating that S1R does not significantly contribute to either mitochondrial or cytosolic Ca^{2+} levels in its dormant state (Figure 14, 15). However, upon activation, it enhances ER-to-mitochondria Ca^{2+} flux. This suggests that the increase in mitochondrial Ca^{2+} levels is likely responsible for the enhancement of OXPHOS. Moreover, treatment with an S1R agonist, exclusively elevated basal mitochondrial Ca^{2+} levels in transiently S1R-expressing MCF7 cells but did not affect mitochondrial Ca^{2+} uptake upon IP_3-induced ER Ca^{2+} release. This leads us to speculate that the basal elevation of mitochondrial Ca^{2+} levels facilitated by directed ER-to-mitochondria Ca2+ flux may be sufficient to enhance mitochondrial bioenergetics. This speculation is in line with our previous findings, which demonstrated that mitochondrial basal Ca^{2+} levels regulate cellular energy metabolism (11).

Our findings of S1R activation enhancing mitochondrial Ca^{2+} levels in cancer cells are supported by previous research showing that S1R activation through its agonist leads to the interaction of S1R with IP_3 receptors, resulting in effective Ca^{2+} delivery to the mitochondria (72). Additionally, the activation of S1R boosts IP_3-triggered ER Ca^{2+} release in neuroblastoma cell lines by interfering with the interaction between the adaptor protein Ankyrin and IP_3R. Our findings align with these previous studies and contribute a novel molecular mechanism by which S1R activation influences mitochondrial bioenergetics via enhanced Ca^{2+} delivery to mitochondria, shifting cellular energy metabolism from glycolysis to OXPHOS.

The question of whether S1R remains inactive under basal conditions remains elusive. Our observations produced varying outcomes when we either administered the S1R antagonist or conducted experiments involving S1R knockdown. Remarkably, neither the S1R antagonist nor S1R knockdown had any influence on mitochondrial bioenergetics, a phenomenon that can be attributed to the unchanged levels of mitochondrial Ca2+. In contrast to our findings, previous research has reported that in unstimulated states S1R stabilizes IP_3Rs for effective Ca^{2+} delivery to the mitochondria. However, it's important to note that this conclusion was based on data showing reduced mitochondrial Ca^{2+} uptake in S1R-depleted cells upon consecutive stimulation with IP_3-generating agonists, while the initial stimulation showed no effect (72). Hence, it is not unexpected, based on our experiments, that S1R knockdown did not produce any discernible effect on the initial ER Ca^{2+} release. Additionally, the reduction in the pyruvate-to-lactate ratio in cells treated with S1R antagonists or subjected to S1R knockdown implies the presence of S1R activity at baseline. However, further research is needed to fully elucidate the underlying mechanism in this specific case.

In summary, our findings unveil a crucial role for pharmacological activation of S1R in enhancing the ER-mitochondria Ca^{2+} flux. This enhancement significantly augments the mitochondrial bioenergetics of cancer cells while concurrently reducing their dependence on aerobic glycolysis as an energy source.

4.1.3 AnxA5 is essential for VDAC1-dependent mitochondrial Ca^{2+} signaling and plays a critical role in regulating apoptotic cell death

Earlier research has presented findings that support the role of AnxA5 in regulating intracellular Ca^{2+} levels (85,133). However, the complete role of AnxA5 in the maintenance of Ca^{2+} homeostasis remains unclear. To investigate the role of AnxA5 in intracellular Ca^{2+} signaling, we conducted dynamic monitoring of sub-mitochondrial and cytosolic Ca^{2+} signaling both under basal conditions and upon IP_3-induced ER Ca^{2+} release. Our study revealed that AnxA5 regulates the VDAC1's Ca^{2+} permeability upon ER Ca^{2+} release, thereby contributing to mitochondrial IMS Ca^{2+} homeostasis. We demonstrated the essential role of AnxA5 in mitochondrial Ca^{2+} homeostasis in three different cell lines, including cells isolated from AnxA5KO mice. Furthermore, we found that AnxA5's localization in the vicinity of VDAC1 regulates VDAC1's oligomeric level in response to cisplatin treatment.

Our real-time tracking of mitochondrial matrix Ca^{2+} levels has unveiled the vital contribution of AnxA5 to the maintenance of mitochondrial Ca^{2+} balance in response to IP_3-induced ER Ca^{2+} release. Our findings demonstrate the localization of AnxA5 both on the OMM and within the mitochondria under basal conditions, while ER Ca^{2+} release leads to the accumulation of AnxA5 on the OMM (Figure 28). Notably, the elevated Ca^{2+} microdomains, which can reach up to 16 µM within the MAMs regions, seem to have the capacity to trigger the dynamic association of AnxA5 with the OMM in this specific area.

In contrast to prior findings suggesting AnxA7's involvement in the regulation of ER Ca^{2+} signaling in the brain (134), our investigation of both ER and cytosolic Ca^{2+} dynamics unequivocally establishes that AnxA5 does not contribute to ER Ca^{2+} release or re-uptake (Figure 18). Previous studies have also implicated AnxA6 as a regulator of mitochondrial fission processes (135). Consequently, in AnxA6 knockout cells, researchers observed fragmented mitochondria, reduced Ψmito, and disruptions in mitochondrial Ca^{2+} signaling. However, our research findings diverge from these observations, indicating that AnxA5 knockout cells maintain normal Ψmito and exhibit a more branched and voluminous mitochondrial morphology (Figure 20).

We have discovered that AnxA5 plays a specific role in modulating Ca^{2+} flux across the OMM, thereby directly influencing IMS Ca^{2+} signaling and mitochondrial architecture. Our lab previously showed that elevated IMS Ca^{2+} levels regulate mitochondrial morphology by inducing MICU1 dimerization, which, in turn, leads to the opening of cristae junctions and induces mitochondrial fission (42). Our results show that in AnxA5-depleted cells, both MICU1 rearrangements and cristae junction openings are hampered, underscoring the pivotal role of AnxA5 in controlling IMS Ca^{2+} homeostasis thereby participating in the dynamic modeling of mitochondrial morphology. Therefore IP_3-induced ER Ca^{2+} release triggers mitochondrial fission in WT cells, but not in AnxA5-depleted cells (Figure 24). These findings provide insight into the increased size and branching of mitochondria seen in AnxA5KO cells, as well as the clustering of cristae in the center of the mitochondria.

In our patch-clamp experiments performed at the OMM of isolated intact mitochondria, we identified a Ca^{2+} channel with a conductance of 35 pS (Figure 29, 30). It's noteworthy that we did not detect the high-conductance single-channel activity reported in earlier studies involving reconstituted VDAC1 in artificial lipid bilayers or vesicles (12). VDAC-mediated ion fluxes have been extensively studied, characterizing VDAC as a high-conductance channel with reported conductances ranging from 680 pS to 4 nS (12). Nevertheless, the lack of high-conductance single channels in our findings aligns with earlier research that identified a 30 pS channel in freshly isolated intact mitochondria under conditions similar to ours. (136). These controversial findings may be attributed to differences in experimental approaches between the two models. In lipid bilayer experiments, isolated VDAC1 is reconstituted within lipid-containing bilayers. In contrast, in isolated mitochondria, the OMM remains intact, preserving interaction partners of VDAC1 and maintaining a distinct lipid microenvironment. Considering the reported influence of lipid compositions and protein interactions on VDAC1 conductance, the conductance of VDAC1 may differ between freshly isolated mitochondria and its reconstitution in artificially generated liposomes (27,29,137).

Our findings demonstrate that the absence of AnxA5 does not impact the biophysical characteristics, including conductance and gating, of the 35 pS single channel. However, there is a significant reduction in the NPo. These results unequivocally exclude the possibility of AnxA5 to function as a pore-forming element of the Ca^{2+} channel. Instead, they strongly indicate that AnxA5 regulates the Ca^{2+} permeability of the VDAC1. Previous research has highlighted the pivotal role of VDAC1 in enabling the Ca^{2+} ion flux across the OMM when it is in its Ca^{2+}-permeable state (98,138). This phenomenon significantly contributes to the intricate orchestration of Ca^{2+} signaling within the IMS. Our experiments using the proximity ligation

assay have revealed that AnxA5 localizes in the VDAC1 microenvironment. However, when we employed the co-IP technique, we did not detect any direct physical interactions between these two proteins. This lack of physical interaction suggests two possible scenarios: either there exists a transient interaction, or AnxA5 is closely localized to VDAC1 without engaging in a direct physical interaction. Our data do not completely deny a dynamic transient interaction between AnxA5 and VDAC1; however, it suggests an alternative role for AnxA5 in regulating VDAC1's Ca^{2+} permeability. In the specific scenario being discussed, it is important to focus on the binding ability of AnxA5 to the negatively charged phospholipids in elevated Ca^{2+} levels. The OMM's negatively charged phospholipids pool generates a lipid microenvironment that facilitates the binding of AnxA5 when high levels of Ca^{2+} are present (94). In this line, previous studies have shown that AnxA5 binds to cardiolipin-rich microdomains in isolated mitochondria to stabilize the membranes in the presence of 10 μM of Ca^{2+} ions (94). Moreover, it has been demonstrated that cardiolipin, constituting approximately 4% of the OMM lipids, exhibits enrichment in the contact sites between the OMM and IMM where VDAC1 is predominantly located (139). Consequently, it is tempting to speculate that AnxA5 can bind to negatively charged phospholipids in the vicinity of VDAC1 in the presence of high Ca^{2+} levels. The interaction between AnxA5 and this specific membrane microdomain may create a distinctive lipid environment that stabilizes VDAC1 in its unique Ca^{2+}-permeable state. By stabilizing the lipid microenvironment of VDAC1, AnxA5 regulates the Ca^{2+} permeability of the VDAC1, thereby contributing to the establishment of Ca^{2+} signaling in the IMS (Figure 36, upper panel).

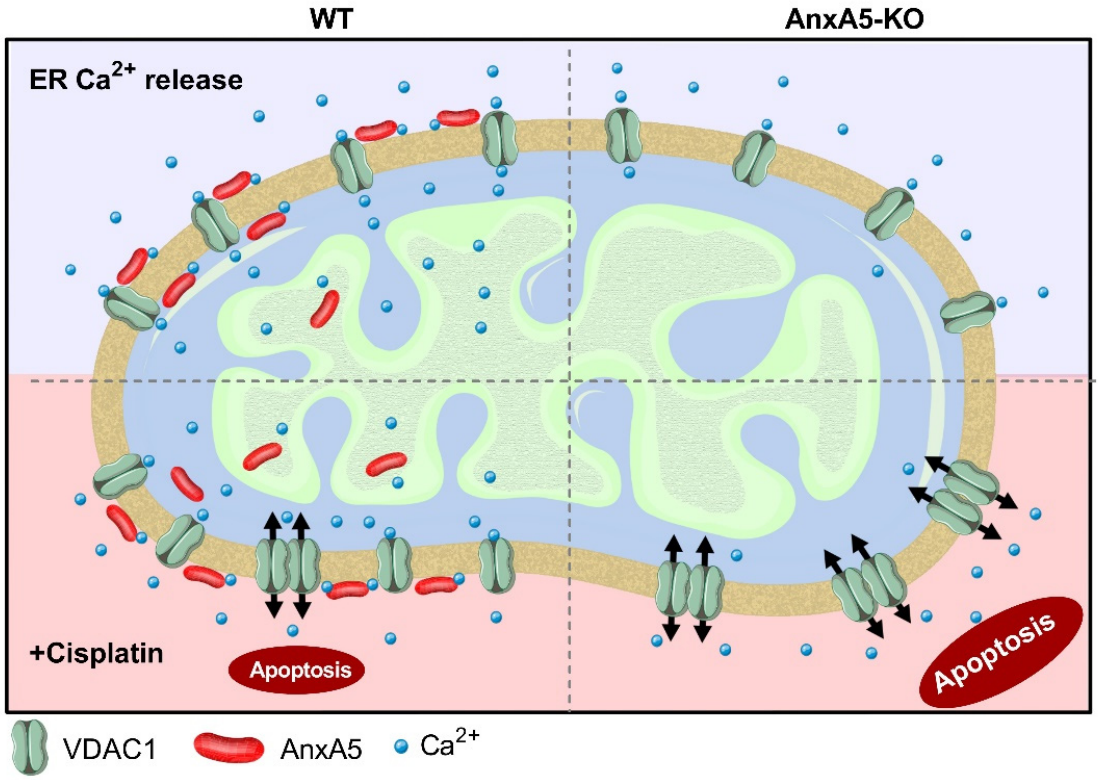

Figure 36. Schematic illustration of AnxA5's role in mitochondrial Ca^{2+} signaling and apoptosis. In its basal state, VDAC1 is observed in a monomeric form, as depicted in the upper panel. However, upon treatment with cisplatin, there is a discernible shift, leading to VDAC1 dimerization and the initiation of apoptotic cell death, as illustrated in the lower panel. This dimerization process is intricately regulated by AnxA5, which exerts its influence by localizing in the VDAC1 microenvironment, consequently impacting the overall level of apoptosis, as highlighted in the lower left panel. Intriguingly, in cells lacking AnxA5, exposure to cisplatin induces a more pronounced VDAC1 dimerization, thereby resulting in an escalated apoptotic response, as demonstrated in the lower right panel. This nuanced interplay emphasizes the crucial role of AnxA5 in modulating VDAC1 dynamics and subsequently influencing apoptotic outcomes. Figure is taken from my own publication (Olfaz et al. 2023, under review) (84).

Our results with cisplatin provided additional evidence confirming AnxA5's role in controlling the stability of VDAC1's singular Ca^{2+}-permeable state. In line with previous research (122), we observed that cisplatin treatment increased mitochondrial Ca^{2+} levels both in the matrix and IMS of WT HeLa cells, while AnxA5KO cells did not show such an effect. This highlights the resistance of AnxA5 KO cells to cisplatin-induced mitochondrial Ca^{2+} overload. Conversely, AnxA5 knockout cells displayed heightened vulnerability to apoptotic cell death when exposed to cisplatin, underscoring that apoptosis is not solely controlled by mitochondrial Ca^{2+} overload. Since these findings hint at an unexplored function of AnxA5 in regulating apoptotic cell death, extensive studies were launched to explore the dimerization state of VDAC1 and the impact of

AnxA5 on cisplatin-triggered apoptosis. Previous studies have demonstrated that under basal conditions, VDAC1 exists in a monomeric state (80,104,140). Upon treating the cells with apoptotic stimuli, including cisplatin, the monomeric equilibrium of VDAC1 shifts to the oligomeric state, which, in turn, establishes a pore to release IMS residing proapoptotic proteins into the cytosol, thereby initiating apoptosis (80). Importantly, a recently developed molecule, VBIT-4, has been shown to inhibit the oligomerization of VDAC1 and, consequently, inhibit apoptosis in different cell lines. Our experiments using VBIT-4 inhibited both cell death and the oligomerization of VDAC1 in both WT and AnxA5KO cells upon cisplatin treatment, providing evidence that the elevated cell death in AnxA5-depleted cells may be due to differences in VDAC1 dimerization level compared to WT cells.

Our investigation into VDAC1 dimerization levels has unveiled significant differences between WT and AnxA5KO cells in response to cisplatin treatment. Specifically, compared to WT, in AnxA5KO cells, we observed a 62% increase in VDAC1 dimerization after 24 hours of cisplatin treatment, and a 17% increase after 48 hours. These results underscore the regulatory role of AnxA5 in the control of VDAC1 dimerization. It has been demonstrated that the negatively charged phospholipids environment around VDAC1 promotes its oligomerization (137). Additionally, during apoptosis, the cytosolic pool of AnxA5 has been shown to translocate to the OMM probably to bind to negatively charged phospholipids (141). Upon binding to these membranes, AnxA5 can self-assemble into 2D arrays, effectively decreasing the lateral diffusion of phospholipids. Consequently, by binding to the negatively charged pool of the OMM, AnxA5 plays a protective role in cisplatin-induced VDAC1 oligomerization (Figure 36 lower panel).

In opposition to our results, a prior investigation showed that in the context of cisplatin-induced apoptosis, AnxA5 promotes VDAC1 oligomerization, thereby intensifying the effects of cisplatin-induced apoptosis (141). In the same study, Jeong et al. showed that AnxA5KO-depleted cells exhibited resistance to apoptosis and reduced VDAC1 oligomerization upon cisplatin treatment. Unlike our study, Jeong et al. reported a significant reduction in VDAC1 levels in AnxA5-depleted cells. Consequently, they observed a 60% reduction in cisplatin-induced VDAC1 dimerization in AnxA5-depleted cells, accompanied by a 70% reduction in VDAC1 levels in the absence of any treatment. Hence, the decreased VDAC1 oligomerization observed in AnxA5 knockout cells following cisplatin treatment can be attributed to the lower VDAC1 expression levels. In line with this assumption, several studies have indicated that VDAC1 expression levels control the equilibrium shift from the monomeric to the oligomeric form (80,140). Additionally, the downregulation of VDAC1 expression has been shown to

confer resistance to cisplatin-induced cell death by forming fewer VDAC1 oligomers (140). Our results demonstrate that AnxA5-KO cells exhibit increased VDAC1 dimerization upon cisplatin treatment without affecting its basal expression level. Therefore, we propose a novel model suggesting that the presence of AnxA5 in the VDAC1 microenvironment controls apoptotic cell death by preventing excessive VDAC1 oligomerization (Figure 36, lower panel).

Together, our data emphasize the pivotal function of AnxA5 in regulating Ca^{2+} flux through OMM by regulating VDAC1's Ca^{2+} permeability. AnxA5 promotes the stability of the lipid environment near VDAC1 and facilitates an efficient transfer of Ca^{2+} to the IMS during ER Ca^{2+} release. AnxA5's presence in the vicinity of VDAC1 regulates the formation of VDAC1 dimers induced by cisplatin and the resulting apoptosis.

4.2 Future Perspectives

Drawing from the insights garnered during my PhD studies, prospective research avenues could delve deeper into the intricate interplay among near-UV light exposure, ROS production, and Ca^{2+} signaling—especially within the realm of single-cell measurements. Future investigations may extend beyond the identified effects to explore potential side effects of near-UV light. Additionally, assessing whether other wavelengths commonly employed in single-cell measurements elicit similar responses in cells could provide a more comprehensive understanding of the broader impacts of light exposure on cellular processes. This approach would enrich our knowledge, offering a more nuanced perspective on the effects of various wavelengths and facilitating a more informed use of light-based techniques in cellular studies.

In the realm of mitochondrial energy metabolism, future inquiries may delve into the nuanced role of S1R, particularly under various cellular states. Exploring the impact of S1R on mitochondrial bioenergetics in diverse cancer cell contexts could reveal additional facets of its regulatory role, potentially uncovering novel therapeutic avenues for modulating cancer cell energy metabolism.

Additionally, the latest research unveiling the crucial role of AnxA5 in mitochondrial Ca^{2+} homeostasis presents opportunities for further exploration. Future studies could delve into the specific molecular mechanisms through which AnxA5 participates in IMS Ca^{2+} signaling. This includes investigating whether AnxA5 regulates IMS Ca^{2+} levels from the cytosolic leaflet of the OMM or the IMS leaflet. Moreover, understanding the broader implications of AnxA5's role in apoptosis and its potential therapeutic applications could be a promising avenue for future

investigations. Overall, these directions could contribute to advancing our knowledge of cellular signaling dynamics and their implications in health and disease.

In conclusion, throughout my PhD, my research focused on intracellular Ca^{2+} signaling, uncovering the impact on transcription factors, mitochondrial Ca^{2+} homeostasis, apoptosis, and cancer cell bioenergetics. I revealed the influence of near-UV light on cytosolic Ca^{2+} oscillations, the multifaceted role of S1R in cancer cell energy metabolism, and the indispensable contribution of AnxA5 to mitochondrial Ca^{2+} homeostasis and apoptosis. Collectively, these findings advance our understanding of cellular signaling dynamics and their implications in health and disease.

5 References

1. Bagur R, Hajnóczky G. Intracellular Ca2+ sensing: role in calcium homeostasis and signaling. Mol Cell. 2017;66(6):780.

2. Selstø CH, Ruoff P. A basic model of calcium homeostasis in non-excitable cells. bioRxiv. 2022;2012–22.

3. Rossi AM, Taylor CW. Reliable measurement of free Ca2+ concentrations in the ER lumen using Mag-Fluo-4. Cell Calcium. 2020;87.

4. Bengtson CP, Bading H. Nuclear calcium signaling. Adv Exp Med Biol. 2012;970:377–405.

5. Dawson AP. Calcium signalling: how do IP3 receptors work? Curr Biol. 1997;7(9).

6. Trinquet E, Bouhelal R, Dietz M. Monitoring Gq-coupled receptor response through inositol phosphate quantification with the IP-One assay. Expert Opin Drug Discov. 2011;6(10):981–94.

7. Ma G, Wei M, He L, Liu C, Wu B, Zhang SL, et al. Inside-out Ca2+ signalling prompted by STIM1 conformational switch. Nat Commun. 2015;6.

8. Hogan PG, Lewis RS, Rao A. Molecular basis of calcium signaling in lymphocytes: STIM and ORAI. Annu Rev Immunol. 2010;28:491–533.

9. Oflaz FE, Koshenov Z, Hirtl M, Rost R, Malli R, Graier WF. Sigma-1 Receptor Modulation by Ligands Coordinates Cancer Cell Energy Metabolism. Biomolecules. 2022;12(6).

10. Oflaz FE, Koshenov Z, Hirtl M, Rost R, Bachkoenig OA, Gottschalk B, et al. Near-UV light induced ROS production initiates spatial Ca2+ spiking to fire NFATc3 translocation. Int J Mol Sci. 2021;22(15):8189.

11. Koshenov Z, Oflaz FE, Hirtl M, Gottschalk B, Rost R, Malli R, et al. Citrin mediated metabolic rewiring in response to altered basal subcellular Ca2+ homeostasis. Commun Biol 2022 51. 2022;5(1):1–15.

12. Shoshan-Barmatz V, De S, Meir A. The Mitochondrial Voltage-Dependent Anion Channel 1, Ca2+ Transport, Apoptosis, and Their Regulation. Front Oncol. 2017;7(APR):1.

13. Primeau JO, Armanious GP, Fisher MLE, Young HS. The sarcoendoplasmic reticulum

calcium ATPase. Subcell Biochem. 2018;87:229–58.

14. Yong J, Bischof H, Burgstaller S, Siirin M, Murphy A, Malli R, et al. Mitochondria supply ATP to the ER through a mechanism antagonized by cytosolic Ca2+. Elife. 2019;8.

15. Strehler EE, Caride AJ, Filoteo AG, Xiong Y, Penniston JT, Enyedi A. Plasma membrane Ca2+-ATPases as dynamic regulators of cellular calcium handling. Ann N Y Acad Sci. 2007;1099:226–36.

16. Giacomello M, Drago I, Bortolozzi M, Scorzeto M, Gianelle A, Pizzo P, et al. Ca2+ Hot Spots on the Mitochondrial Surface Are Generated by Ca2+ Mobilization from Stores, but Not by Activation of Store-Operated Ca2+ Channels. Mol Cell. 2010;38(2):280–90.

17. Swulius MT, Waxham MN. Ca2+/calmodulin-dependent protein kinases. Cell Mol Life Sci. 2008;65(17):2637–57.

18. Putney JW. Calcium signaling: deciphering the calcium-NFAT pathway. Curr Biol. 2012;22(3).

19. Bremer S, Vethe NT, Skauby M, Kasbo M, Johansson ED, Midtvedt K, et al. PHARMACOKINETIC DYNAMIC RELATIONSHIPS NFAT-regulated cytokine gene expression during tacrolimus therapy early after renal transplantation. Br J Clin Pharmacol Br J Clin Pharmacol. 2017;83:2494.

20. Beals CR, Sheridan CM, Turck CW, Gardner P, Crabtree GR. Nuclear export of NF-ATc enhanced by glycogen synthase kinase-3. Science (80-). 1997;275(5308):1930–3.

21. Rao A, Luo C, Hogan PG. TRANSCRIPTION FACTORS OF THE NFAT FAMILY:Regulation and Function. https://doi.org/101146/annurev.immunol151707. 2003;15:707–47.

22. Kar P, Parekh AB. Distinct Spatial Ca2+ Signatures Selectively Activate Different NFAT Transcription Factor Isoforms. Mol Cell. 2015;58(2):232.

23. Kim MS, Usachev YM. Mitochondrial Ca2+ Cycling Facilitates Activation of the Transcription Factor NFAT in Sensory Neurons. J Neurosci. 2009;29(39):12101.

24. Marchi S, Pinton P. The mitochondrial calcium uniporter complex: molecular components, structure and physiopathological implications. J Physiol. 2014;592(Pt 5):829.

25. Gincel D, Zaid H, Shoshan-Barmatz V. Calcium binding and translocation by the

voltage-dependent anion channel: a possible regulatory mechanism in mitochondrial function. Biochem J. 2001;358(Pt 1):147.

26. Messina A, Reina S, Guarino F, De Pinto V. VDAC isoforms in mammals ☆. 2011;

27. Rosencrans WM, Aguilella VM, Rostovtseva TK, Bezrukov SM. α-Synuclein emerges as a potent regulator of VDAC-facilitated calcium transport. Cell Calcium. 2021;95:102355.

28. Camara AKS, Zhou YF, Wen PC, Tajkhorshid E, Kwok WM. Mitochondrial VDAC1: A Key Gatekeeper as Potential Therapeutic Target. Front Physiol. 2017;8(JUN):460.

29. Monaco G, Decrock E, Arbel N, Van Vliet AR, La Rovere RM, De Smedt H, et al. The BH4 Domain of Anti-apoptotic Bcl-XL, but Not That of the Related Bcl-2, Limits the Voltage-dependent Anion Channel 1 (VDAC1)-mediated Transfer of Pro-apoptotic Ca2+ Signals to Mitochondria. J Biol Chem. 2015;290(14):9150–61.

30. De Stefani D, Bononi A, Romagnoli A, Messina A, De Pinto V, Pinton P, et al. VDAC1 selectively transfers apoptotic Ca2+ signals to mitochondria. Cell Death Differ. 2012;19(2):267.

31. De Stefani D, Raffaello A, Teardo E, Szabó I, Rizzuto R. No Title [Internet]. Nature NIH Public Access; Aug 8, 2011 p. 336.

32. Raffaello A, De Stefani D, Sabbadin D, Teardo E, Merli G, Picard A, et al. The mitochondrial calcium uniporter is a multimer that can include a dominant-negative pore-forming subunit. EMBO J. 2013;32(17):2362–76.

33. Chaudhuri D, Artiga DJ, Abiria SA, Clapham DE. Mitochondrial calcium uniporter regulator 1 (MCUR1) regulates the calcium threshold for the mitochondrial permeability transition. Proc Natl Acad Sci U S A. 2016;113(13):E1872–80.

34. Tomar D, Dong Z, Shanmughapriya S, Koch DA, Thomas T, Hoffman NE, et al. MCUR1 Is a Scaffold Factor for the MCU Complex Function and Promotes Mitochondrial Bioenergetics. Cell Rep. 2016;15(8):1673–85.

35. Liu JC, Liu J, Holmström KM, Menazza S, Parks RJ, Fergusson MM, et al. MICU1 Serves as a Molecular Gatekeeper to Prevent In Vivo Mitochondrial Calcium Overload. Cell Rep. 2016;16(6):1561–73.

36. Madreiter-Sokolowski CT, Klec C, Parichatikanond W, Stryeck S, Gottschalk B, Pulido

S, et al. PRMT1-mediated methylation of MICU1 determines the UCP2/3 dependency of mitochondrial Ca2+ uptake in immortalized cells. Nat Commun. 2016;7.

37. Xing Y, Wang M, Wang J, Nie Z, Wu G, Yang X, et al. Dimerization of MICU Proteins Controls Ca2+ Influx through the Mitochondrial Ca2+ Uniporter. Cell Rep. 2019;26(5):1203-1212.e4.

38. Waldeck-Weiermair M, Malli R, Parichatikanond W, Gottschalk B, Madreiter-Sokolowski CT, Klec C, et al. Rearrangement of MICU1 multimers for activation of MCU is solely controlled by cytosolic Ca2+. 2015;5(1):1–10.

39. Gottschalk B, Klec C, Leitinger G, Bernhart E, Rost R, Bischof H, et al. MICU1 controls cristae junction and spatially anchors mitochondrial Ca2+ uniporter complex. Nat Commun. 2019;10(1).

40. Delprat B, Crouzier L, Su TP, Maurice T. At the Crossing of ER Stress and MAMs: A Key Role of Sigma-1 Receptor? Adv Exp Med Biol. 2020;1131:699–718.

41. Gottschalk B, Klec C, Waldeck-Weiermair M, Malli R, Graier WF. Intracellular Ca2+ release decelerates mitochondrial cristae dynamics within the junctions to the endoplasmic reticulum. Pflügers Arch - Eur J Physiol. 2018;470(8):1193–203.

42. Gottschalk B, Koshenov Z, Waldeck-Weiermair M, Radulović S, Oflaz FE, Hirtl M, et al. MICU1 controls spatial membrane potential gradients and guides Ca2+ fluxes within mitochondrial substructures. Commun Biol. 2022;5(1).

43. Boyman L, Williams GSB, Khananshvili D, Sekler I, Lederer WJ. NCLX: The mitochondrial sodium calcium exchanger. J Mol Cell Cardiol. 2013;59:205–13.

44. Palty R, Silverman WF, Hershfinkel M, Caporale T, Sensi SL, Parnis J, et al. NCLX is an essential component of mitochondrial Na+/Ca2+ exchange. Proc Natl Acad Sci U S A. 2010;107(1):436.

45. Brand MD. The stoichiometry of the exchange catalysed by the mitochondrial calcium/sodium antiporter. Biochem J. 1985;229(1):161–6.

46. Jung DW, Baysal K, Brierley GP. The Sodium-Calcium Antiport of Heart Mitochondria Is Not Electroneutral. J Biol Chem. 1995;270(2):672–8.

47. Luongo TS, Lambert JP, Gross P, Nwokedi mary, Lombardi alyssa, Shanmughapriya S, et al. The mitochondrial Na + /Ca 2+ exchanger is essential for Ca 2+ homeostasis and viability. 2017;

48. Nolfi-Donegan D, Braganza A, Shiva S. Mitochondrial electron transport chain: Oxidative phosphorylation, oxidant production, and methods of measurement. Redox Biol. 2020;37:101674.

49. Jonckheere AI, Smeitink JAM, Rodenburg RJT. Mitochondrial ATP synthase: Architecture, function and pathology. J Inherit Metab Dis. 2012;35(2):211–25.

50. Busiello RA, Savarese S, Lombardi A, Diz DI, Joseph AM, Katakam P V. Mitochondrial uncoupling proteins and energy metabolism. 2015;

51. Busiello RA, Savarese S, Lombardi A. Mitochondrial uncoupling proteins and energy metabolism. Front Physiol. 2015;6(FEB):36.

52. Waldeck-Weiermair M, Malli R, Naghdi S, Trenker M, Kahn MJ, Graier WF. The contribution of UCP2 and UCP3 to mitochondrial Ca2+ uptake is differentially determined by the source of supplied Ca2+. Cell Calcium. 2010;47(5):433–40.

53. Trenker M, Malli R, Fertschai I, Levak-Frank S, Graier WF. Uncoupling proteins 2 and 3 are fundamental for mitochondrial Ca 2+ uniport. 2007;

54. Waldeck-Weiermair M, Duan X, Naghdi S, Khan MJ, Trenker M, Malli R, et al. Uncoupling protein 3 adjusts mitochondrial Ca2+ uptake to high and low Ca2+ signals. Cell Calcium. 2010;48(5):288–301.

55. Berardi MJ, Chou JJ. Fatty Acid Flippase Activity of UCP2 Is Essential for Its Proton Transport in Mitochondria. Cell Metab. 2014;20(3):541–52.

56. Oflaz FE, Koshenov Z, Hirtl M, Bachkoenig OA, Graier WF, Gottschalk B. Synergy of uncoupling proteins (1 and 2) with mitochondrial Ca2+ uptake machinery potentiate mitochondrial uncoupling. Cell Calcium. 2023;112:102736.

57. Fedorenko A, Lishko P V., Kirichok Y. Mechanism of Fatty-Acid-Dependent UCP1 Uncoupling in Brown Fat Mitochondria. Cell. 2012;151(2):400–13.

58. Xue K, Wu D, Wang Y, Zhao Y, Shen H, Yao J, et al. The mitochondrial calcium uniporter engages UCP1 to form a thermoporter that promotes thermogenesis. Cell Metab. 2022;34(9):1325-1341.e6.

59. Depaoli MR, Karsten F, Madreiter-Sokolowski CT, Simmen T, Graier WF, Correspondence RM. The Author(s). Cell Rep. 2018;25:501–12.

60. Warburg O, Wind F, Negelein E. THE METABOLISM OF TUMORS IN THE BODY. J

Gen Physiol. 1927;8(6):519.

61. Potter M, Newport E, Morten KJ. The Warburg effect: 80 years on. 2016;

62. Zheng J. Energy metabolism of cancer: Glycolysis versus oxidative phosphorylation (Review). Oncol Lett. 2012;4(6):1151.

63. Navale AM, Paranjape AN. Glucose transporters: physiological and pathological roles. Biophys Rev. 2016;8(1):5.

64. Akram M. Mini-review on Glycolysis and Cancer. 2013;

65. Mccommis KS, Finck BN. Mitochondrial pyruvate transport: a historical perspective and future research directions. 2015;

66. Denton RM. Regulation of mitochondrial dehydrogenases by calcium ions. BBA - Bioenerg. 2009;1787:1309–16.

67. Wang YH, Tao AY, Vaeth M, Feske S. CALCIUM REGULATION OF T CELL METABOLISM. Curr Opin Physiol. 2020;17:207–23.

68. Wan B, Lanoue KF, Cheung JY, Scaduto RC$. Regulation of Citric Acid Cycle by Calcium*. 1989;264(23):13430–9.

69. Antonio Enríquez J. Supramolecular Organization of Respiratory Complexes. 2015;

70. Aydar E, Onganer P, Perrett R, Djamgoz MB, Palmer CP. The expression and functional characterization of sigma (s) 1 receptors in breast cancer cell lines.

71. Pontisso I, Combettes L. Role of Sigma-1 Receptor in Calcium Modulation: Possible Involvement in Cancer. 2021;

72. Hayashi T, Su TP. Sigma-1 Receptor Chaperones at the ER-Mitochondrion Interface Regulate Ca 2+ Signaling and Cell Survival.

73. Koshenov Z, Oflaz FE, Hirtl M, Pilic J, Bachkoenig OA, Gottschalk B, et al. Sigma-1 receptor promotes mitochondrial bioenergetics by orchestrating er ca2+ leak during early er stress. Metabolites. 2021;11(7).

74. Aydar E, Palmer CP, Djamgoz MBA. Sigma Receptors and CancerPossible Involvement of Ion Channels. Cancer Res. 2004;64(15):5029–35.

75. Xiong S, Mu T, Wang G, Jiang X. Mitochondria-mediated apoptosis in mammals. Protein Cell. 2014;5(10):737.

76. Kinnally KW, Antonsson B. A tale of two mitochondrial channels, MAC and PTP, in apoptosis. Apoptosis. 2007;12(5):857–68.

77. Dewson G, Kluck RM. Mechanisms by which Bak and Bax permeabilise mitochondria during apoptosis. J Cell Sci. 2009;122(16):2801–8.

78. Keinan N, Tyomkin D, Shoshan-Barmatz V. Oligomerization of the Mitochondrial Protein Voltage-Dependent Anion Channel Is Coupled to the Induction of Apoptosis. 30(24).

79. Mannella CA. VDAC—A Primal Perspective. Int J Mol Sci. 2021;22(4):1–10.

80. Ben-Hail D, Begas-Shvartz R, Shalev M, Shteinfer-Kuzmine A, Gruzman A, Reina S, et al. Novel Compounds Targeting the Mitochondrial Protein VDAC1 Inhibit Apoptosis and Protect against Mitochondrial Dysfunction. J Biol Chem. 2016;291(48):24986–5003.

81. Keinan N, Tyomkin D, Shoshan-Barmatz V. Molecular and Cellular Biology Oligomerization of the Mitochondrial Protein Voltage-Dependent Anion Channel Is Coupled to the Induction of Apoptosis. 2023;

82. Shoshan-Barmatz V, Maldonado EN, Krelin Y. VDAC1 at the crossroads of cell metabolism, apoptosis and cell stress. 1(1).

83. Zaid H, Israelson A, Nahon E, Shoshan-Barmatz V. Hexokinase-I Protection against Apoptotic Cell Death Is Mediated via Interaction with the Voltage-dependent Anion Channel-1 MAPPING THE SITE OF BINDING * Salah Abu-Hamad ‡1 and the. 2008;

84. Graier W, Ooaz F, Bondarenko A, Trenker M, Waldeck-Weiermair M, Gottschalk B, et al. Annexin-A5 is fundamental for VDAC1-dependent mitochondrial Ca2+ homeostasis and determines the susceptibility to apoptosis. 2023;

85. Gerke V, Moss SE. Annexins: From structure to function. Physiol Rev. 2002;82(2):331–71.

86. Huber R, Romisch J, Paques EP. The crystal and molecular structure of human annexin V, an anticoagulant protein that binds to calcium and membranes. EMBO J. 1990;9(12):3867–74.

87. Reviakine I, Bergsma-Schutter W, Mazères-Dubut C, Govorukhina N, Brisson A. Surface Topography of the p3 and p6 Annexin V Crystal Forms Determined by Atomic Force Microscopy. J Struct Biol. 2000;131(3):234–9.

88. Wang J, Liu J, Cao Y, Hu M, Hua Z. Domain IV of Annexin A5 Is Critical for Binding

Calcium and Guarantees Its Maximum Binding to the Phosphatidylserine Membrane. Molecules. 2017;22(12):2256.

89. Lin YC, Chipot C, Scheuring S. Annexin-V stabilizes membrane defects by inducing lipid phase transition. Nat Commun. 2020;11(1):230.

90. Köhler G, Hering U, Zschörnig O, Arnold K. Annexin V Interaction with Phosphatidylserine-Containing Vesicles at Low and Neutral pH †. 1997;36:25.

91. Berendes R, Burger A, Voges D, Demange P, Huber R. Calcium influx through annexin V ion channels into large unilamellar vesicles measured with fura-2. FEBS Lett. 1993;317(1–2):131–4.

92. Hawkins TE, Das D, Young B, Moss SE. DT40 cells lacking the Ca2+-binding protein annexin 5 are resistant to Ca2+-dependent apoptosis. Proc Natl Acad Sci. 2002;99(12):8054–9.

93. Sun J, Bird CH, Salem HH, Bird P. Association of annexin V with mitochondria. FEBS Lett. 1993;329(1–2):79–83.

94. Megli FM, Selvaggi M, De Lisi A, Quagliariello E. EPR study of annexin V-cardiolipin Ca-mediated interaction in phospholipid vesicles and isolated mitochondria. Biochim Biophys Acta - Biomembr. 1995;1236(2):273–8.

95. Megli FM, Mattiazzi M, Di Tullio T, Quagliariello E. Annexin V binding perturbs the cardiolipin fluidity gradient in isolated mitochondria. Can it affect mitochondrial function? Biochemistry. 2000;39(18):5534–42.

96. Palmer AE, Giacomello M, Kortemme T, Hires SA, Lev-Ram V, Baker D, et al. Ca2+ Indicators Based on Computationally Redesigned Calmodulin-Peptide Pairs. Chem Biol. 2006;13(5):521–30.

97. Palmer AE, Jin C, Reed JC, Tsien RY. Bcl-2-mediated alterations in endoplasmic reticulum Ca2+ analyzed with an improved genetically encoded fluorescent sensor. Proc Natl Acad Sci U S A. 2004;101(50):17404.

98. Waldeck-Weiermair M, Gottschalk B, Madreiter-Sokolowski CT, Ramadani-Muja J, Ziomek G, Klec C, et al. Development and Application of Sub-Mitochondrial Targeted Ca2 + Biosensors. Front Cell Neurosci. 2019;13:449.

99. Bouter A, Gounou C, Bérat R, Tan S, Gallois B, Granier T, et al. Annexin-A5 assembled into two-dimensional arrays promotes cell membrane repair. Nat Commun. 2011;2(1):1–

9.

100. Dana H, Sun Y, Mohar B, Hulse BK, Kerlin AM, Hasseman JP, et al. High-performance calcium sensors for imaging activity in neuronal populations and microcompartments. Nat Methods 2019 167. 2019;16(7):649–57.

101. Reichmann F, Painsipp E, Holzer P, Kummer D, Bock E, Leitinger G. A novel unbiased counting method for the quantification of synapses in the mouse brain. J Neurosci Methods. 2015;240:13–21.

102. Sobol M, Philimonenko V V., Hozák P. Comparison of methods of high-pressure freezing and automated freeze-substitution of suspension cells combined with LR White embedding. Histochem Cell Biol. 2010;134(6):631–41.

103. Tubbs E, Rieusset J. Study of Endoplasmic Reticulum and Mitochondria Interactions by In Situ Proximity Ligation Assay in Fixed Cells. J Vis Exp. 2016;2016(118):54899.

104. Weisthal S, Keinan N, Ben-Hail D, Arif T, Shoshan-Barmatz V. Ca2 +-mediated regulation of VDAC1 expression levels is associated with cell death induction. Biochim Biophys Acta - Mol Cell Res. 2014;1843(10):2270–81.

105. Schindelin J, Arganda-Carreras I, Frise E, Kaynig V, Longair M, Pietzsch T, et al. Fiji: an open-source platform for biological-image analysis. Nat Methods 2012 97. 2012;9(7):676–82.

106. Frezza C, Cipolat S, Scorrano L. Organelle isolation: functional mitochondria from mouse liver, muscle and cultured fibroblasts. Nat Protoc. 2007;2(2):287–95.

107. Wieckowski MRMR, Giorgi C, Lebiedzinska M, Duszynski J, Pinton P. Isolation of mitochondria-associated membranes and mitochondria from animal tissues and cells. Nat Protoc 2009 411. 2009;4(11):1582–90.

108. Zhou YD, Fang XF, Cui ZJ. UVA-induced calcium oscillations in rat mast cells. Cell Calcium. 2009;45(1):18–28.

109. Csordás G, Renken C, Várnai P, Walter L, Weaver D, Buttle KF, et al. Structural and functional features and significance of the physical linkage between ER and mitochondria. J Cell Biol. 2006;174(7):915–21.

110. Matsuno K, Senda T, Kobayashi T, Mita S. Involvement of σ1 receptor in (+)-N-allylnormetazocine-stimulated hippocampal cholinergic functions in rats. Brain Res. 1995;690(2):200–6.

111. Matsumoto RR, Bowen WD, Tom MA, Vo VN, Truong DD, De Costa BR. Characterization of two novel o-receptor ligands" antidystonic effects in rats suggest o-receptor antagonism. Eur J Pharmacol. 1995;280:301–10.

112. Galaz A, Cortés-Molina F, Arce-Molina R, Romero-Gómez I, Mardones GA, Felipe Barros L, et al. Imaging of the Lactate/Pyruvate Ratio Using a Genetically Encoded Förster Resonance Energy Transfer Indicator. Anal Chem. 2020;92(15):10643–50.

113. Brachvogel B, Dikschas JJ, Moch H, Welzel H, Mark K von der, Hofmann C, et al. Annexin A5 Is Not Essential for Skeletal Development. Mol Cell Biol. 2003;23(8):2907–13.

114. Zorova LD, Popkov VA, Plotnikov EY, Silachev DN, Pevzner IB, Jankauskas SS, et al. Mitochondrial membrane potential. Anal Biochem. 2018;552:50.

115. Szabadkai G, Bianchi K, Várnai P, De Stefani D, Wieckowski MR, Cavagna D, et al. Chaperone-mediated coupling of endoplasmic reticulum and mitochondrial Ca2+ channels. J Cell Biol. 2006;175(6):901.

116. D'Eletto M, Rossin F, Occhigrossi L, Farrace MG, Faccenda D, Desai R, et al. Transglutaminase Type 2 Regulates ER-Mitochondria Contact Sites by Interacting with GRP75. Cell Rep. 2018;25(13):3573-3581.e4.

117. Collins TJ, Lipp P, Berridge MJ, Bootman MD. Mitochondrial Ca2+ Uptake Depends on the Spatial and Temporal Profile of Cytosolic Ca2+ Signals. J Biol Chem. 2001;276(28):26411–20.

118. Wang L, Yang X, Li S, Wang Z, Liu Y, Feng J, et al. Structural and mechanistic insights into MICU1 regulation of mitochondrial calcium uptake. EMBO J. 2014;33(6):594.

119. Söderberg O, Gullberg M, Jarvius M, Ridderstråle K, Leuchowius KJ, Jarvius J, et al. Direct observation of individual endogenous protein complexes in situ by proximity ligation. Nat Methods 2006 312. 2006;3(12):995–1000.

120. Monastyrskaya K, Babiychuk EB, Hostettler A, Rescher U, Draeger A. Annexins as intracellular calcium sensors. Cell Calcium. 2007;41(3):207–19.

121. Keinan N, Pahima H, Ben-Hail D, Shoshan-Barmatz V. The role of calcium in VDAC1 oligomerization and mitochondria-mediated apoptosis. Biochim Biophys Acta - Mol Cell Res. 2013;1833(7):1745–54.

122. XU YE, WANG C, SU J, XIE QI, MA L, ZENG L, et al. Tolerance to endoplasmic

reticulum stress mediates cisplatin resistance in human ovarian cancer cells by maintaining endoplasmic reticulum and mitochondrial homeostasis. Oncol Rep. 2015;34(6):3051–60.

123. Shen L, Wen N, Xia M, Zhang Y, Liu W, Xu Y, et al. Calcium efflux from the endoplasmic reticulum regulates cisplatin-induced apoptosis in human cervical cancer HeLa cells. Oncol Lett. 2016;11(4):2411.

124. McCormack JG, Bromidge ES, Dawes NJ. Characterization of the effects of Ca2+ on the intramitochondrial Ca2+-sensitive dehydrogenases within intact rat-kidney mitochondria. BBA - Bioenerg. 1988;934(3):282–92.

125. Miranda JG, Schleicher WE, Wells KL, Ramirez DG, Landgrave SP, Benninger RKP. Dynamic changes in β-cell [Ca2+] regulate NFAT activation, gene transcription, and islet gap junction communication. Mol Metab. 2022;57:101430.

126. Yissachar N, Sharar Fischler T, Cohen AA, Reich-Zeliger S, Russ D, Shifrut E, et al. Dynamic Response Diversity of NFAT Isoforms in Individual Living Cells. Mol Cell. 2013;49(2):322–30.

127. Trapp S, Tucker SJ, Ashcroft FM. Activation and inhibition of K-ATP currents by guanine nucleotides is mediated by different channel subunits. Proc Natl Acad Sci U S A. 1997;94(16):8872–7.

128. Murphy JG, Crosby KC, Dittmer PJ, Sather WA, Dell'Acqua ML. AKAP79/150 recruits the transcription factor NFAT to regulate signaling to the nucleus by neuronal L-type Ca2+ channels. Mol Biol Cell. 2019;30(14):1743–56.

129. Pak V V, Ezerin¸a D, Ezerin¸a E, Lyublinskaya OG, Vriz S, Messens J, et al. Ultrasensitive Genetically Encoded Indicator for Hydrogen Peroxide Identifies Roles for the Oxidant in Cell Migration and Mitochondrial Function.

130. Alfar EA, Kirova D, Konantz J, Birke S, Mansfeld J, Ninov N. Distinct Levels of Reactive Oxygen Species Coordinate Metabolic Activity with Beta-cell Mass Plasticity OPEN.

131. Pan MG, Xiong Y, Chen F. NFAT Gene Family in Inflammation and Cancer. Curr Mol Med. 2013;13(4):543–54.

132. Griesche N, Sanchez G, Hermans C, Idevall-Hagren O. Cortical mitochondria regulate insulin secretion by local Ca2+ buffering in rodent beta cells. J Cell Sci. 2019;132(9).

133. Kubista H, Hawkins TE, Patel DR, Haigler HT, Moss SE. Annexin 5 mediates a peroxide-

induced Ca2+ influx in B cells. Curr Biol. 1999;9(23):1403–8.

134. Watson WD, Srivastava M, Leighton X, Glasman M, Faraday M, Fossam LH, et al. Annexin 7 mobilizes calcium from endoplasmic reticulum stores in brain. Biochim Biophys Acta - Mol Cell Res. 2004;1742(1–3):151–60.

135. Chlystun M, Campanella M, Law AL, Duchen MR, Fatimathas L, Levine TP, et al. Regulation of Mitochondrial Morphogenesis by Annexin A6. PLoS One. 2013;8(1):e53774.

136. Moran O, Sciancalepore M, Sandri G, Panfili E, Bassi R, Ballarin C, et al. Ionic permeability of the mitochondrial outer membrane. Eur Biophys J. 1992;20(6):311–9.

137. Betaneli V, Petrov EP, Schwille P. The Role of Lipids in VDAC Oligomerization. Biophys J. 2012;102(3):523.

138. Shoshan-Barmatz V, De Pinto V, Zweckstetter M, Raviv Z, Keinan N, Arbel N. VDAC, a multi-functional mitochondrial protein regulating cell life and death. Mol Aspects Med. 2010;31(3):227–85.

139. Ardail D, Privat JP, Egret-Charlier M, Levrat C, Lerme F, Louisot P. Mitochondrial contact sites. Lipid composition and dynamics. J Biol Chem. 1990;265(31):18797–802.

140. Arif T, Vasilkovsky L, Refaely Y, Konson A, Shoshan-Barmatz V. Silencing VDAC1 Expression by siRNA Inhibits Cancer Cell Proliferation and Tumor Growth In Vivo. Mol Ther Nucleic Acids. 2014;3(4):e159.

141. Jeong JJ, Park N, Kwon YJ, Ye DJ, Moon A, Chun YJ. Role of Annexin A5 in Cisplatin-induced Toxicity in Renal Cells. J Biol Chem. 2014;289(4):2469–81.